RHODES UNIVERSITY
Grahamstown • 6140 • South Africa

Petrography, geochemistry and origin of atypical sedimentary-igneous contact relationships at the base of the Hotazel Formation around Middelplaats, Northern Cape Province, RSA

By

Matt Terracin

A dissertation submitted in partial fulfilment of the requirements for the degree of

MASTER OF SCIENCE
(Exploration Geology)

MSc Exploration Geology Programme
Geology Department
Rhodes University
P.O. Box 94
Grahamstown 6140
South Africa

Revised March, 2014

ACKNOWLEDGEMENTS

I would like to thank everyone in the geology department at Rhodes University. Without their combined support and help no research (not just the authors) would be possible. It is only through the combined efforts of us all that we aid in the progression of knowledge.

I would like to point out the extraordinary efforts of my supervisor Dr Harilaos Tsikos for his direction in this research; Dr Gabi Costin for his substantial time devoted to helping me understand the interaction and development of geochemical relationships and analytical chemistry; Dr Stephen Prevec (Head of the Department of Geology) for his mentoring, igneous petrographical insights and the occasional acoustical guitar songs; Professor Young Yao for his dedication to the Exploration Geology program during these very challenging times and Ms Ashley Goddard for answering every other question that happened to cross my mind during the course of the last year.

Special mention should also be given to Mr Bantu Ntsaluba for his aid in preparing the analytical samples as well as the entire staff of the geology lab led by Mr John Hepple.

Thanks must also be given Ms Maggie Marokane for her aid with the microprobe, data analysis and personal support as well as my classmates, other friends and family who have supported me during this and my other endeavours.

DECLARATION

I, Matthew Theodore Terracin, declare this dissertation to be my own work. It is submitted in fulfilment of the Degree of Master of Science at the University of Rhodes. It has not been submitted before for any degree or examination in any other University or tertiary institution.

Signature of the candidate: ……………………………………….

Date: ………………………………………………………………

ABSTRACT

In the Middelplaats mine area of the Kalahari manganese field, two drill holes (MP53 and MP54) intersected anomalously high-grade manganese ore sitting stratigraphically just above an igneous body (likely a dike or sill). Manganese ore located within approximate 5 meters of the contact with the underlying igneous rocks has been substantially metasomatically upgraded from 25% manganese, to over 40% whilst the dominant manganese species with in the ore has been altered to hausmannite. This report demonstrates the metasomatic alteration is related to devolatilization (removal and/or remobilization of H_2O, CO_2 and CaO) due to contact metamorphism caused by the underlying igneous rocks.

The Middelplaats mine is situated in the southwest corner of the Kalahari manganese field where the paleo basin shallows out and ends. Within the mine area, several stratigraphic units pinch out or are truncated by the side of the basin. This pinching out of lithological formations has led to the underlying Ongeluk Formation being in contact with the much younger units of the Hotazel Formation. Therefore, geochemical investigation into the nature and source of the igneous rocks was also undertaken to see if the rocks from the two drill holes were related to one another and/or the underlying Ongeluk Formation.

Results of these geochemical studies have demonstrated that the Middelplaats igneous rocks (dolerites) from the two drill holes (MP53 and MP54) share a co-genetic source region. There is also reasonable geochemical evidence that the source region of the Middelplaats igneous rocks was substantially similar to the source region of the Ongeluk Formation. This may indicate that the source region of the Ongeluk Formation was reactivated at some later stage resulting in the emplacement of doleritic dikes or sills in the Middelplaats mine area.

The Middelplaats igneous rocks were also found to have undergone a slight but pervasive potassic alteration; with most of the original plagioclase feldspar showing some level of replacement by a potassium enriched feldspar. Although no source for this potassic fluid was found, the devolatilization reaction within the manganese ore appears to have released some potassium into the surrounding rocks. This additional potassium may be responsible for some localized potassic alteration.

Table of Contents

LIST OF FIGURES

LIST OF FIGURES

LIST OF FIGURES

LIST OF TABLES

Chapter 1 Introduction

1.1 *General background*

The late Archaean to Paleoproterozoic iron and manganese formations of the Transvaal Supergroup (Kaapvaal Craton) of South Africa (Figure 1-1) contain an estimated 5,370 Mt of iron ore making it the world's 9th largest iron resource (DeYoung, et al., 1984). The Transvaal Supergroup also contains more than 8 billion tons of manganese ore at grades between 20 and 48 wt percent Mn (Tsikos, et al., 2003); an incredible 80% of known land-based manganese resources worldwide (DeYoung, et al., 1984; Astrup & Tsikos, 1998; International Manganese Institute, 2013). Although there has been extensive past research focusing on the iron, manganese and the Transvaal Supergroup as a whole, there still remain areas that are poorly understood and need further research to fill in gaps within our current understanding. There are also several areas of study in which the existing research is contested with various researchers failing to come to a consensus, and as more research is completed on one subject, it invariably highlights flaws and gaps in prior areas of study necessitating a re-visit and/or re-interpretation of the existing data. This project is intended to look at one of these latter questions; to re-visit a small but distinctive assumed correlation between the Kalahari manganese field and the underlying lithologies within the greater Transvaal Supergroup.

The area of study is located within the now closed Middelplaats manganese mine which lies at the southern end of the Kalahari manganese field in the Griqualand West region of the Northern Cape Province, approximately 60 km west of Kuruman (Figure 1-1C). The stratiform ore body (Figure 1-2) is located approximately 300-400m deep with a strike length of more than 5 km (Jennings, 1986). Anglo American Corporation commenced underground mining operations in August of 1979. Peak production was estimated at 1.1 Mt of metallurgical grade manganese ore per year. In 1983 the mine was sold to South African Manganese Amcor, Ltd. (SAMANCOR) (Jennings, 1986).

After being on "Care and Maintenance" status for approximately a decade SAMANCOR and BHP Billiton researched re-opening the underground mine from March-May 2008 (South African Heritage Resources Agency, 2013). Although no easily accessible public documents were released, one can assume it was uneconomic to do so as no mining activity was undertaken and application to formally close the mine was submitted on Friday, December 7, 2012 (South African Heritage Resources Agency, 2013).

The general geographical setting is dominated by the mostly flat topography created by the thick cover of calcrete and gravels of the Kalahari Formation (Altermann & Nelson, 1998). The mean elevation lies between 1050m to 1500m and is intersected by the North-South trending Asbestos Hills, Klipfontein Hills and the Gamagara Ridges. Regional water drainage pattern is northwards which creates seasonal rivers and streams. Local climate is semi-arid with average annual rainfall of 250-350 mm (Jennings, 1986). Infrastructure in the area is regarded as good and conducive to mining operations with well paved main roads and accessible rail lines to shipping ports (e.g. Port Elizabeth) (Jennings, 1986).

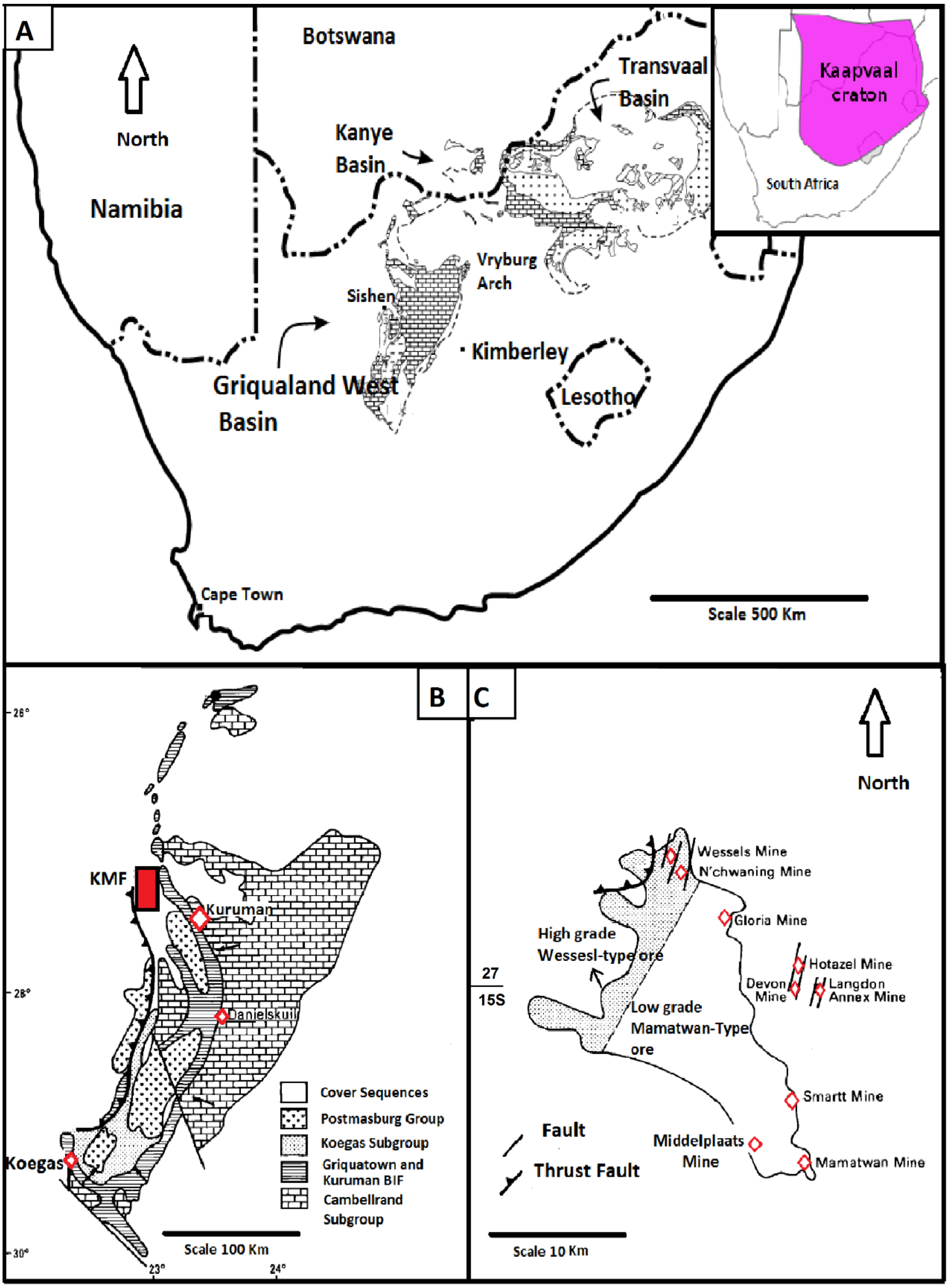

Figure 1-1 A) Simplified map of the Transvaal and Griqualand West sub-basins with inset showing the location of the Kaapvaal craton; B) Detail map of the Griqualand West sub-basin showing the location and extent of the Kalahari manganese field (KMF); C) Detail map of the KMF showing the location of the Middelplaats mine. Modified after Tsikos and Moore, (1997) and Moore, et al., (2001)

]

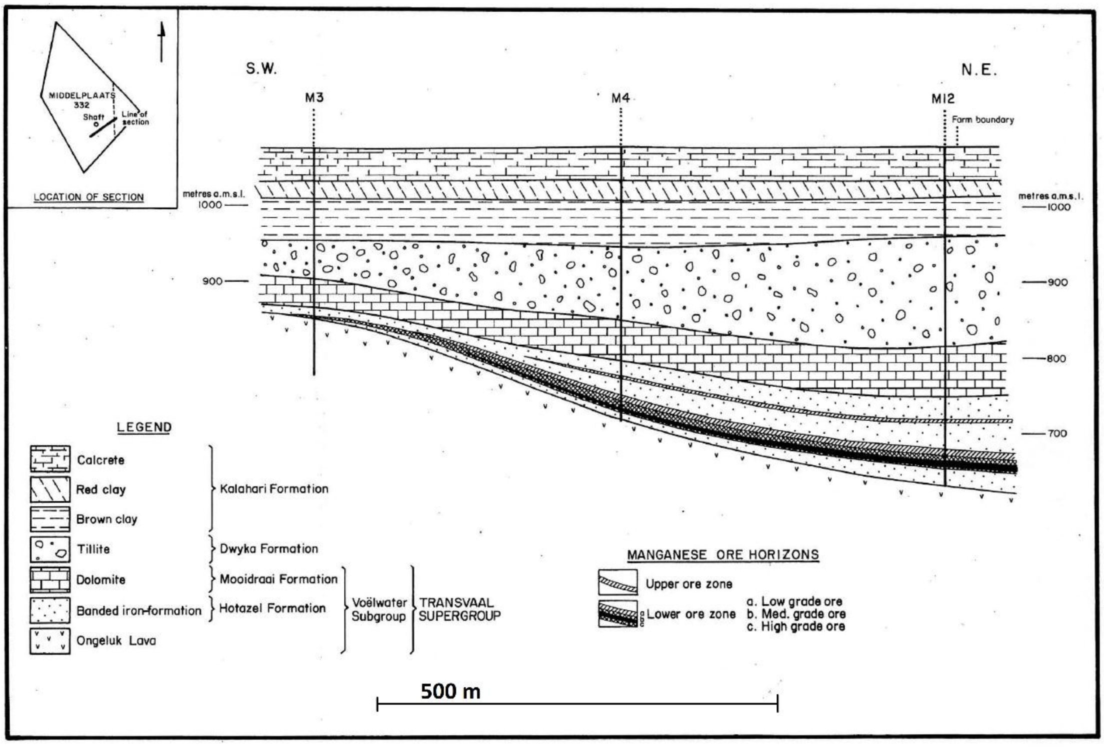

Figure 1-2 Cross section of the Middelplaats mine showing the location of the orebody. Modified after Jennings (1986).

1.2 *Regional geology*

1.2.1 Kaapvaal Craton, Ghaap and Chuniespoort Groups, Lower Transvaal Supergroup

The Archean Kaapvaal and Zimbabwe cratons together form the nucleus of continental Southern Africa. The Kaapvaal Craton (Figure 1-3), host to the Transvaal Supergroup (the main area of this study), is comprised of two domains; the 3.5 Ga eastern domain and the younger 3.2 Ga western domain (James, et al., 2003). The Kaapvaal cratonic nucleus was mostly stabilized by about 3.1 Ga which was then followed by the accretion of composite terranes composed of detrital material from the surrounding intracratonic subdomains (Eriksson, et al., 2011). Detrital material from the north was supplied from the Murchison terrane and from the western Kimberley block (Figure 1-3).

Microbial and stromatolitic material mark some of the oldest known marine deposits in the world, with the earliest large carbonate platforms developing in intracratonic basins shortly after cratonic stabilization (Altermann & Nelson, 1998). The development of these large carbonate and chemical sedimentary platforms is thought to have been made possible due to the almost complete absence of clastic input occurring during long periods of tectonic quiescence (Altermann & Nelson, 1998; James, et al., 2003). One of the best preserved of these domains and one of the most economically important is the intracratonic basin of the Transvaal Supergroup, South Africa (Evans, 1993).

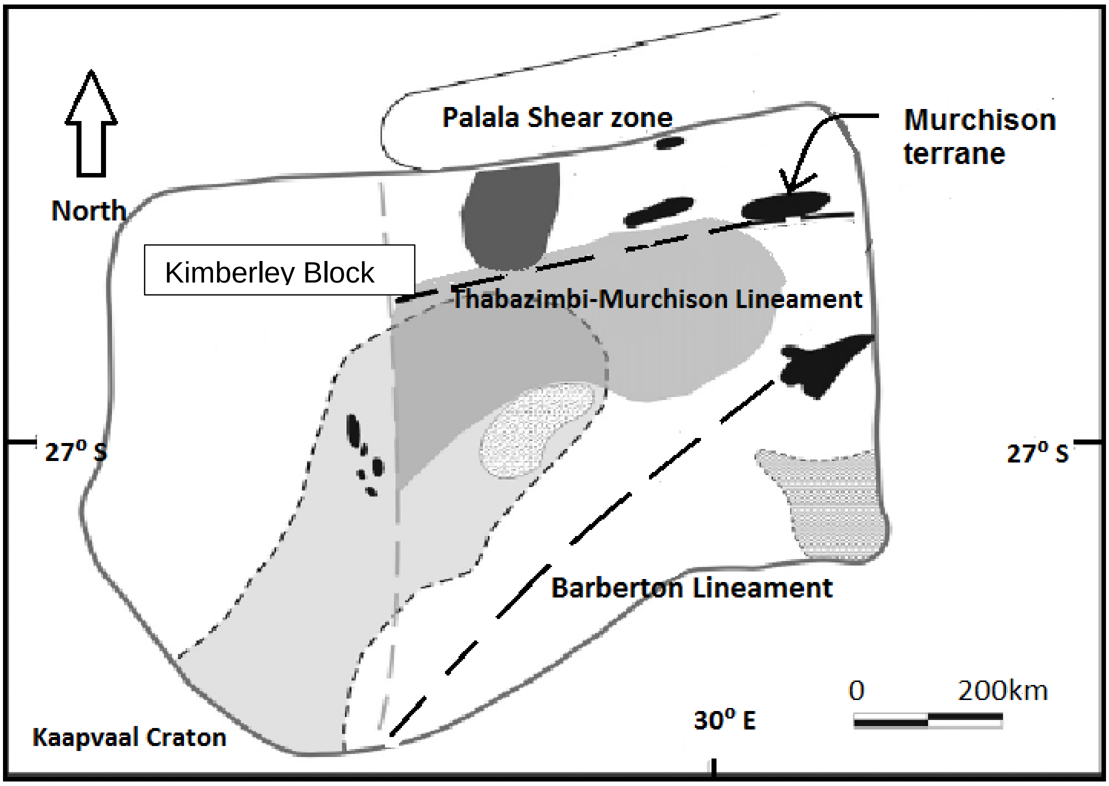

Figure 1-3 Map of the Kaapvaal Craton modified after Eriksson, et al., (2011)

The approximate beginning and end of deposition of the Transvaal Supergroup (~2.66-2.05 Ga) is bracketed by two major mantle plume events that had a profound impact on the composition of the Kaapvaal Craton. The first of these events was the ca. 2.7 Ga emplacement of the Ventersdorp Supergroup lavas and the second was the intrusion of the ca. 2.058 Ga Bushveld Complex (Eriksson, et al., 1993; Eriksson, et al., 2011).

The Transvaal Supergroup is preserved in three separate basins, the Griqualand West and Transvaal basins of South Africa and the Kanye Basin of Botswana (Altermann & Nelson, 1998). These basins are separated by a basement rock high known as the Vryburg Rise/Arch, which divides the area into two geographically similar regions

(Figure 1-4). Correlation of stratigraphy across the three Transvaal basins is complex and hindered by paleotopography, lack of outcrop, local disconformities and thrusting in the western region (Eriksson & Clendenin, 1990).

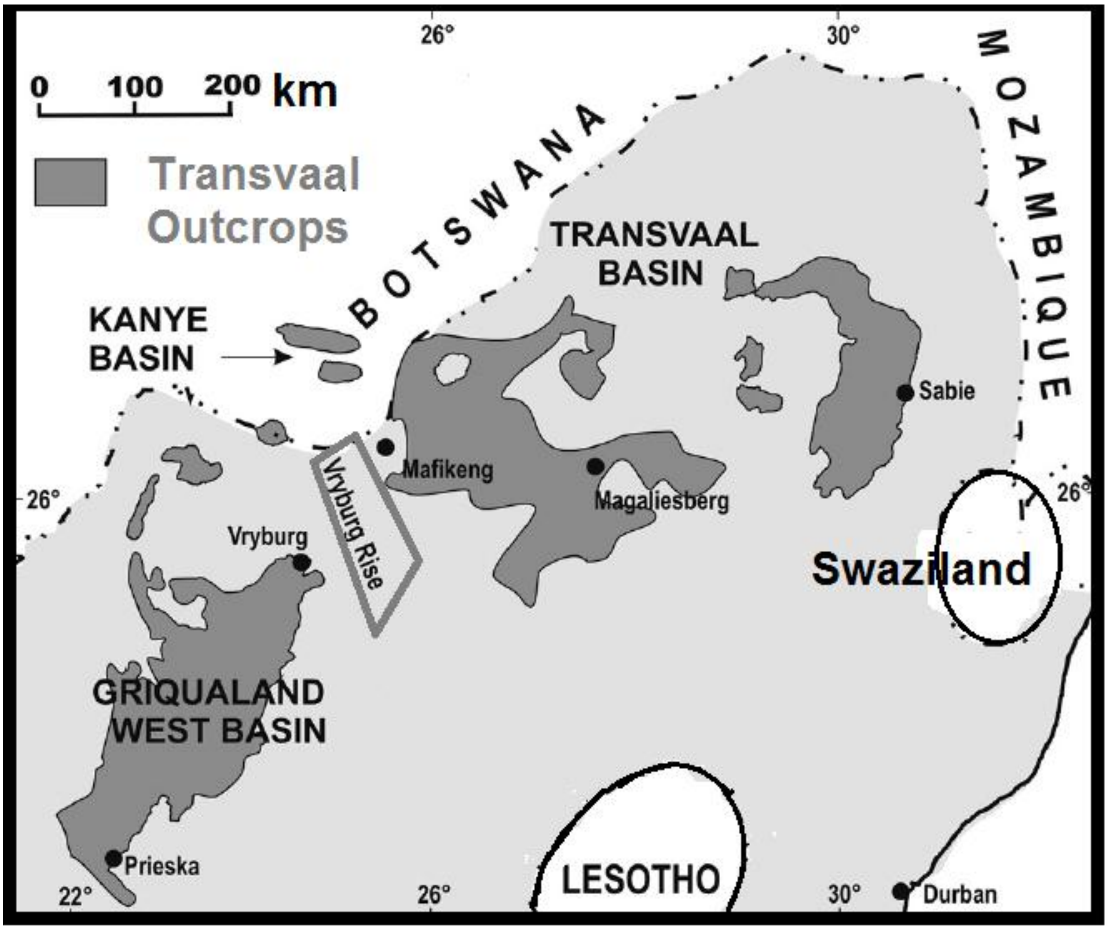

Figure 1-4 Simplified map showing the locations of the Griqualand West, Transvaal, Kanye basins and the Vryburg Rise/Arch modified after Eriksson, et al., (2011)

The basement rock for all three basins are the lavas of the Ventersdorp Supergroup (Altermann & Nelson, 1998) which is unconformably overlain by the sediments of the Transvaal Supergroup. In the Transvaal and Kanye basins, the basal formation is the Black Reef formation (Eriksson & Clendenin, 1990). This formation is composed of fluvio sheet sandstones and conglomerates, which grade into a transgressive marine sequence known as the Chuniespoort Group in the Transvaal Basin and Taupone in the Kanye Basin. In the Griqualand West Basin, the lowermost unit is the 2,642 Ma old Vryburg Formation, West Schmidtsdrif Subgroup of the Ghaap Group (Figure 1-5), which is regarded as the equivalent of the Black Reef Formation (Altermann & Nelson, 1998). These lower most units of all three basins are generally composed of stromatilic carbonates (mostly dolomitized), banded iron formations (BIF) and mixed siliclastic sediments (Eriksson, et al., 1993; Altermann & Nelson, 1998; Eriksson & Altermann, 1998; Moore, et al., 2001).

Rift type extensional tectonics, thermal subsidence (and the associated isostatic rebound) which were results of the Ventersdorp mantle plume had significant effects on the depositional environment. Eriksson & Altermann (1998) have described the paleo setting as varying from exposed peri-tidal flats to deep-sea carbonate platforms with deposition of BIF lithologies commencing at ca. 2.5 Ga., when a further marine transgression drowned the carbonate platform (Altermann & Nelson, 1998). Coeval with the withdrawal of the epeiric sea from the Kaapvaal Craton was the deposition of mixed clastic and chemical sediments of the Duitschland and Koegas subgroups in the Transvaal and Griqualand basins respectively (Eriksson, et al., 2011).

An angular unconformity separates the Chuniespoort and Ghaap Groups from the overlying Pretoria and Postmasburg Groups respectively (Eriksson, et al., 1993; Eriksson & Altermann, 1998; Moore, et al., 2001; Eriksson, et al., 2011). This unconformity is much more pronounced in the eastern Transvaal Basin, where in places it is estimated to have eroded up to 3 km in a north (Mokopane) to south (Carolina) direction; in places the entire lower sequence has been eroded exposing the lower most Black Reef Formation (Eriksson, et al., 2011). Similarly for the Kanye Basin the corresponding units of the Segwagua Group overlie the Taupone Group (Altermann & Nelson, 1998). In both the Transvaal and Kanye basins the unconformity is characterized by a distinctive chert breccia and conglomerate that sit on a paleo-karstic surface (Moore, et al., 2001; Eriksson, et al., 2011).

The much shallower unconformity in the Griqualand West Basin is not seen at the outcrop level but has been inferred from the presence of detrital iron formation, carbonate and chert fragments interstitial to the overlying glacial diamictites of the Makganyene Formation which sit on top of the Asbesheuwels and Koegas subgroups (Moore, et al., 2001).

The contact between the Makganyene Formation and the underlying Asbesheuwels Subgroup is gradational and largely conformable throughout most of the Griqualand West Basin (Eriksson, et al., 2011). Thrusting in the south-west area of the basin has resulted in the only area where the Koegas Subgroup is in unconformable contact with the overlying Makganyene Formation (Moore, et al., 2001). The detrital iron formation and carbonates that characterize the unconformable contact have been dated by Kirschvink, et al., (2000) at 2415 ± 6 Ma (Pb-Pb) and interpreted as shelf deposits that were removed from clastic input due to third order sea-level cyclicity.

The Duitschland Formation in the Transvaal basin is composed of diamictites, intermediate volcanics and carbonates, which although commonly correlated with the Koegas Subgroup are undated. However, Gutzmer & Beukes, (1998) dated a tuff layer in the Penge Iron Formation just below the Duitschland at 2480 ± 18Ma and Hannah, et al., (2004) dated authigenic pyrite at the top of the correlate Rooihoogte Formation at 2316 ± 7 Ma. It is therefore reasonable to estimate the date of the formation for the Duitschland at ~2.35 Ga (Frauenstein, et al., 2009) and as noted earlier, the unconformable contact cuts down through the underlying Penge and Malmani units (Eriksson & Altermann, 1998; Moore, et al., 2001; Eriksson, et al., 2011). Eriksson, et.al (2011) also note that folding in the underlying carbonate and iron units has led to the appearance of a conformable relationship with the Duitschland lithologies and that one must take into account the three dimensional geometry of the basin to see the unconformable nature of the contact.

Radiometric dating of the unconformable Postmasburg, Pretoria groups and underlying Ghaap and Chuniespoort Groups performed by Eriksson, et al., (1993) indicate a substantial hiatus in deposition of approximately 80 Ma.

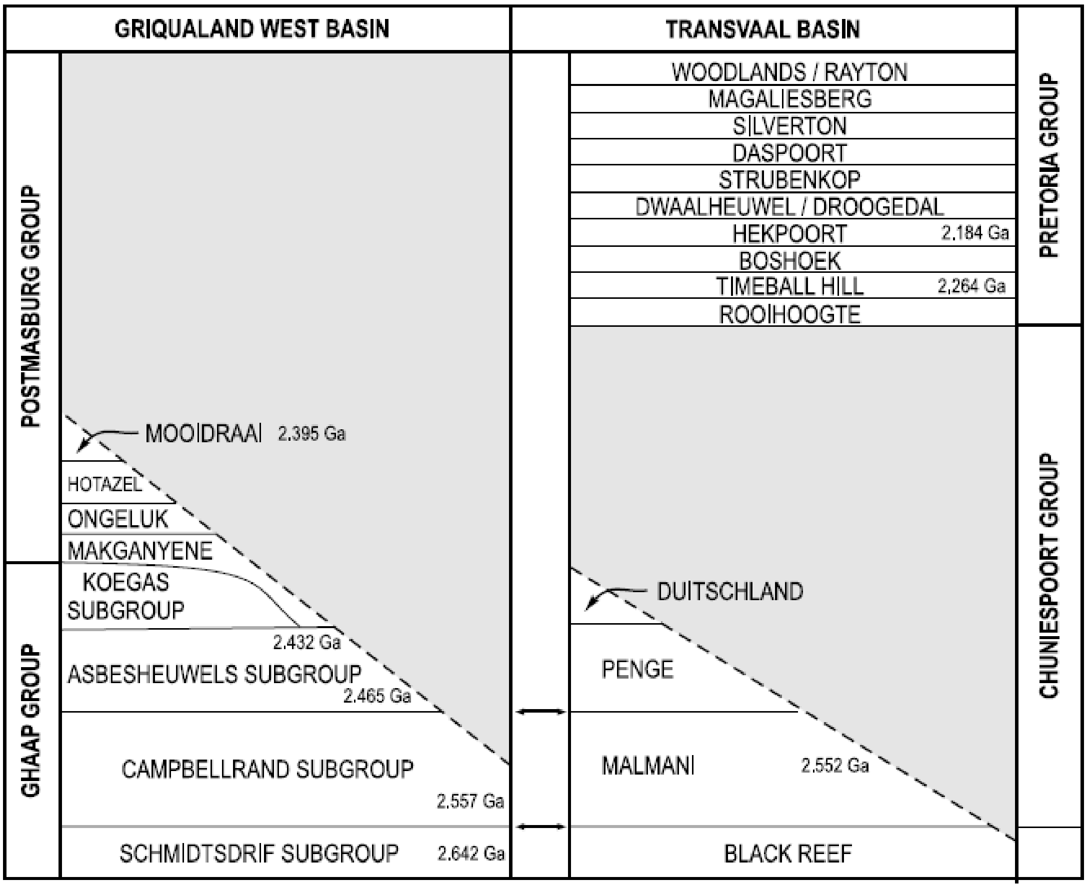

Figure 1-5 Simplified stratigraphy of the Transvaal Supergroup showing correlations between the Griqualand West, Transvaal and Kanye Basins reproduced from Moore, et al., (2001)

1.2.2 Postmasburg and Pretoria Groups; Upper Transvaal Supergroup

The Chuniespoort Group is unconformably overlain by the Pretoria Group. The latter is a clastic lesser volcanic succession consisting of alternating sandstone, mudrock, conglomerates, volcanics and diamictites that are interpreted as having formed from alternating alluvial sedimentation and epeiric marine conditions (Eriksson, et al., 1993; Moore, et al., 2001). The paleoenvironment of the Pretoria Group is thought to be composed of a mega-cycle of alternating fan, delta fan, lacustrine delta, lacustrine basin and basin lake margin sedimentation as well as increasing amounts of clastic volcanics (Eriksson & Clendenin, 1990). Alluvial sediment deposition was likely tectonically controlled due to subsidence of rift basins which were reactivations of Ventersdorp Supergroup rift zones (Eriksson & Clendenin, 1990; Altermann & Nelson, 1998). This sequence has also been likened to a possible early super-continental breakup (e.g. Vaalbara /Zimvaalbara) (Moore, et al., 2001; Roy, 2006).

In the eastern Transvaal and Kanye basins, the first formation encountered above the angular unconformity is the Rooihoogte Formation. This paleokarstic-infill formation is composed of detrital fragments of chert, dolomitic carbonates and ironstones derived from the Chuniespoort Group (Eriksson, et al., 1993). Although separated by a substantial angular unconformity, Eriksson, et al., (2001) noted a possible genetic relationship between the Duitschland and Rooihoogte, citing analogous source regions and developmental environments.

Overlying the Rooihoogte, the Timeball Hill Formation is composed of carbonaceous mudrocks, rhythmically interbedded ferruginous mudrocks and sandstones (Eriksson, et al., 1993; Altermann & Nelson, 1998; Moore, et al., 2001). Eriksson, et al., (2011) reported the formation contains minor (but widespread) lenticular glaciogenic deposits in the upper areas consisting of diamictites, wackes, conglomerates and shales. A shallow marine deltaic environment is envisaged for the deposition of this formation with pro-deltaic deposition of the carbonaceous shales, turbiditic re-sedimentation of distal deltaic deposits and tidally reworked delta front sands (metamorphosed) as quartzites (Eriksson & Clendenin, 1990). Of note, the chert clasts in the diamictites show a preferential orientation with the long axis of the clasts parallel to regional bedding (and bounding faults), upward fining and decreased rounding of the clastic material. This supports the genesis as a reworking of glacial moraines in a periglacial setting (Eriksson, et al., 1993; Eriksson, et al., 2011).

The Makganyene Formation in the Griqualand West basin is composed of diamictites, iron formation, shales, sandstones and conglomerates which overlie the high angle fault that cuts through the Koegas Subgroup and BIF units down to the carbonate units (Eriksson & Clendenin, 1990). The diamictite was described by Moore, et al., (2001) as having poorly sorted, faceted and striated clasts with overall clast size progressively decreasing to the west. The contact between the Makganyene Formation and the Koegas Subgroup is largely conformable with a gradational contact. Although the average thickness of the formation is 3-70 m there are areas of highly variable thickness up to 500 meters (Eriksson & Clendenin, 1990; Eriksson, et al., 1993). Furthermore, although the striations and faceted grains as well as the appearance of areas of localized glacial pavements suggest a glacial origin, prior work by Eriksson &

Clendenin, (1990) and Eriksson, et al., (1993) suggest only a limited amount of glaciation with extensive marine and fluvial reworking of the deposits.

Correlations of the Pretoria Group and the Postmasburg Group in the formations above the Timball Hill / Makganyene formations becomes increasingly more difficult. The Pretoria Group is poorly dated, with Hannah, et al., (2004) reporting Re-Os dates of detrital zircons from sandstones from the lower, middle and upper Kanye Basin of 2250 ± 14 Ma, 2236 ± 13 Ma and 2193 ± 20 Ma respectively. The Pretoria Group is composed of 10-12 units of alternating successions of mudrocks, sandstones, diamictites, conglomerates and lesser clastic volcanic units (Altermann & Nelson, 1998); whereas the Postmasburg Group has only 4 units that are largely composed of chemical sedimentary deposits (Eriksson & Clendenin, 1990). In the Griqualand Basin, the Ongeluk Formation is overlain by manganese jaspillites (which are generally considered to be of volcanic-exhalative origin) that include the economically important Fe-Mn deposits of the Hotazel Formation and the dolomites of the Mooidraai Formation, which have no direct collation in the Transvaal Basin (Eriksson & Clendenin, 1990; Eriksson & Altermann, 1998; Eriksson, et al., 2011). The relationship between the two groups is perhaps best described as being one of proximal coarse clastics in the north-east to distal chemical sedimentary in the south-west (Moore, et al., 2001).

One of the main stratigraphic markers used to correlate beds across these basins and establish a genetic relationship between the sister basins is the Hekpoort-Ongeluk-Tsatsu Formations (Pretoria-Postmasburg-Kanye basins respectively). Cornell, et al., (1996) recorded a Pb-Pb isochron age for the Ongeluk of 2222 ± 13 Ma and an Rb-Sr age for the Hekpoort Formation of ca. 2184 Ma. However, Moore, et al., (2001) has challenged this genetic relationship between the Hekpoort and Ongeluk lavas citing extensive alteration by metamorphic and/or metasomatic processes that also affected the older Ventersdorp Supergroup. The Ventersdorp yielding whole rock ages of ca. 2150 Ma using Rb-Sr; ca. 2370 Ma using Pb-Pb; and 2693 from U-Pb zircons evidences this. This also included significant authigenic zircons giving ages between 2370-1765 Ma. Dates were originally reported by Armstrong, et al., (1991). Moore, et al., (2001) also noted dates of 2349 ± 26 Ma for the Mooidraai Formation by Bau et al., (1999) and zircon chronology dates of ca. 2521 for the Campbellrand dolomites from Summer and Bowring, (1996) to support their theory that the Postmasburg Group is significantly older than reported.

There is general agreement amongst researchers that two very different environments are envisaged for the deposition of the older Chuniespoort, Ghaap and Postmasburg groups (Altermann & Nelson, 1998; Moore, et al., 2001; Eriksson, et al., 2011). The proposed paleoenvironment for these groups is envisaged as an epeiric sea which spread out over the Kaapvaal Craton well beyond the boundaries of the preserved Transvaal Basin (Eriksson & Clendenin, 1990; Altermann & Nelson, 1998; Eriksson & Altermann, 1998). Sequence stratigraphy from Eriksson & Clendenin, (1990) show the Chuniespoort Sea had at least 2 phases of development. The first phase was characterized by a north-northeast transgressive deposition followed by regression and erosion. The second phase, although composed of a several onlap-offlap sequences, had a much greater extent with conformable deposition from the Transvaal to Griqualand basin. This environment is much more indicative of a stable inter-cratonic or possible super-continental sea starved from clastic input (Moore, et al., 2001; Roy, 2006; Eriksson, et al., 2011).

1.2.3 The Bushveld Complex

Sedimentation and infill of the Pretoria Group ended at ~ 2.05 Ga. This has been shown by compressive deformation of regional scale sedimentary strata (Eriksson & Altermann, 1998). As noted in section 1.2.2 deposition in the Postmasburg Group is truncated by an unconformity and correlation of the thin upper units with the Pretoria sediments is questionable. The end of sedimentary infill of the Transvaal Supergroup was followed shortly thereafter by the regional scale emplacement of the ca. 2.058 Ga Bushveld Complex (Altermann & Nelson, 1998). Emplacement of the Bushveld Complex detached the Rooiberg Group lavas and overlying Loskop Formation from the underlying Pretoria Group creating a lid over the underlying strata (Eriksson, et al., 2001), and due to the central placement of the Bushveld Complex, areas of the Transvaal strata dip at angles up to 20° towards the centre.

1.3 *Geology of the Kalahari manganese field*

The Kalahari manganese field located approximately 60 km north-west of Kuruman (Figure 1-1), is composed of five structurally preserved erosional relics of the Hotazel Formation (Astrup & Tsikos, 1998). The Hotazel along with the Makganyene, Ongeluk and Mooidraai Formations, comprise the Postmasburg Group of the Griqualand West Basin.

These five relic formations of the Hotazel are composed of rhythmically deposited Superior type iron formations intercalated with manganese ore (Astrup & Tsikos, 1998). The deposits form a basin with a strike length of ~41 km and a width of between 5 and 20 km. The total area underlain by the basin is approximately 4,525 km^2 (Astrup & Tsikos, 1998). Borehole observations show there are four distinct units of banded iron formation interbedded with three manganese units (Figure 1-6) (Tsikos & Moore, 1997). Each of the manganese beds forms the centre of a symmetrical iron-formation,-hematite-lutite,-braunite-lutite sedimentary cycle (Gutzmer & Beukes, 1995b).

Two major types of ore are generally recognized (Gutzmer & Beukes, 1995a; Gutzmer & Beukes, 1995b; Tsikos & Moore, 1997; Tsikos, 1999). Low-grade ore, known as Matawan-Type, is thought to be the result of diagenesis and/or low level (greenschist facies) metamorphism. The high-grade ore, called Wessels –type ore, has been altered by hydrothermal and/or supergene processes. The low grade Matawan-type ore accounts for 97% of the resource and high-grade hydrothermally altered Wessels-type ore ~3% (Kleyenstuber, 1984). Mamatwan-type ore contains 30-39% Mn and is microcrystalline with carbonate bedding laminations. The composition reported by Gutzmer & Beukes, (1995b) is finely intergrown braunite, hematite, kutnohorite and magnocalcite with ovoides of manganese bearing calcite. Hausmannite is common as a diagenetic oxidation product that replaces carbonate ovoids. This species of Hausmannite is low temperature and contains up to 4.5% Fe_2O_3 (Neil, et al., 1986). The high-grade Wessels –type ore in contrast contains 46-60 wt.% Mn as coarse crystalline Hausmannite, Braunite II, Braunite (new) (an unofficial name first used by Kleyenstuber 1984 to define compositional and textural characteristics of a member of the Braunite group but not an officially recognized mineral by the IMA commission), and Bixbyite. This ore has been upgraded from Matawan-type ore by both hydrothermal and supergene processes which have removed a substantial portion of the carbonate content and silica (Gutzmer & Beukes, 1995a). The high-grade Wessels-type ore is generally restricted to the northwestern section of the Kalahari manganese field where thrust duplication and normal faulting have affected the strata (Gutzmer & Beukes, 1995a) (Figure 1-7).

The lowermost unit of the manganese is by far the most important economically with virtually all production coming from this zone (Gutzmer & Beukes, 1995a). This bed reaches a maximum thickness at the Mamatwan mine of ~ 45m with the average thickness being 4 to 8 m in the Nchwaning and Wessels mining areas. The middle bed is currently sub-economic as thickness varies from 1-3 meters and is often absent due to varying levels of paleo erosion (Astrup & Tsikos, 1998). The upper manganese body which is approximately 5 m thick has been mined locally and reaches a maximum thickness of approximately 30 m in the southern area of the Kalahari manganese field (Gutzmer & Beukes, 1995a).

1.4 *Context of this study*

In parts of the Middelplaats mine area, the basal Hotazel Formation Mn ores overlie mafic igneous footwall rocks. These have been mapped as Ongeluk lavas (Jennings, 1986). However, in the Middelplaats mine there is textural evidence for modification of the ores and the mafic rocks along the contact. It is therefore unclear whether the contact here is in fact intrusive (in which case the igneous rocks are not, in fact, Ongeluk lavas, and must presumably be younger magma pulses overlying the Ongeluk footwall below), or sedimentary (in which case the alteration represents hydrothermal fluid activity along the unconformity between the Ongeluk and the Hotazel Formations).

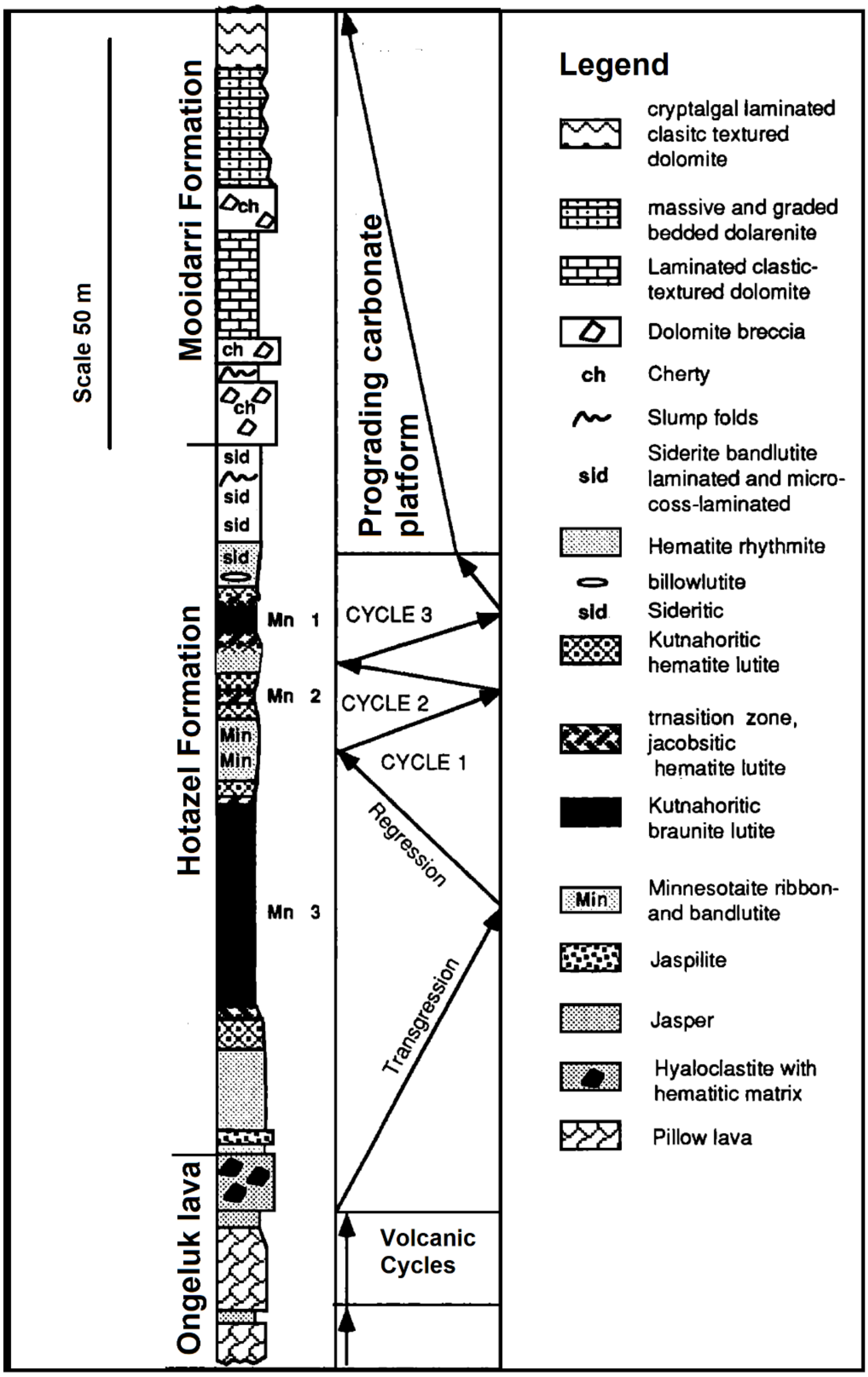

Figure 1-6 Generalized stratigraphy of the Hotazel showing 3 cycles on Mn ore intercalated with BIF as related to sea-level transgression-regression cycles. Modified after Neil, et al. (1986) and Gutzmer & Beukes, (1995a).

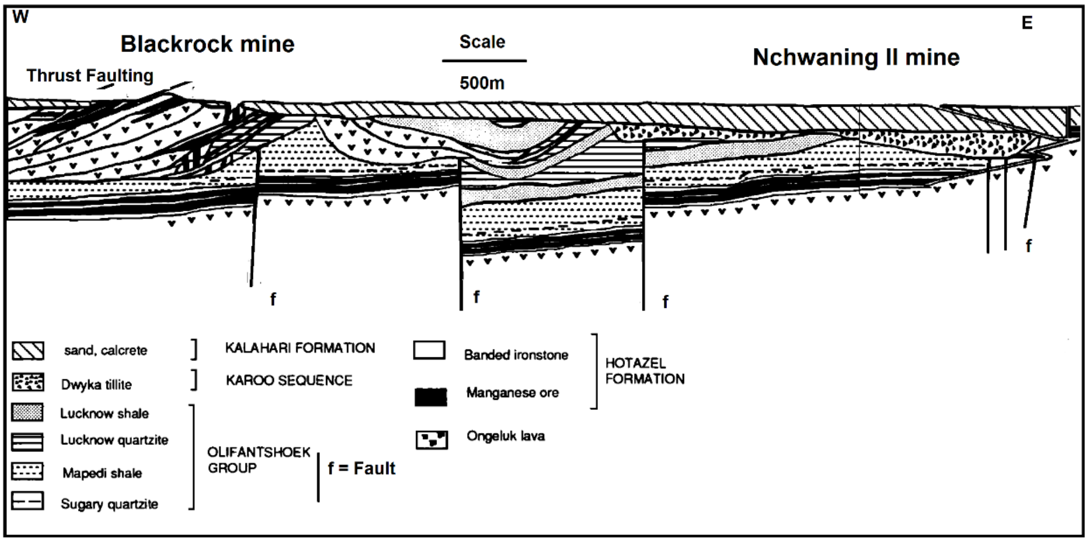

Figure 1-7 Cross-section through the Kalahari manganese field showing thrust duplication and faulting. Modified after Gutzmer & Beukes, (1995a)

1.5 *Project aims and objectives*

The aims of this project are to characterize the nature of the contact between the lowermost manganese ore of the Hotazel Formation in drill holes MP53 and MP54 at the Middelplaats mine with the underlying igneous rocks. Typically, in other mined areas of the Hotazel Formation, the lower most BIF of the Hotazel Formation is in contact with the underlying Ongeluk Formation lavas. This project will attempt to determine if the contact between the manganese ore and the underlying igneous rocks a primary sedimentary contact in which the sediments were emplaced directly on top of the underlying igneous rocks or if the igneous rocks were injected into the semi or wholly consolidated sediments of the Hotazel Formation. The project will also look at what if any effect the underlying igneous rocks may have had on the manganese ore and if there is any relationship to the Ongeluk Formation. Several factors will be investigated:

- Is there a genetic relationship between the igneous rocks underlying the Mn ore in 2 different bore holes; MP53 and MP54 from the Middelplaats mine?
- Is there a genetic relationship between the igneous rocks from MP53 and MP54 and the Ongeluk Formation or do they represent a different pulse of magma?
- Is the contact between the manganese ore and underlying igneous rocks sedimentary or intrusive/metamorphic in origin?

- What is the nature of the alteration of the manganese ore close to the contact with the igneous rock and how does this alteration change with increasing distance from the igneous rocks?
- What if any implications for other areas of the Kalahari manganese field does this contact relationship have?

.

Chapter 2 Formation and Genesis of Manganese Deposits

Manganese is a unique mineral in that it has a relatively high abundance in the lithosphere (~0.1%) (Best, 2003). Manganese also has two valencies (di and tetravalent) which are stable over a wide range of conditions which allows it to be transported from areas of low redox potential to areas that are well oxidized (Deer, et al., 1992). Although the environmental conditions that have allowed manganese accumulation throughout geological time have been researched and evaluated, the local conditions that persisted to produce incipient precipitation of manganese were defined by the evolution of the complex interplay of the hydrosphere, lithosphere and atmosphere (James & Trendall, 1982; Glasby, 1988; Eriksson & Clendenin, 1990; Moore, et al., 2001; Eriksson, et al., 2011). This chapter will look at the evolution of manganese metallogenesis through time and explore the processes necessary to accumulate manganese ore.

2.1 *Manganese metallogenesis*

Manganese ore deposits are generally divided into three types based on the nature of their formation; hydrothermal, sedimentary and supergene. Formation of these deposits from a temporal and spatial view will be reviewed first then review of the associated processes responsible for the differing deposit types.

2.1.1 Archean manganese formation

The formation of manganese deposits was distinctly inhibited during the Archean. This is in stark contrast to the development of associated iron formations. Economic iron formations such as the Isua Supracrustals in Greenland have been dated at ca. 3.8 Ga, whereas economic manganese is considerably younger, appearing in formations such as the Iron Ore Group India at ca. 3.2 Ga (James & Trendall, 1982; Roy, 1988; Roy, 2006). Global distribution of economic manganese deposits in the Archean is quite limited, with only five deposits being identified. Three are in India within the Iron Ore Group ca. 3.2-2.95 Ga and two within Brazil’s 2.8-2.6 Ga Rio das Velhas Series (Glasby, 1988). Sub-economic deposits are known from well-developed Archean terrains in Russia such as the Segan-Zaba limestones and the Khapchensk Serries in the Anabar Massif (Roy, 1988). Greenstone terrains are only known to contain two such deposits; the Rio das Vehlhas Series in Brazil and the Chitradurga Group in India. This would indicate that not only are manganese deposits selective in time but also quite selective in space as well (Roy, 2006).

During the early Archean, the low concentration of oxygen in the atmosphere is considered to have been a major factor in the lack of manganese deposition compared to iron (Roy, 1988; Buhn & Stanistreet, 1997). The differences in solubility between iron and manganese allowed deposition of iron in low oxygen environments whilst manganese stayed in solution (Glasby, 1988; Evans, 1993; Robb, 2005).

Reviewing the depositional settings of these early deposit shows a preference for shallow water intracratonic settings witch had more of a “Proterozoic character” (Roy, 2006); although (not unsurprisingly due to the age) many have been metamorphosed to a greater or lesser extent (Roy, 1988). Granulite facies metamorphism has affected the ~2.6 Ga Eastern Ghats in India and the high-grade region of the ~2.8 Ga Bahia State in Brazil (Sakar, 1980); whilst only incipient metamorphism has affected the ~3.2 Ga Iron Ore Group sequence in India (James & Trendall, 1982).

Several theories have been put forth to explain the paucity of Archean manganese deposits. However, consideration must be first be given to the physical conditions controlling potential areas of ore formation and/or deposition. Late-Hadean to Archean crustal tectonics, atmospheric conditions and basin evolution operated in a considerably different fashion than in the Paleoproterozoic and Phanerozoic (Walter & Tronnes, 2004). Archean to Paleoproterozoic tectonics were dominated by cratonic assemblage, early continental formation (Sleep, 2003), flat or low angle subduction and “flake tectonics” (Smithies, et al., 2003; Smithies, et al., 2009).

Stern (2008) has demonstrated that during the Hadean-Archaean, rapidly circulating, poorly-organized convecting asthenospheric cells would have driven semisolid basaltic proto-crust rafts/platelets against and beneath one another. However, due to the elevated mantle temperatures and the thinness of the slabs produced by small lithosphere-asthenosphere density inversions, these platelets would not be able to be deeply subducted before they were sufficiently heated to negate any negative buoyancy (Smithies, et al., 2007). These changes in buoyancy are thought to be responsible for transgression/regression cycles within the intracratonic basins which affected the formation of manganese deposits (Van Hunen & Van Den Berg, 2008;

Smithies, et al., 2009). The relatively small platelets would also be consistent with the preserved individual Archaean granite-greenstone belts that formed as oceanic crust and were subsequently sutured to primitive island arcs. In addition, some Archaean TTG terrains are thought to have formed when mantle plumes underpinned these primitive island arcs accreting large volumes of material without interaction with either a subducting slab or mantle wedge. This environment of high heat flux, mantle plumes and substantial magmatic outgassing produced large volumes of Mn^{2+} released into marine systems and contributed to oceanic chemistries unique to this time period that inhibited the precipitation of manganese (Roy, 2006; Smithies, et al., 2009).

Roy (1988) contends that in the early stages of cratonic formation the associated volcanogenic/hydrothermal chemical exhalations were rich in Mn. However, unfavourable anoxic conditions prevented large-scale (economic) precipitation of manganese. This is illustrated by the absence of any manganese halo surrounding deposits of Archean age and prominent halos around volcanogenic/hydrothermal massive sulphide deposits from the Proterozoic and younger eras. The extremely selective environments of manganese deposition during the Archean can also be seen in the isotopic chemistry of the few areas of known Mn deposition. Carbonates in the Late Archean (~2.75 Ga) have been shown by Des Marais, (1994) to have a strong negative δ^{13} C anomaly (-35% to -50% PDB). This, along with the high CH_4 content in the Archean atmosphere and evolving oxygen, has been taken as evidence of the presence of methanogenic bacteria. These bacteria consumed CH_4 at the CH_4-O_2 interface close to stromatolitic (carbonate) units. The localized decrease in CH_4 allowed for the development of microenvironments which encouraged the development of oxygen photosynthesis (Des Marais, 1994). These fragile changes in basinal chemistry are thought to be the likely precursors for manganese deposition. However, preservation potential of these areas was extremely low due to supercontinent breakup, mantle overturn and superplume events which may have destroyed other areas of accumulation (Roy, 1988; Roy, 2006; Smithies, et al., 2007).

2.1.2 Proterozoic manganese formation

The Proterozoic era produced by far the most manganese in terms of tonnage of minable ore. This is in large part due to the Kalahari manganese field, which accounts for an astounding 80% of world resources (Table 2-1) (International Manganese Institute, 2013). The massive deposition of manganese during this time period was brought about by substantial changes in the earth's atmosphere- hydrosphere system which allowed the accumulated stores of manganese to be liberated (from solution) and subsequently deposited. One of the key factors that facilitated this change was the oxygenation of the atmosphere (Buhn & Stanistreet, 1997). Oxygen production by cyanobacteria is thought to have begun prior to the "Great Oxidation Event" at ~ 2.45 Ga. Several different lines of geologic evidence support this: organic biomarkers in sediments, carbon isotope patterns and stromatolite morphology (Barley, et al., 2005; Kasting, 2013). However, there was no immediate surface expression of this increase due to substantial existing O_2 sinks (Buhn & Stanistreet, 1997). The actual rise of surface oxygen was brought about by several coincident factors that helped overcome existing O_2 sinks such as reducing gases, organic matter and Fe^{2+} (Roy, 2006). Of particular note is the diminished production of iron formations during the period of ~ 2.4 - 2.0 Ga which has a direct correlation to manganese deposition. Iron as Fe^{2+} is thought to have acted both as a direct O_2 sink and indirectly by helping to remove phosphorus in Archean oceans thereby inhibiting the proliferation of oxygen- producing cyanobacteria (Robb, 2005; Roy, 2006).

This rise in oxygen levels (Kerr, 2005) coupled with the development of the ozone layer which had the effect of stopping the mass-independent fractionation of sulphur at ~ 2.45 Ga changed the balance of marine chemistry and initiated the large scale liberation of accumulated manganese from solution (Kerr, 2005).

The geotectonics of the Proterozoic are also of critical importance to the formation of both iron and manganese deposits. The relationship between volcanic exhalative activity, supercontinent disassembly (rifting) and reorganization have been shown to have a direct relationship on the formation of these deposits. Iron formations in particular have been demonstrated to form in rift-type environments in both the Paleoproterozoic and Neoproterozoic, with most related to continental breakup events (Roy, 1988; Schissel & Aro, 1992; Buhn & Stanistreet, 1997; Roy, 1997; Roy, 2006).

Table 2-1 Resources of manganese listed by age. Data taken from DeYoung, et al., (1984). Glasby, (1988) and International Manganese Institute, (2013)

Estimated manganese resources by geological age		
Age	Location	Million tonnes of Mn
Archean	Hsiangtan deposits (China) >	4.5
	Wafangtzu district (China)	0.7
Proterozoic	Tambao deposit (Upper Volta)	9
	Azul deposit (Brazil)	24.7
	Moro da Mina deposit (Brazil)	1.4
	Serro do Navio mine (Brazil)	8.9
	Urucµm mine (Brazil)	27.3
	Moanda mine (Gabon)	96.8
	Nsuta mine (Ghana)	6
	Andhra Pradesh State (India)	0.6
	Goa State (India)	3.2
	Gujarat State (India)	> 1.2
	Karnataka State (India)	4.4
	Madhya Pradesh and Maharashtra State (India)	22.3
	Orissa State (India)	12.4
	Kalahari field (South Africa)	5026.3
	Postmasburg field (South Africa)	5.8
Early Permian	Leiping district (China)	
	Tsunyi district (China)	> 2.0
Early Jurassic	Urkut district (Hungary)	44.1
Late Jurassic	Molango mine (Mexico)	523.6
Early Cretaceous	Groote Eylandt mine (Australia)	152.9
Late Cretaceous	Inimi mine (Morocco)	0.7
Oligocene	Varna district (Bulgaria)	5
	Bolshe Tokmakdeposits (Russia.)	203.5
	Nikopol deposits (Russia)	144.1
	Tchiatura deposits (Russia)	38
Holocene	Western Transvaal deposits (South Africa)	3.7
		Total 6376.1

There is a large body of evidence that suggests that the development of manganese (and iron) formations are directly related to marine transgression events, although the depositional settings changed substantially from the Precambrian to Phanerozoic (Buhn & Stanistreet, 1997).

Marine transgressive-regressive cycles during the Proterozoic can be related to two dominant factors: the formation of continents/ super continents and glaciation events that were brought about by the changes in atmospheric composition coupled with these tectonic events (Buhn & Stanistreet, 1997).

Formation of continents and supercontinents has been demonstrated to have a profound effect on the lithospheric heat budget by acting as heat reservoirs (Buhn & Stanistreet, 1997). The localized build-up of additional heat causes the continental assemblage to be uplifted isostatically and the beginning of the continental assemblage/dissemblage cycle to commence (Evans, 1993). Isostatic uplift initially causes a local marine regression as well as extension within the associated continental assemblage. Extension, however, eventually leads to rifting and continental breakup. The smaller assemblages allow heat to dissipate more quickly which in turn results in thermal sag; thus facilitating a marine transgression (Gurnis, 1988). Additionally, weathering of the newly exposed rock surface serves to reduce available $CO_{2.}$ The culmination of these interrelated events leads to atmospheric forcing which ultimately results in a cycle of glaciation coupled with centennial assemblage/breakup and sea-level changes common to the Proterozoic (Buhn & Stanistreet, 1997).

Glaciation events were widespread during the early Proterozoic (ca. 2.45-2.22 Ga.), with glaciated sequences correlated between the Huronian Supergroup, in Canada, Transvaal Supergroup South Africa and the Hamersley Megasequence of Western Australia (Roy, 2006). As noted earlier the assemblage of the inferred supercontinents such as Vaalbara /Zimvaalbara and Kenorland would have resulted in an upwelling of the mantle and a geoid high before breakup. This geodesic high is envisaged to have increased the freeboard areas which resulted in extensive development of platform carbonates and surface (continental) weathering, which resulted in a massive drawdown in CO_2 levels and ultimately the drop in global temperatures that initiated the glacigenic events (Young, 1991).

The interplay of these two cycles, continental assemblage/ dis-assemblage and glaciation, produced a complex feedback loop (Figure 2-1) during the Proterozoic. This resulted in multiple cycles of oxic-anoxic/transgressive-regressive seas, which allowed for the accumulation of large quantities of manganese in anoxic environments followed by the deposition of the manganese in oxic generally shallow continental shelf environments (Calvert & Pedersen, 1996; Buhn & Stanistreet, 1997; Roy, 2006).

The cyclical changes in the atmosphere-hydrosphere along with rapidly changing cratonic assemblages during the early Paleoproterozoic allowed for the release and deposition of massive quantities of manganese that had been stored in solution during these transgressive-regressive events (Calvert & Pedersen, 1996). The Hotazel Formation of the Kalahari Supergroup is quite possibly the best example of the cyclicity during this time period. The Hotazel Formation consists of four distinct BIF units interbedded with three manganese layers which correspond to repeated transgression-regression cycles (Tsikos & Moore, 1997). The Hotazel Formation in particular also shows evidence of early glaciation. The formation (Figure 1-6) begins with a volcaniclastic sandstone that is followed by a 50-100 cm thick BIF which contains glacigenic drop stones that are indicative of rapid deglaciation from the Makganyene icehouse state. Kirschvink, et al., (2000) also noted that the presence of this dropstone bearing unit within the base of the Hotazel Formation can be taken as proof the glaciation outlasted the Ongeluk volcanism.

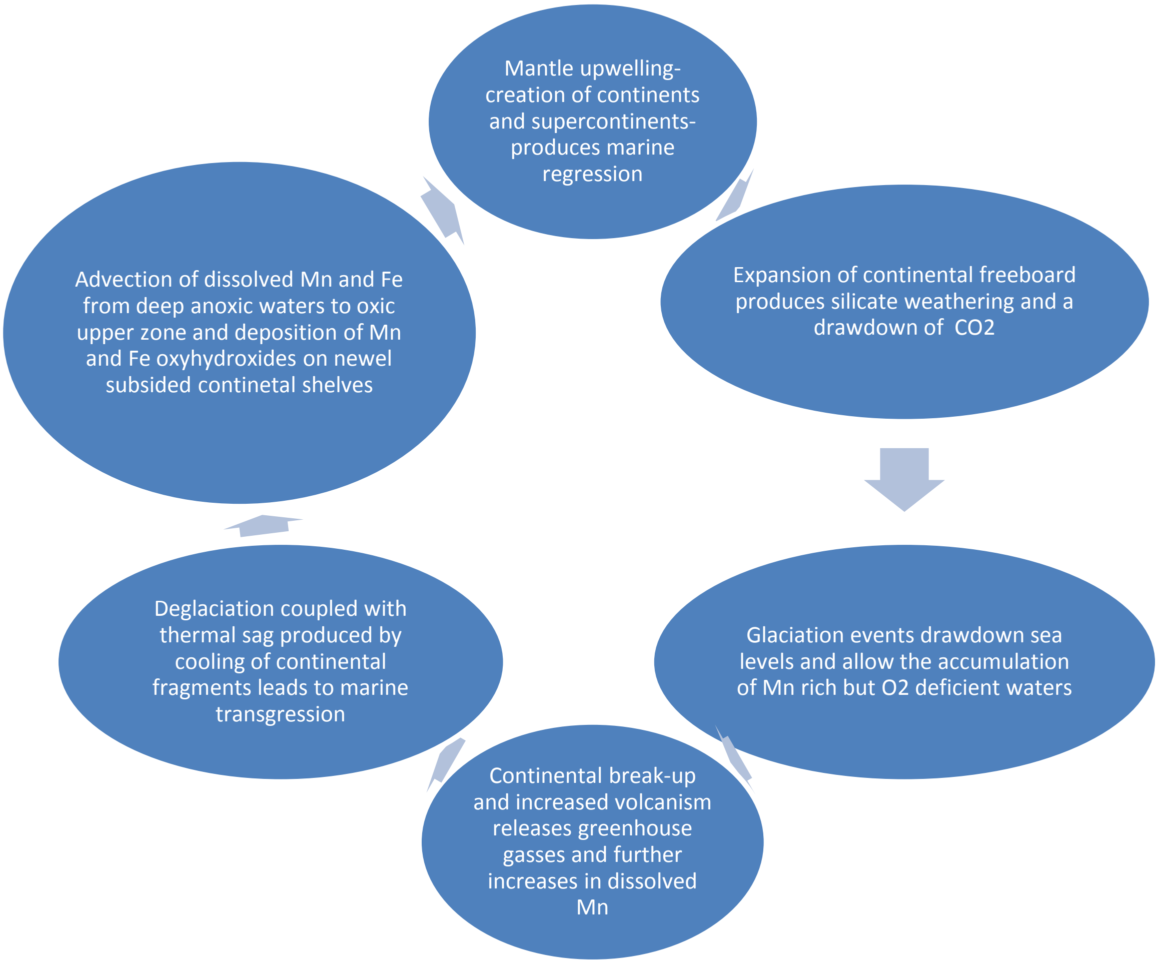

Figure 2-1 Schematic representation of the relationship of continental formation, breakup, glaciation and sea-level changes which resulted in Mn deposition in continental shelf settings during the Proterozoic. Modified after Roy, (2006)

2.1.3 Phanerozoic manganese formation

Phanerozoic manganese metallogeny, although quite diverse in depositional environments, is considered to have operated in a fashion similar to contemporary (i.e. Quaternary) environments. Quaternary deposits tend to be associated with deep-water spreading centres whereas during the Proterozoic the vast majority of deposits occurred in shallow water shelf environments (Glasby, 1988; Evans, 1993; Buhn & Stanistreet, 1997; Roy, 1997). As with prior eras, plate motions and the resulting environments controlled the depositional settings of manganese. By far the largest accumulations of manganese during this period were associated with divergent plate margins and spreading centre volcanogenic activity similar to those seen near black smokers close to the current day Mid Atlantic Ridge (Roy, 1988). Climatic changes during the Phanerozoic also had significant effect on the accumulation and deposition of manganese by causing glaciations, which resulted in cycles of marine transgression/ regression. The advancing and retreating glaciers also acted as a transport depositional mechanism for previously deposited terrestrial manganese (Roy, 2006).

During the Phanerozoic pO_2 levels in the hydrosphere and atmosphere began to approach current levels (Roy, 1997). However, during this period there were various times of substantial climatic change. Berner (1991) used $\delta^{13}C$ values to demonstrate that volcanism and other geological and biological processes produced greenhouse gasses which resulted in global warming and cooling periods. Berner (1991) also showed that the Early Paleozoic and Mesozoic were characterized by a warm climate where as colder climates prevailed in the Late Paleozoic and Late Cenozoic. During these warm intervals the oceans were once again stratified, allowing the build-up of manganese in anoxic environments (Berner, 1991).

2.1.4 Sources of metals and fluids

The basic model of transgressive/regressive sea level accumulation and deposition of manganese carbonates was explained by the “manganese pump” model put forth by Calvert & Pedersen (1996). They suggested that sedimentary concentrations of solid phase manganese oxyhydroxides and manganese carbonate originally accumulated under oxic bottom water conditions where preservation of these oxides was made possible by the very low or zero levels of dissolved oxygen (Figure 2-2). Under these conditions manganese carbonate precipitation is primarily controlled by the high level of dissolved Mn^{2+} in pore water which in conjunction with dissolved bicarbonate will exceed the solubility product of manganese carbonate (Roy, 2006). This accumulation of Mn^{2+} is only possible in an O_2 stratified basin where manganese oxyhydroxides are predicated from overlying oxygenated seawater in basinal margins and subsequently buried to a reducing zone below where upon dissolution a high level of Mn^{2+} could be obtained. The highest levels of surficial oxyhydroxides tend to be found on the continental margins where rapid accumulation of organic matter leads to the complete consumption of oxygen at shallow depths within the sediments (Roy, 2006). The continuous burial of organics and their removal of available oxygen then supports the active recycling of the buried oxyhydroxides and hence the secondary enrichment of the oxic horizons in manganese from the supply of dissolved manganese by diffusion from the deeper levels (Calvert & Pedersen, 1996; Robb, 2005).

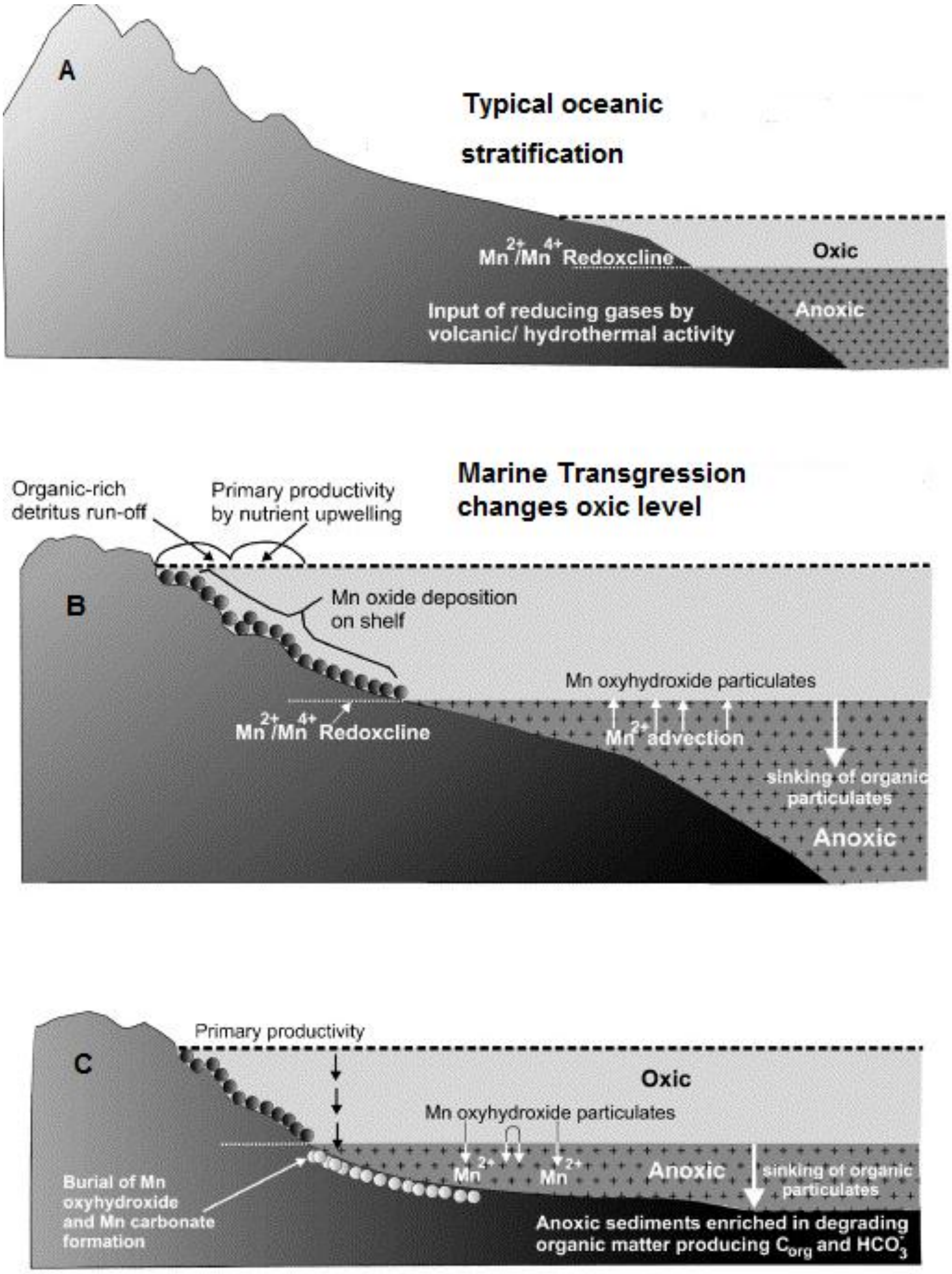

Figure 2-2 Deposition of manganese related to the change in sea level with associated changes in oxidation states. A) Lower anoxic areas accumulate Mn; B) Change in sealevel brings Mn saturated waters onto continental shelf areas and deposition of manganese oxides; C) Mn oxyhydroxides and organic carbonates are buried in a reducing environment allows the formation of Mn carbonates such as rhodochrosite and/or kutnohorite. Modified after Roy (2006)

Chapter 3 Materials and Methods

3.1 *Sample collection*

This study is a continuation and expansion of prior work by Mr Bavulelu Qutu (2009) and Dr Harilaos Tsikos's Manganese Research Group, Rhodes University. Field collection of samples was conducted by Mr Qutu in 2009 at the Hotazel mine. Two drill cores MP53 and MP54 (Middelplaats) were sampled at intervals of 30 cm over a distance of approximately 15 meters of depth. These cores intersected the BIF layer at the top of the sampled section and continue through to the lowermost manganese layer and into the underlying igneous rocks (Figure 3-1). Of the 24 samples collected in 2009, 6 ¼ core samples were selected for re-examination: MP53_S1, MP53_S2, MP54_S1, MP54_S2, MP54-CS3 and MP54-515. Samples MP54-CS3 and MP54-515 were presented as polished thin-sections with no accompanying ¼ core off cuts. This sample set was supplemented by 2 samples (MP54_567, MP53_BIF_S1 and a replacement of the missing core form MP54-515) collected by Dr Tsikos during field work in September 2013 at which point these cores were re-logged. Unfortunately, no remnant ¼ core could be located for the sample from the contact between the Mn ore and underlying igneous rock (MP54-CS3) due to destructive testing methods used during the prior studies. Therefore, all information on this area is limited to visual microscopy and microprobe analysis of the 2009 polished thin-sections. GPS locations of the drill hole were not disclosed due to confidentially agreements with the mine owners as ongoing research may lead to further economic development. However the distance between drill holes is reported to have been in the order of a few hundred meters (H. Tsikos personal communication) and visual correlation of adjacent drill cores is suggestive of a continuous lithology with only local paleo topographical differences and minor tectonic disturbance imparting depth differences of laterally similar lithologies.

Manganese ore samples were collected immediately above the contact with the igneous rock and several meters further above with the intent to measure the difference in metasomatic alteration if any within the Mn ore. Sample MP54-515 was located within 25 cm of the igneous rock whilst MP54-567 was collected 5 meters further up section (Table 3-1). For comparative purposes these will be referred to as Middelplaats "high-grade" (MP54_515) and "low-grade" (MP54_567) ore.

Polished thin sections for both sample groups (2009 and 2013) were prepared in the laboratory at Rhodes University, South Africa. Samples MP54_S2 and MP54-CS3 from 2009 were tested and the thicknesses were~ 95 µm and 85 µm respectively. These samples were re-ground and polished bringing the thickness to ~30 µm to facilitate optical microscopy. The 2009 sample MP54_S2 was used for microprobe examination before re-grinding (for proper optical examination) which ensured for consistency in chemical evaluations with the prior study. This was done in recognition that the thickness which rendered the sample unreliable visually would not affect the microprobe data.

Rock powders from the 2009 samples were discarded. Fresh powders for all samples were re-ground during this study from ¼ core off cuts in the method described below to ensure environmental variables were consistent.

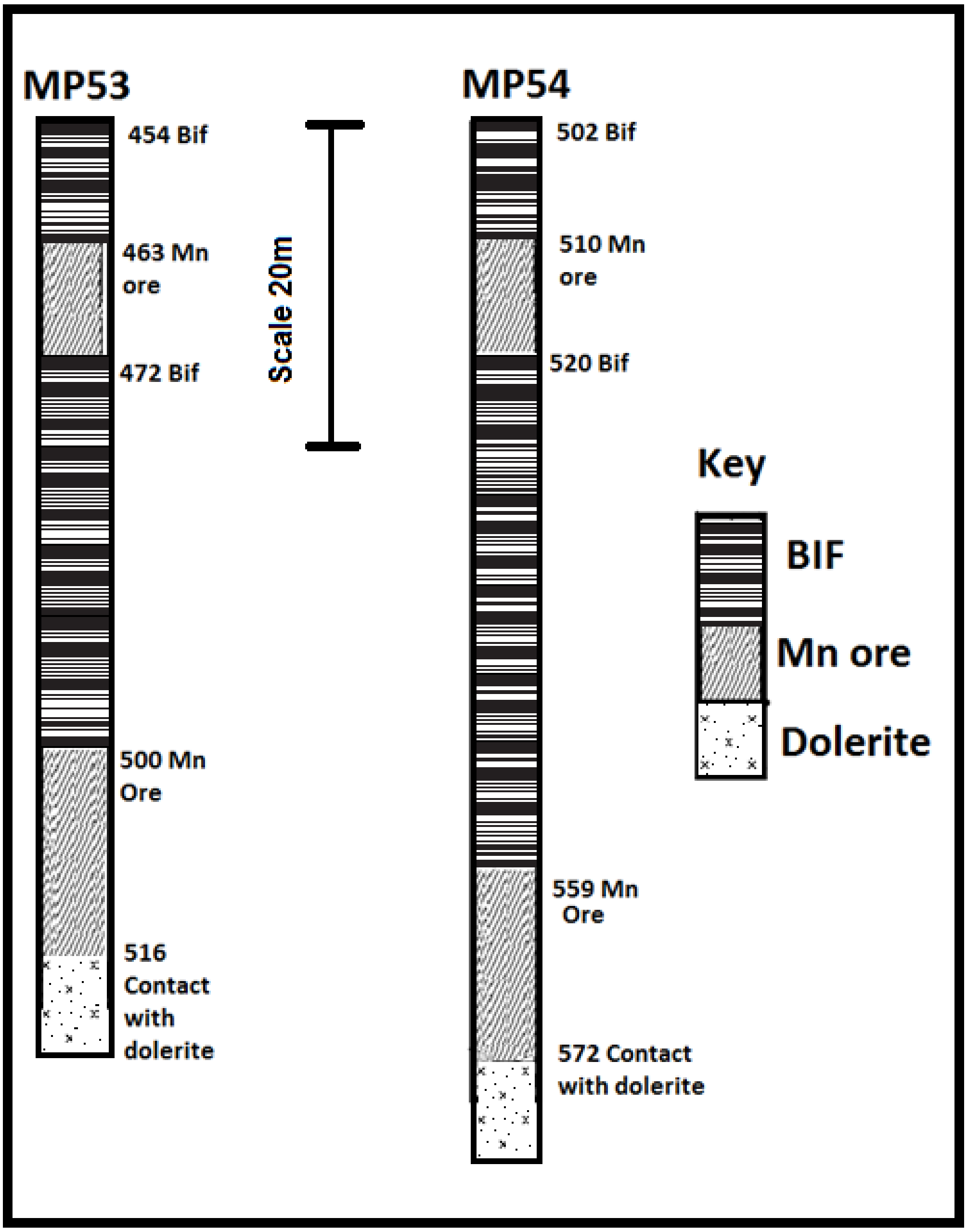

Figure 3-1 Simplified stratigraphic profile of the Middelplaats drill holes MP53 and MP54. Exact sample depths are shown in Table 3-1. Depths of lithological contacts are in meters.

3.1.1 Thin-section preparation

All thin-sections were prepared in the laboratory at Rhodes University, South Africa. Thin-sections from the Qutu (2009) sample suite were checked with a micrometer to ensure a standard thickness of 30 µm. Samples with variations of < 5 µm were re-polished. New ¼ core samples were inspected for optimal locations that would produce the most homogeneous representation of mineralogy. Areas that would produce bias by inclusion of such things as quartz or calcite veins and/or unusual mega-cryst were avoided. Areas where permanent marker ink had penetrated the pore space of the rock were avoided and/or ground off to prevent inclusion of the ink components in the trace element analysis.

3.1.2 Geochemical sample preparation

All ¼ core samples were cleaned to remove any surface oxidation and or paint/ink used during the labelling processes. Rocks were initially broken into 3-4 cm pieces by hammer whilst resting on a cleaned wooden block. The small rock chips were then washed to remove any particles of wood that may have been inadvertently deposited on the surface during crushing. Approximately 40- 50 g of rock chips were weighed out then placed into a large a high carbon steel swing mill vessel. The vessel was placed into a Herzog swing mill for 90-120 seconds allowing the rock chips to be reduced to a fine powder. The resultant powders were collected from the vessel by scooping directly in to pre-sterilized test tubes. The Herzog swing mill was vacuumed and wiped down in between each crushing. The steel vessel was washed with soap and water and dried to remove any of the previous sample. Thirty to forty grams of pure quartzite were then placed in the vessel and allowed to run for 120-180 seconds to clean the inside of any possible remaining contaminants. The vessel was then re-washed to remove the quartzite with soap and water then rinsed with distilled water. Finally, the surfaces were wiped with ethanol and/or acetone to ensure no trace elemental contamination between samples. This process was repeated between each sample as well as a general serialization of all work surfaces in a similar manner. A clean sheet of glossy white paper was used to cover work surfaces for each sample and discarded during cleaning. The composition of the swing mill vessel is listed as “C - 0.90%, P – 0.30%, Mn 2.00% and Si 0.2%.” No notable contamination was detected during analysis of results.

Each powdered sample was then further processed in a Fritsch Pulorisette agate mill for an additional 15-30 minutes to reduce the particle size to maximum of -300 µm. The agate mill was dissembled and washed using the technique described above between each sample. Collection was into new cleaned test tubes also as above.

3.2 *Major oxide (bulk rock) analysis*

Samples were analysed for chemical composition by X-ray Fluorescence Spectrometry (XRF) using the techniques of Norrish & Hutton (1969). Silica crucibles were thoroughly cleaned and dried at 110º C for 30 minutes in a Labotec oven to remove any remnant water. The crucibles were then weighed using a high precision Mettler AE100 scale and weights recorded to 4 decimal places (e.g. 2.0081 g). Approximately 2g of rock powder was then placed into the crucible and re-weighed (to 4 decimal places) to determine the exact amount of rock powder used (See Appendix Table 1 for exact weights for this entire procedure). These crucibles were stored in a desiccator whilst other samples were being weighed. Once all samples were completed they were placed in the oven at 110º C and dried overnight. The crucibles and rock powder were then re-weighed to determine the loss of absorbed water. Samples were then placed in a Labcom L-1200 furnace for a minimum of 12 hours. Igneous samples were processed separately from manganese samples. Igneous rocks were heated to 1000º C whilst the manganese ore to 950ºC. After heating the samples were removed from the oven and allowed to cool in a desiccator before being re-weighed to determine the loss on ignition (LOI) weights.

Core Lithology; Reported at logging	*Sample Name*	Hole # MP53	Lithology from examination	*Sample Name*	Hole # MP54
		Depth in m			*Depth in m*
UBIF (T.O.H)		454			502.28
µMn-UBIF		463.45			510.75
LBIF-µMn		472.5			520.03
LMn-LBIF		500.7			559.57
			Low grade Mn ore	*MP54-567*	567
			High grade Mn ore	*MP54-515*	572.55
Sill-LMn		516.15	Contact between Mn ore and dolerite	*MP54-CS3*	572.8
	MP53_BIF	516.6	BIF xenolith within dolerite material		
	MP53_S2	517.9	Dolerite	*MP54_S2*	575.5
	MP53_S1	519.65	Dolerite	*MP54_S1*	577.4
Dolerite (E.O.H)		520.18			577.77

Table 3-1 Sample list with field lithologies. Samples are displayed in order by drill hole to show stratigraphic relationships. Please note sample list is not to actual scale.

Fusion disks for major element analysis were prepared by combining the ashed rock powder, $NaNO_3$ and Spectroflux, which had also been dried in the oven overnight at 110^{o}C to remove any free water in the following proportions. (Spectroflux is spectroscopically pure and contains weight percent quantities of lanthanum oxide).

Sample	0.2800 g
Spectroflux	1.5000 g
$NaNO_3$	0.0200 g

The combined material was then put into a platinum crucible and melted over a standard gas burner for approximately 10-20 minutes until the melt appeared homogeneous. The molten glass was then poured onto a carbon mould and pressed into a round diskette. These diskettes were then allowed to anneal overnight in a Labcom annealing plate before removal and labelling for testing.

The platinum crucible was cleaned between each usage by first filling it with Na_2CO_3 and placing it over the flame until well melted. The molten sodium carbonate was run around inside the crucible to attack and remove any adhering glass. This liquid was then poured off quickly and the crucible placed into dilute hydrochloric acid which dissolved any remaining carbonate. The crucibles were then washed and cleaned with the standard method of cleaning listed above.

Analysis of the glass disks was performed on a Philips PW1410 XRF machine by Professor J.S. Marsh using the K-alpha line for each of the major elements. Corrections for background were made by counting disks made from “blank” materials in the same fusion mixture at the analyte peak positions. Volatile constituent were determined by loss on ignition calculations during furnace heating. Inter-element absorption and enhancement effects have been corrected by iterative calculations using the factors given in Norrish & Hutton (1969). International rock standards (Appendix B) were employed for calibration and accuracy.

3.3 *Trace element analysis*

Trace element analysis was also carried out by XRF using the methods of Norrish & Hutton (1969) and Norrish & Chappell (1967). Briquettes were made by taking 5-6g of the finely ground rock powders and combining it with 2 to 3 drops of Mowiol solution which acts as a binding agent. This powder was then placed into an aluminium tube resting on a high carbon steel puck and pressed into a circular pellet. The tube was removed and excess powder removed. A larger steel tube was then placed over the pellet and 15 g of boric acid was pored over the pellet to encase it and provide a broader. A steel rod was then inserted on top and the powders pressed to 12 tonnes of pressure for a period of not less than 1 minute which allows the consolidation of the powders and formation of a coherent briquette.

Analysis of the briquettes was performed on the Philips PW1410 XRF at Rhodes University by Professor J.S. Marsh. The K-alpha spectral line was used for most elements but the L spectral line was used for La, Ce, Nd, Th and U. Data reductions techniques were used for the correction of dead-time, instrumental drift, count rate, differences produced by sample position within the sample holding carousel, determination of background and its removal, and correction for interferences from other spectral lines and impurities in the X-ray tube anode. Additional background corrections were performed in the manor provided for by Norrish & Chappell (1967) as discussed in Duncan, et al., (1984).

3.4 *X-Ray Diffraction Analysis (XRD)*

X-Ray Diffraction analysis was performed on the two manganese samples by Tanya Dreyer, Senior Scientific Officer at the University of Cape Town. This additional method was used as optical recognition of the various manganese oxides as well as the extremely fine grained nature of the carbonate and silicate minerals within the samples is quite difficult. A small amount (less than 1g) of each manganese ore sample which had been finely ground into a powder of -300 µm using the Fritsch Pulorisette agate mill for the XRF trace element briquettes was used for the XRD analysis. These powders were placed in a sample holder and loaded into a Philips PW 1390 XRD for analysis at the Department of Geological Sciences, University of Cape Town (UCT). This machine uses a copper K-α X-Ray tube with x-ray wavelength of 1.540560 A. Accelerating voltage= 40kv and current=25mA. Bragg 2Θ angles between 5.01 and 64.96° were used for analysis. A continuous scan step size of 0.02° was applied with a scan step time of 0.4s. The resultant XRD pattern of two theta vs. intensity was used to calculate the d-spacing of the most intense peaks by solving for the Bragg equation. Values of 37.4900 for 2 theta and 18.7450 Omega were used.

Spectral analysis was done using the University of Arizona’s Rruff project software program, (Crystlsluth, 2008, James, et al., 2003). Powder diffraction spectra data was also obtained from the Rruff program spectral library (Downs, 2006). Samples were checked for all common manganese ore minerals and associated gangue minerals, which at a minimum included:

- Aeginine
- Andradite
- Augite
- Barite
- Bixbyite
- Braunite
- Brucite
- Calcite
- Clinochlore
- Dolomite
- Friedelite
- Gaudefroyite
- Hausmannite
- Haematite
- Jacobsite
- Kutnohorite
- Magnetite
- Pectolite
- Specularite

3.4.1 XRD spectral pattern analysis

The Rruff spectral library contains several different powder diffraction patterns for any given mineral. When available analysis from minerals located within the Kaapvaal craton or larger African continent were selected for comparison to aid in the accuracy of analysis.

Analysis of the calibration of the XRD patterns shows some samples are systematically offset (generally to the left) from the known standards. This is likely due to Bragg 2Θ angles of the UCT machine being slightly offset compared to the Rruff standard. The Rruff project uses 5 to 90 degrees 2 theta at 2.0 seconds per 0.010 degree step at 25 degrees C (slightly different than the UCT system). This is compensated for by checking peak positions and cell refinement data.

3.5 *Electron microprobe analysis*

Scanning electron microprobe (EPMA) data acquisition was performed at Rhodes University, Department of Geology, on a Jeol JXA 8230 Superprobe, using 4 wavelength dispersive spectrometers. The analytical conditions employed were: acceleration voltage of 15 kV, probe current 20 nA and spot beam size (< 1 micron). For each element, the quantitative analysis was run at 10 sec counting time on peak and 5 seconds on each upper and lower background, respectively. Natural standards were used.

The standards suite used for measuring the characteristic Kα lines were slightly adjusted for silicate, carbonate (Table 3-2) and oxide minerals (Table 3-3).

Table 3-2 Silicate and carbonate standard list

Element	Standard name	Mass(%)	ZAF Fac.	Z	A	F
1 Na_2O	Albite_SPI	11.5900	5.5020	10.7239	0.5109	1.0041
2 SiO_2	Olivine_SPI	41.5800	2.8511	4.4023	0.6476	1.0000
3 CaO	Cr_Diopside_SPI	25.5000	0.8676	0.9360	0.9265	1.0005
4 Cr_2O_3	Chromite_SPI	45.6500	0.3565	0.3587	0.9771	1.0172
5 MgO	Periclase_SPI	100.0039	5.4678	7.8316	0.6982	1.0000
6 Al_2O_3	Kyanite_SPI	62.9200	4.4417	5.8542	0.7537	1.0066
7 FeO	Almandine_SPI	23.2700	0.1990	0.2024	0.9830	1.0000
8 K_2O	Orthoclase_SPI	15.9600	1.0761	1.2041	0.8936	1.0002
9 TiO_2	Rutile_SPI	99.9834	0.5904	0.6060	0.9742	1.0000
10 MnO	Rhodonite_SPI	42.3000	0.2677	0.2737	0.9782	1.0000

Table 3-3 Oxide element standard list

Element	Standard name	Mass(%)	ZAF Fac.	Z	A	F
1 SiO_2	Kaersutite_SPI	40.0900	2.9956	4.4250	0.6766	1.0005
2 CaO	Cr_Diopside_SPI	25.5000	0.8676	0.9360	0.9265	1.0005
3 Cr_2O_3	Chromite_SPI	45.6500	0.3565	0.3587	0.9771	1.0172
4 MgO	Olivine_SPI	50.4300	4.8491	7.8682	0.6144	1.0032
5 Al_2O_3	Orthoclase_SPI	16.8800	4.2890	5.8730	0.7188	1.0159
6 FeO	Hematite_SPI	89.6933	0.2140	0.2169	0.9864	1.0000
7 MnO	Rhodonite_SPI	42.3000	0.2677	0.2737	0.9782	1.0000
8 TiO_2	Rutile_SPI	99.9834	0.5904	0.6060	0.9742	1.0000
9 V_2O_3	V_SPI	146.8200	0.5082	0.5216	0.9741	1.0000

For element concentration below 5%, a large diffracting crystal with high sensitivity was used for quantitative analysis. The ZAF matrix correction method was utilized for quantification.

3.5.1 Acknowledgments

The use of Jeol JXA 8230 Superprobe, instrument sponsored by NRF/NEP grant 40113 (UID 74464) is kindly acknowledged.

3.6 *Analytical chemistry*

Calculations of cations, Fe_2O_3, Mn_2O_3 and end members for garnets, pyroxenes and feldspars were performed by standard stoichiometry using the methods listed in Deer, et al., (1992) and verified by Minpet 2.02 software provided by Dr Rene Pierre Menot, University of Jean Monet; Saint Etienne, France.

Chapter 4 Petrography Results

4.1 *Petrography results: X-Ray diffraction analysis (XRD), scanning electron microprobe (EPMA) and optical mineralogy*

Optical and microprobe analysis were done on all thin section samples. Additionally XRD analysis was performed on the two manganese ore samples from the Middelplaats mine to supplement microprobe and optical analysis in the identification of the mineral phases. The results are presented in this chapter as a multi-disciplinary approach was needed to properly identify the various minerals. Optical identification of all minerals was complicated by substantial alteration of the igneous material and the fine grain size of the manganese ore minerals.

Representative elemental mineral compositions from the analysed samples are presented from available microprobe data as well as end members that were calculated by stoichiometry where appropriate. Please note all analysed samples were taken from within 1.5 meters of the contact zone between the igneous material and the manganese ore. Normal mineral composition may vary from published norms due to the effects of the pervasive alteration and the intermixing of the igneous material with the manganese ore. All microprobe data including additional images are attached in electronic format (Appendix E) in the accompanying CD/DVD due to the large number of records.

4.1.1 Middelplaats high-grade ore sample MP54_515

Four mineral phases were positively identified by microprobe, XRD and optical microscopy. Representative mineral compositions from the microprobe are displayed in Table 4-1 and XRD powder diffraction patterns in Figure 4-1. The confirmed minerals are:

- Hausmannite
- “Ferroan” – Hausmannite (See Table 4-1 for mineral composition)
- Calcite
- Andradite

A probable identification was also made of the magnesium oxide mineral brucite, (Figure 4-1), although this was in only trace (<0.1%) amounts.

Microprobe analysis (Figure 4-2 and Figure 4-3) and optical analysis (Figure 4-4) reveal a very fine-grained (~0.1mm) mineral assemblage made up of almost entirely hausmannite. Grains are consolidated into groups (blebs) up to 0.2- 0.3 mm with intercalated calcite and andradite. Virtually all the grains display a skeletal lath like and/or bladed replacement texture. The core of the minerals is generally ferroan-hausmannite (greater than 25% Fe, primarily as Fe_2O_3) with infilling (laths/blades) of Fe-poor “pure” hausmannite. Some relic millimetre scale bedding was observed in the ¼ core off cuts and thin-section (Figure 4-5). Mineral composition less than 100% for brucite and calcite are due to the high content of CO_2 and H_2O respectively which the microprobe does not calculate. The totals reported for these minerals are within the ranges one would expect based on chemical formula and examples from Deer, et al., (1992).

Elemental maps of Mn, Fe and Si (Figure 4-6) show iron is concentrated in the centre of the individual grains whilst manganese is concentrated in the laths. Silica is almost exclusively located within the intergranular space between the manganese oxides.

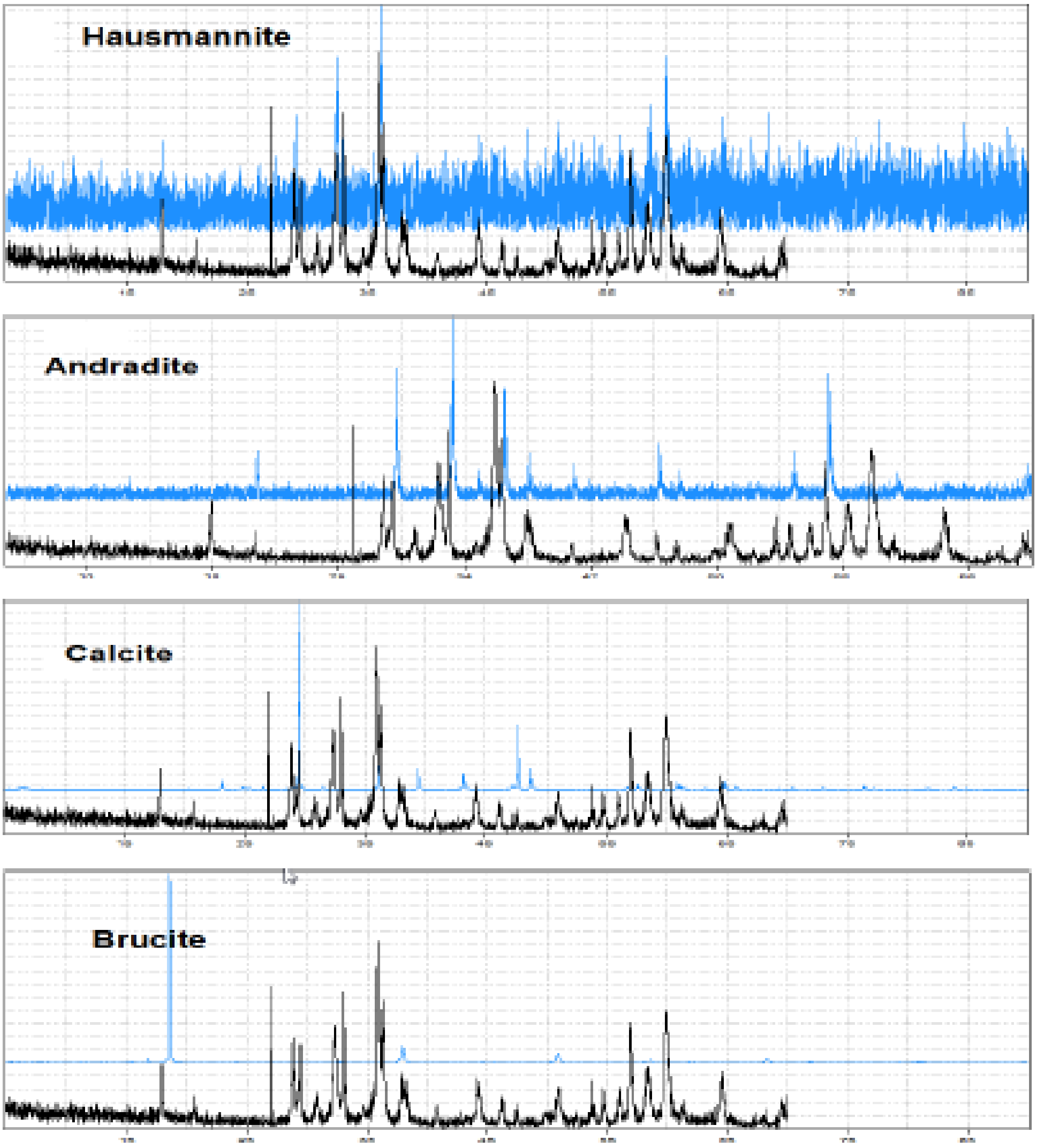

Figure 4-1 XRD powder diffraction patterns from identified minerals in Middelplaats high-grade ore, sample MP54_515. Key sample pattern in black and identified mineral in blue.

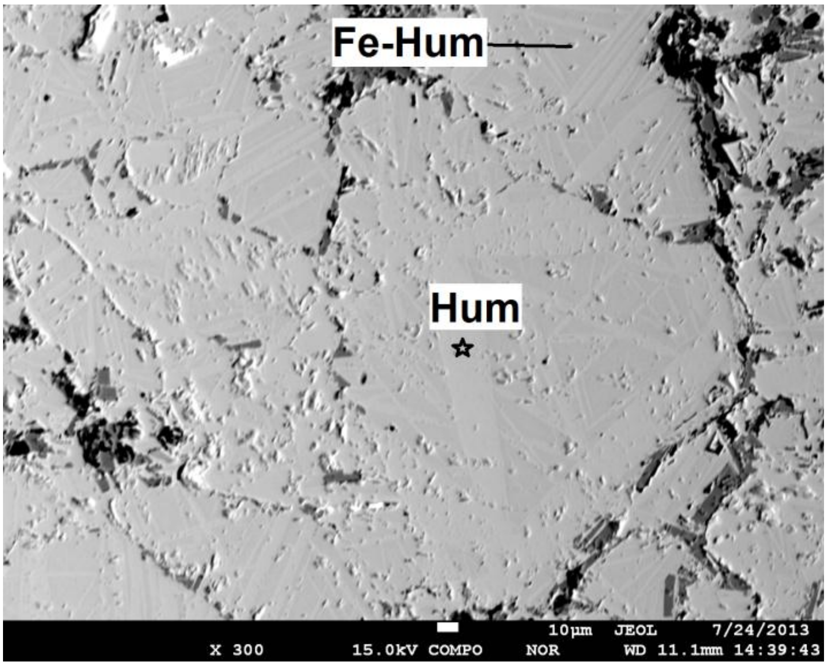

Figure 4-2 Microprobe image of MP54_515 showing hausmannite and ferroan hausmannite. The ferroan areas are the slightly darker cores of the minerals with the lighter laths being pure hausmannite. Key Hum= Hausmannite; Fe-Hum= ferroan-hausmannite.

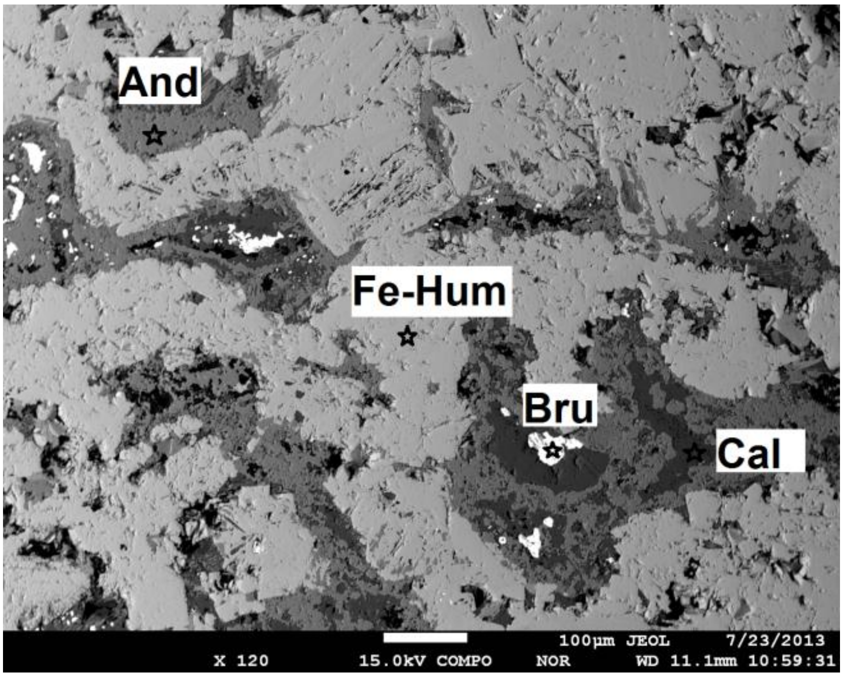

Figure 4-3 Microprobe image of MP54_515: Micrograph shows the infill between manganese grains is composed largely of andradite and calcite with minor amounts of magnesium oxide (likely brucite). Key: as above and: Cal=calcite; And=andradite; Bru=brucite.

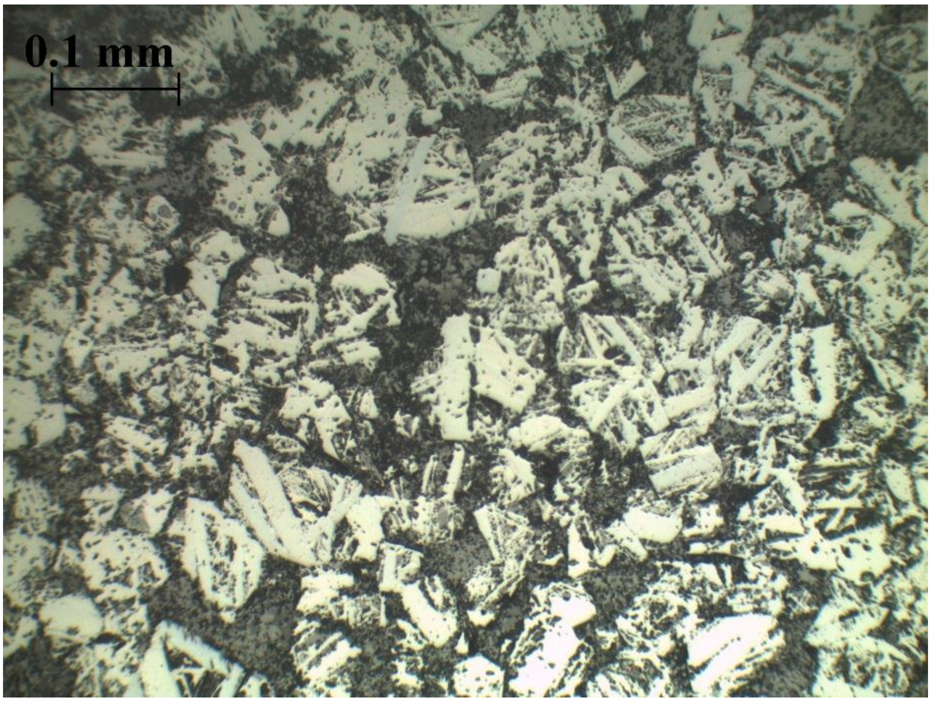

Figure 4-4 Optical micrograph in reflected light of MP54_515. Image shows "regular" and "ferroan" hausmannite. Note the skeletal (bladed) replacement-type texture.

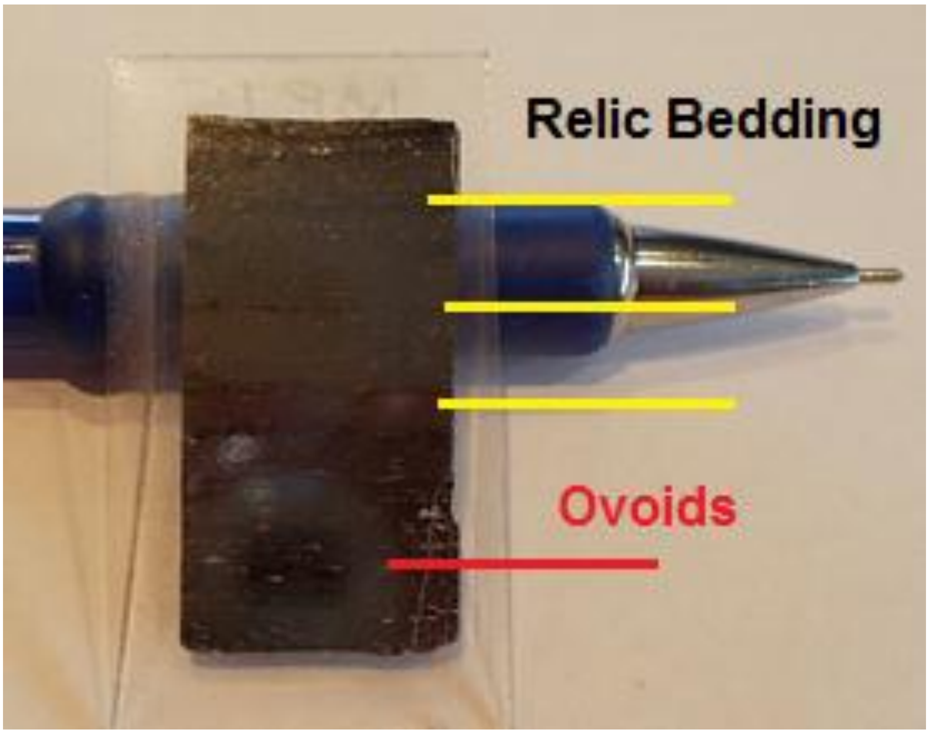

Figure 4-5 Photograph of the thin section of MP54_515: Relic bedding laminations can be seen as well as "concretionary ovoids" of calcite.

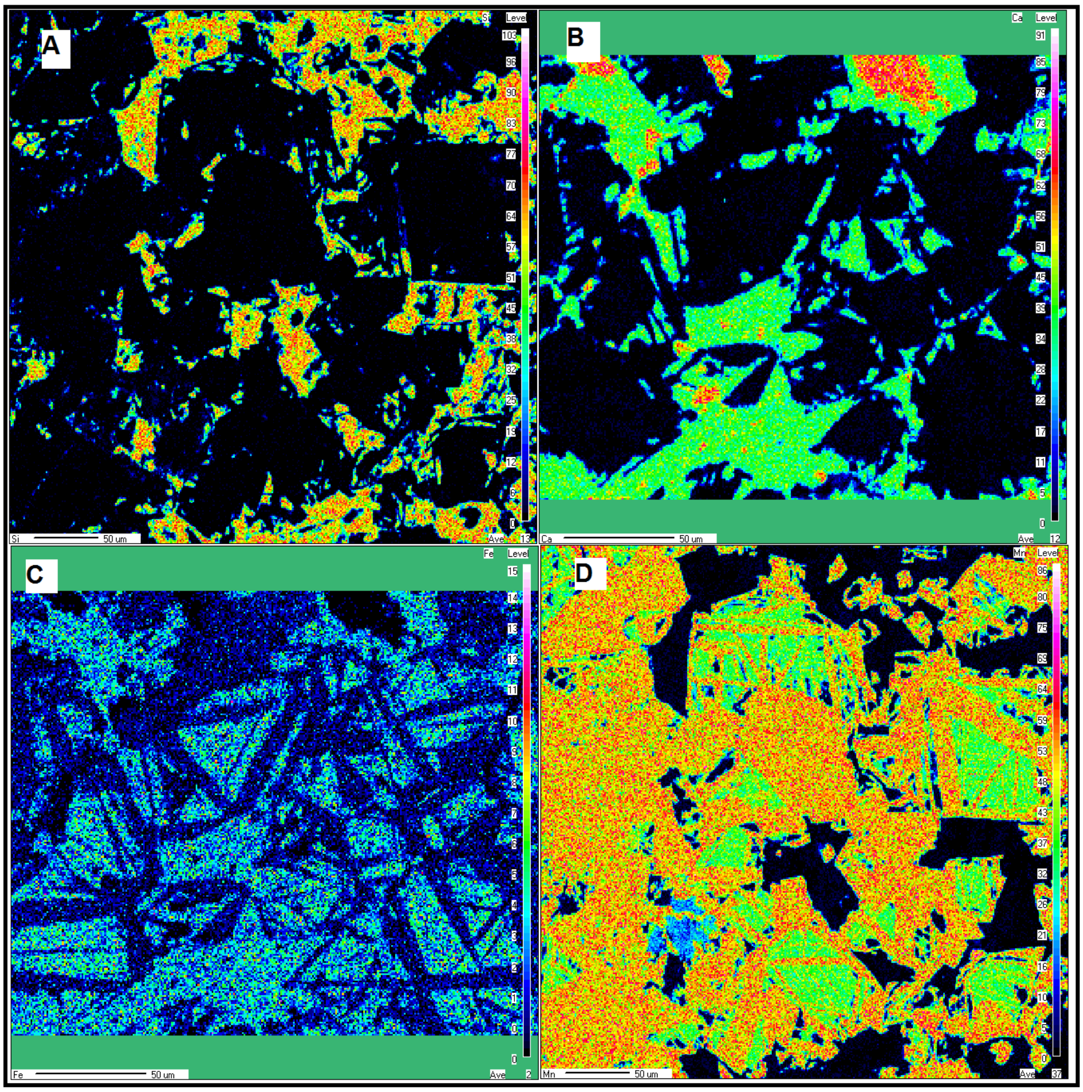

Figure 4-6 Elemental concentration maps of sample MP54_515 displaying A) Si is concentrating within the inter- granular spaces (as andradite). B) Ca is also concreting within the inter-granular spaces. C) Fe is concentrated in the centre of the hausmannite grains. D) Low manganese in the centre of the individual grains and high manganese in the laths of the high-grade Middelplaats ore. *Full size images are available in Appendix E.

Table 4-1 Representative mineral compositions of the Middelplaats high-grade ore sample MP54_515 in weight %.

Sample	Mineral	SiO_2	TiO_2	Al_2O_3	Cr_2O_3	FeO	MnO	MgO	CaO	Na_2O	Total	Total W/Fe_2O_3	Alm	And	Gross	Pyrope	Spess	Uvaro
P54_515	Andradite	36.09	0.02	0.35	0.03	24.84	2.90	0.17	33.99	0.00	98.34	100.96	0.00	97.86	0.00	0.81	1.22	0.11
MP54_515	Andradite	35.34	0.02	0.38	0.00	24.99	2.76	0.15	34.50	0.00	98.14	100.78	0.00	97.81	0.00	0.75	1.44	0.00
MP54_515	Andradite	35.91	0.01	0.48	0.02	23.78	2.75	0.15	34.41	0.03	97.51	100.02	0.00	97.02	0.00	0.74	2.15	0.09
MP54_515	Mineral Name	Na_2O	SiO_2	CaO	Cr_2O_3	MgO	Al_2O_3	FeO	K_2O	TiO_2	MnO	Total						
MP54_516	Brucite	0.00	3.42	0.17	0.00	81.59	0.89	0.65	0.46	0.00	0.00	87.18						
MP54_515	Calcite	0.01	0.00	58.39	0.04	0.00	0.01	0.18	0.20	0.00	0.00	58.82						
MP54_515	Calcite	0.00	0.00	57.70	0.01	0.02	0.01	0.19	0.57	0.00	0.00	58.51						
MP54_515	Mineral Name	SiO_2	CaO	Cr_2O_3	MgO	Al_2O_3	TiO_2	V_2O_3	MnO	Mn_2O_3	FeO	Fe_2O_3	Total					
MP54_515	Hausmannite	0.017	0.29	0	3.22	0.17	0.011	0.011	26	66.85		3.48	100.1					
MP54_515	Hausmannite	0.027	0.26	0	3.23	0.20	0	0	26	67.92		2.83	100.5					
MP54_515	Hausmannite	0.034	0.17	0	3.42	0.15	0	0	25.5	67.91		2.93	100.1					
MP54_515	Ferroan-Hausmannite	0.055	0.47	0.017	6.73	0.70	0	0.033	15.5	47.74	5	24.68	100.9					
MP54_515	Ferroan-Hausmannite	0.051	0.27	0	6.57	0.39	0	0.013	15	50.29	6	21.89	100.5					
MP54_515	Ferroan-Hausmannite	0.028	0.80	0.018	6.96	0.62	0.009	0	15	49.99	5	23.11	101.6					

4.1.2 Middelplaats low-grade ore sample MP54_567

Mineral composition of the low-grade ore is similar to the high-grade ore. Four minerals were positively identified by combined optical microscopy, microprobe and XRD analysis. Representative mineral compositions from microprobe analysis are given in Table 4-2 and XRD patterns in Figure 4-7. Minerals identified are:

- Calcite
- Hausmannite
- Braunite
- Andradite

Braunite is present as two species: braunite and braunite (new). XRD powder diffraction patterns of braunite (new) are not available; therefore, identification was limited to optical analysis and chemical composition determined by microprobe. Grain size of this sample is extremely small (< 50µm) on average with most grains coalescing into blebs or assemblages up to 200 µm in size (Figure 4-8 and Figure 4-9). Optical identification of the manganese minerals was complicated by the fine grain size within the blebs. The small mineral grains obscure the necessary identifying properties (i.e. anisotropic behaviour) due to their random crystallographic orientations. Bedding laminations are quite prominent (Figure 4-10), with alternating layers of pure calcite and hausmannite.

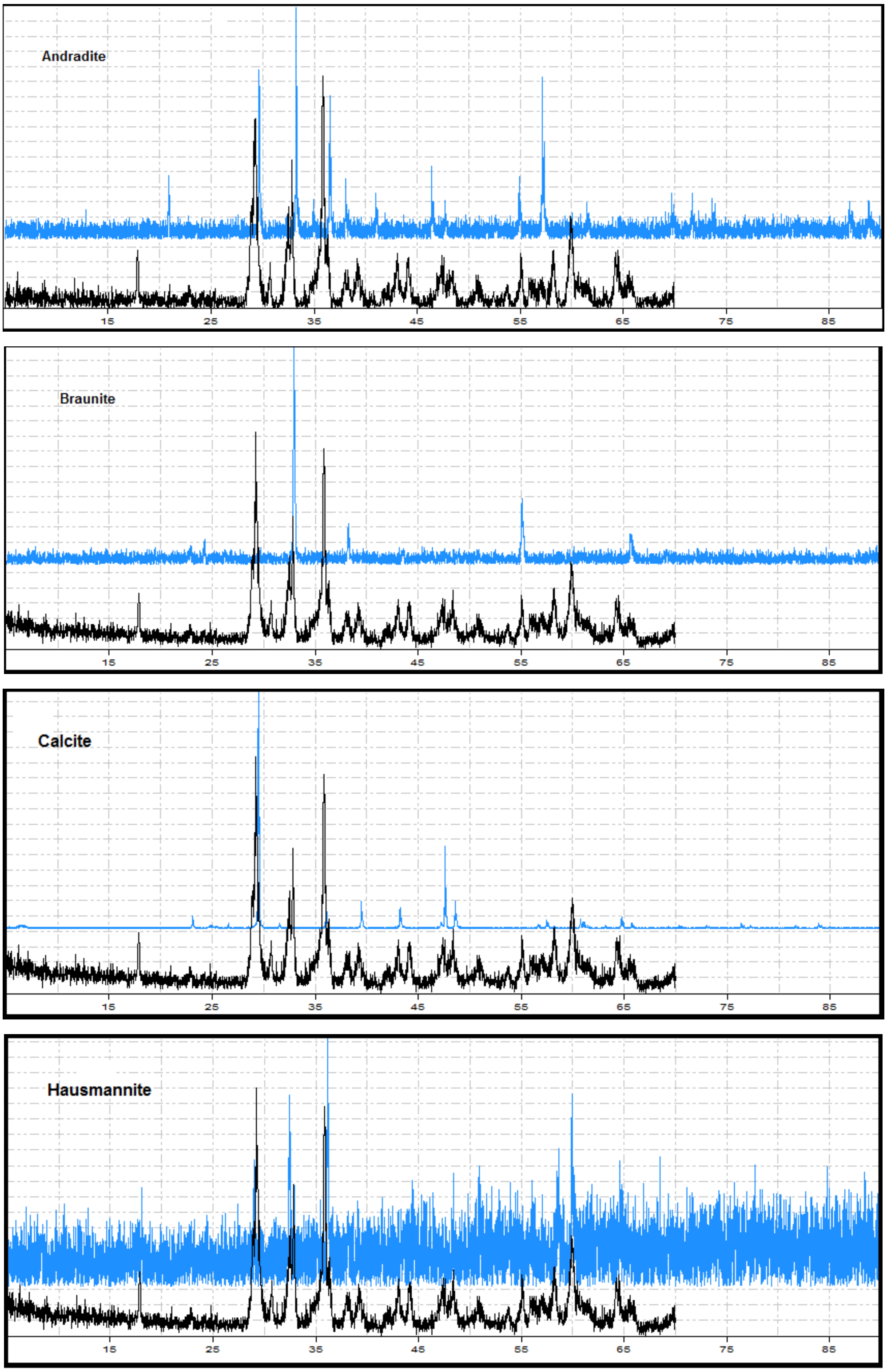

Figure 4-7 XRD mineral powder diffraction patterns from Middelplaats low-grade ore sample MP54_567. Patterns show the 4 identified minerals within the sample. Key = sample pattern in black and identified mineral in blue.

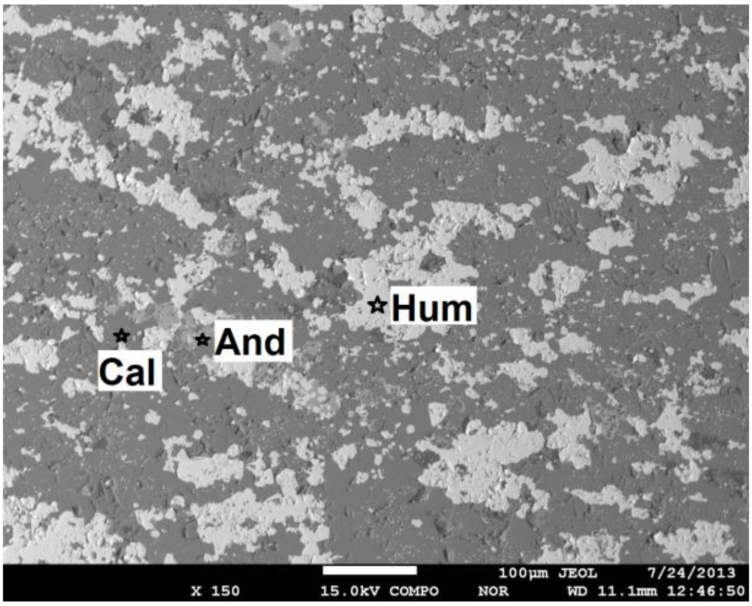

Figure 4-8 Microprobe image of MP54_567 showing the main mineral phases: Key- Cal=calcite; Hum=hausmannite; And=andradite.

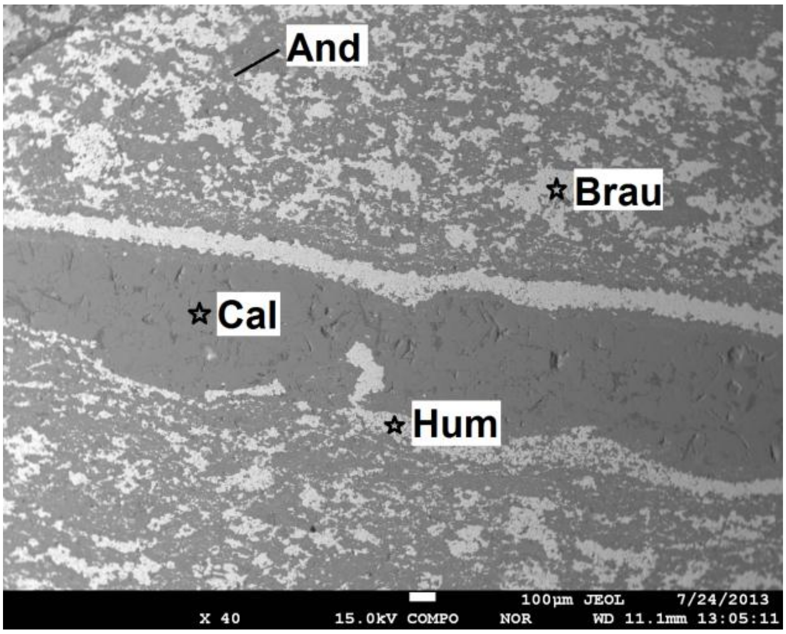

Figure 4-9 Microprobe image of MP54_567 showing main mineral phases as well as bedding laminations: Key- Cal=calcite; Hum=hausmannite; And=andradite; Brau=braunite.

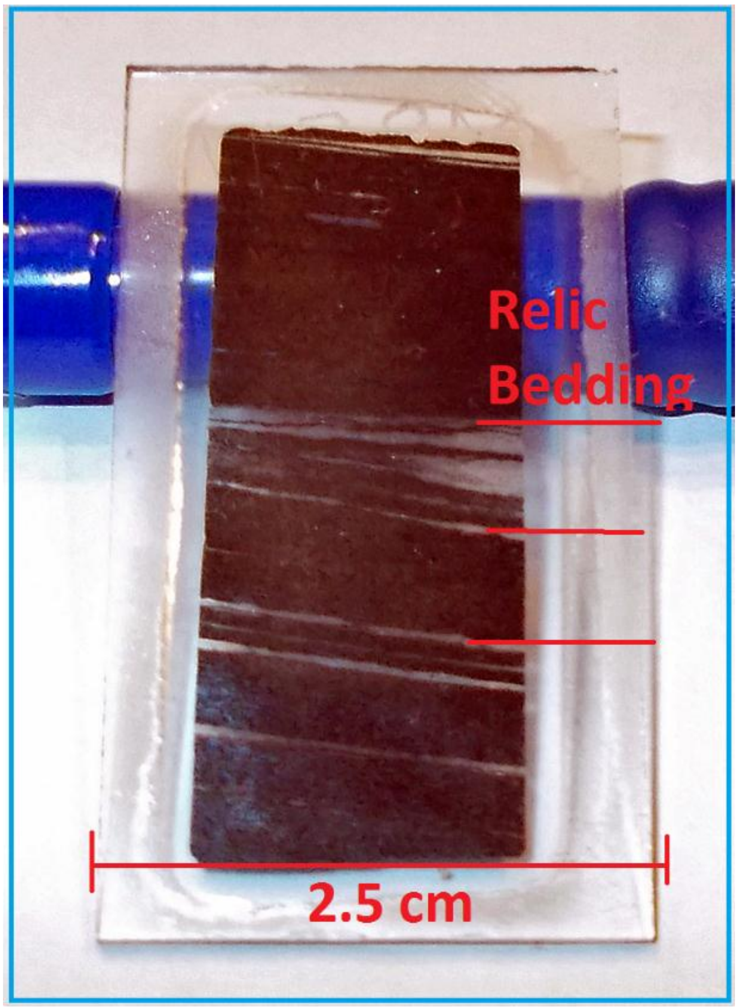

Figure 4-10 Photograph of the thin section of MP54_567 showing relic and/or primary bedding laminations.

Table 4-2 Representative mineral composition of Middelplaats low-grade ore sample MP54_567 in weight %.

MP54_567	Mineral Name	K_2O	CaO	SiO_2	Al_2O_3	MgO	FeO	MnO	BaO	SrO	**Total**		
MP54_567	Calcite	0.00	57.53	0.00		0.39	0.01	0.45	0.05	0.04	**58.47**		
MP54_567	Calcite	0.03	55.82	0.00		0.58	0.00	0.41	0.01	0.00	**56.84**		
MP54_567	Calcite	0.03	55.69	0.00		0.25	0.17	0.95	0.01	0.00	**57.10**		
MP54_567	Mineral name	SiO_2	CaO	Cr_2O_3	MgO	Al_2O_3	TiO_2	V_2O_3	MnO	Mn_2O_3	FeO	Fe_2O_3	**Total**
MP54_567	Hausmannite	0.01	0.45	0.00	2.89	0.32	0.00	0.03	25.00	67.55	1.00	2.93	**100.18**
MP54_567	Hausmannite	0.07	0.31	0.05	2.88	0.36	0.00	0.00	26.00	65.39		4.32	**99.37**
MP54_567	Braunite	6.00	1.64	0.02	1.73	0.58	0.03	0.02	25.00	59.98		4.30	**99.29**
MP54_567	Braunite	7.36	0.16	0.00	13.27	0.71	0.02	0.00	13.00	67.59	1.00	1.20	**104.31**
MP54_567	Braunite (new)	1.92	0.62	0.03	6.28	0.88	0.04	0.00	15.00	50.25	5.00	19.16	**99.19**

4.1.3 Middelplaats igneous rock sample MP54_S2

4.1.3.1 Classification of Middelplaats igneous sample MP54_S2

In order to classify the igneous rocks at the Middelplaats mine, the hand sample and thin section of sample MP54_S2 were examined to determine the modal mineralogy. The hand sample is phaneritic, mesocratic, medium grey/green with white to pink blebs in colour and inequigranular. Grain size is medium 1- 3mm. Visible minerals are plagioclase feldspar, quartz, pyroxene and amphibole. Microscopic examination of the thin section using both transmitted and reflected was used to identify additional mineral phases not easily seen in the hand sample and estimate the percentage of mineral composition. For the purpose of rock classification, any altered minerals were accounted for as the original protolith (i.e. epidote form a plagioclase is counted as a plagioclase).

From microscopic examination the average composition of sample MP54_S2 is:

Plagioclase feldspar	48%
Clinopyroxene	30%
Quartz	10%
Alkali feldspar	5%
Magnetite	2%
Ilmenite	2%
Rutile	1%
Amphibole	1%
Chlorite	1%
Total	100%

The International Union of Geological Sciences (IGUS) recommends using the quartz, alkali feldspar, plagioclase feldspar and feldspathoid (QAPF) diagram for phaneritic plutonic rocks with a grain size of 3mm or larger (Le Maitre, et al., 1989). Quartz, alkali feldspar and plagioclase feldspar were normalized to 100% then plotted on the QAPF diagram (Figure 4-11). The sample plotted in the quartz diorite gabbro field which according to the Le Maitre, et al., (1989) “Either of the two synonymous terms **dolerite** or **diabase** may be used for medium-grained gabbros rather than the term microgabbro”. Therefore, on the above basis this sample will now be classified as a dolorite. Also as the igneous material from both drill holes is essientially homogeneous and phaneritic, this same classifaction will be used for all Middelplaats igneous samples. Additional lines of evidence as to the nature of the contact with the overlying sediments will also be presented to support this classifaction.

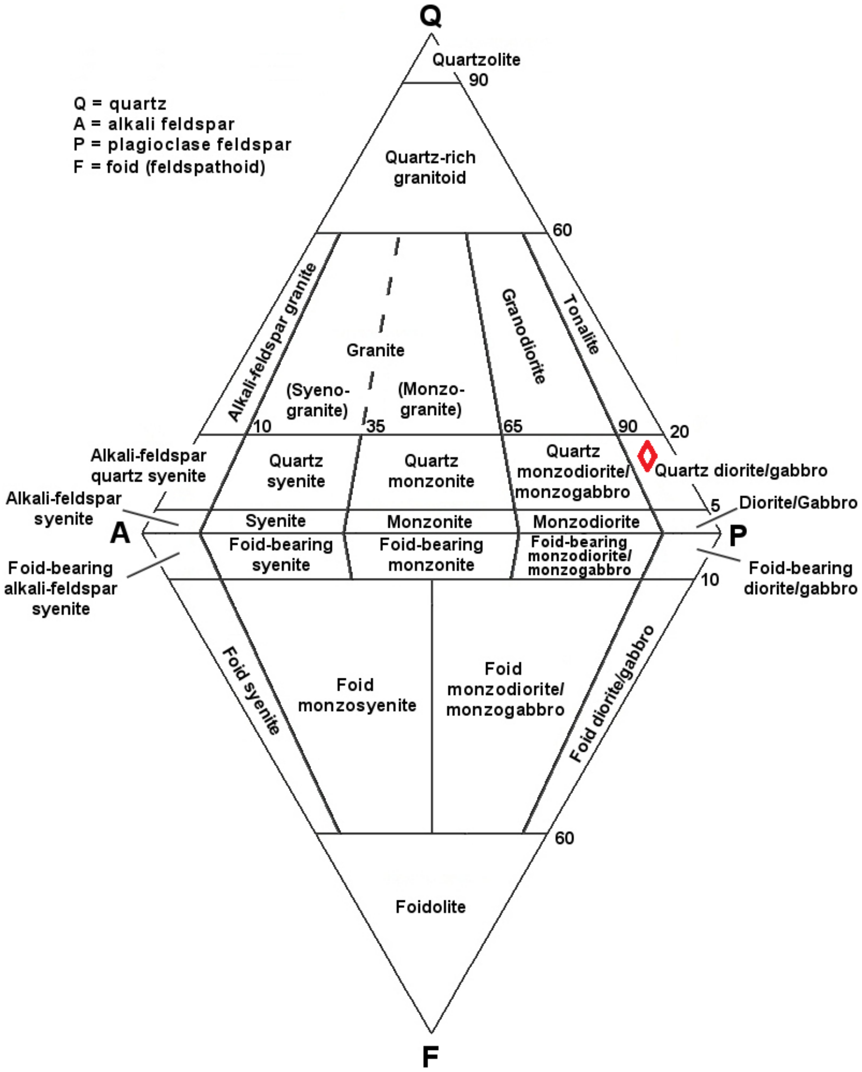

Figure 4-11 QAPF diagram for Middelplaats igneous sample MP_54S2 (Le Maitre, et al., 2002).

4.1.3.2 Petrogrophy of Middelplaats igneous sammple MP54_S2

Microscopic examination of this rock shows a moderate level of hydrothermal alteration. Primary igneous textures are well preserved with no grain boundary dissolution, preferential alignment off minerals or pervasive veining, indicative of compressional metamorphism. As noted above the rock is dominantly composed of feldspar and clinopyroxene with accessory amounts of amphibole, magnetite, ilmenite and chlorite (Figure 4-12). Most of the feldspars appear to be plagioclase that has been altered to a potassium bearing feldspar (here after referred to as K-fds or K-feldspar as the alteration produces anomalous K rich mineral compositions). However, alteration to epidote, chlorite, calcite and myrmekite was also seen. The clinopyroxenes also show some alteration to amphibole, chlorite, epidote and calcite. The most common replacement texture observed is pseudomorphic with the original mineral habit being retained. Several of the feldspars also appeared to show exsolution lamellae or an antiperthitic texture (Figure 4-12 D). This incipient alteration is also easily visible in the microprobe images as subtle changes in the shade of grey. These colour differences are the result of slight chemical compositional changes within the mineral phases (Figure 4-13) Mineral compositional plots (Figure 4-14) show the clinopyroxenes are mostly augite and the feldspars are alkaline ranging from Ab 30 to Or 60. Representative mineral compositions from the microprobe are presented in Table 4-3.

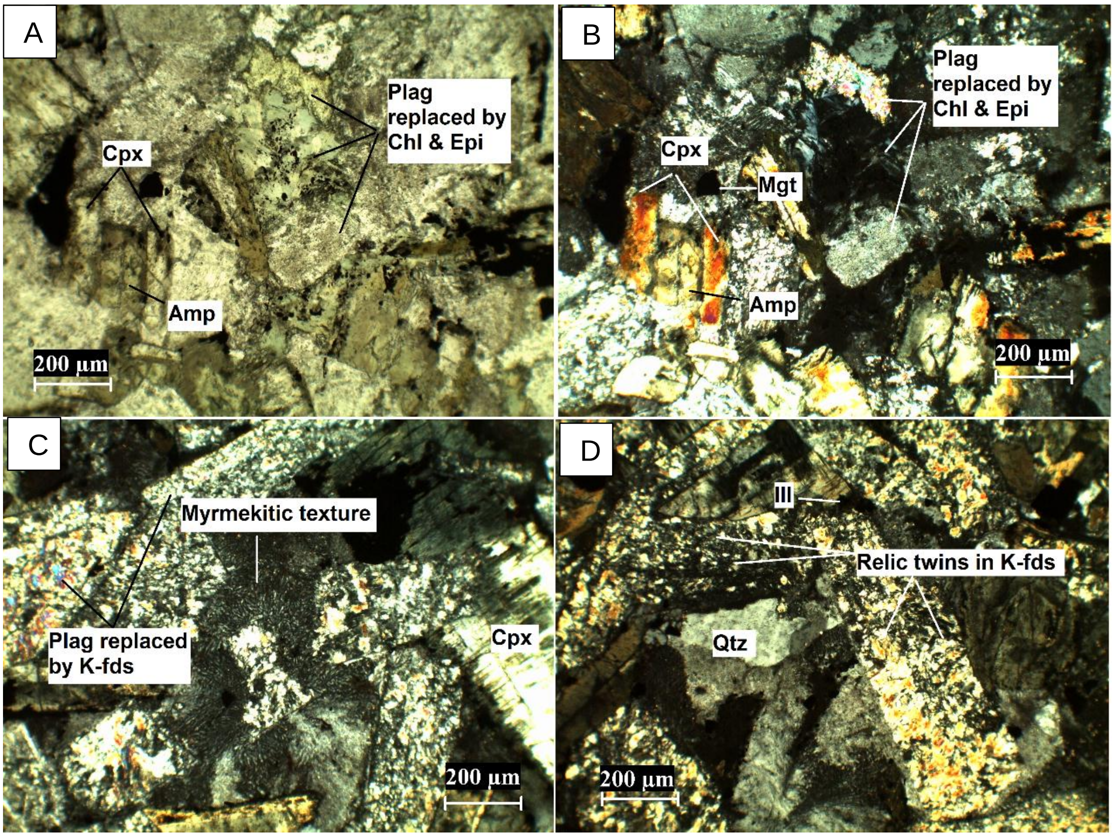

Figure 4-12 Optical mineralogy of MP54_S2 A) Plagioclase altered to chlorite and epidote; B) Same as A shown in XPL; C) Myrmekitic textures and plagioclase replaced by K-feldspar; D) Relic twinning common in plagioclase replaced by K-feldspar. Key: Amp= Amphibole; Cpx= clinopyroxene; Epi= epidote; Ill=Ilmenite, Plag=plagioclase; Qtz= Quartz.

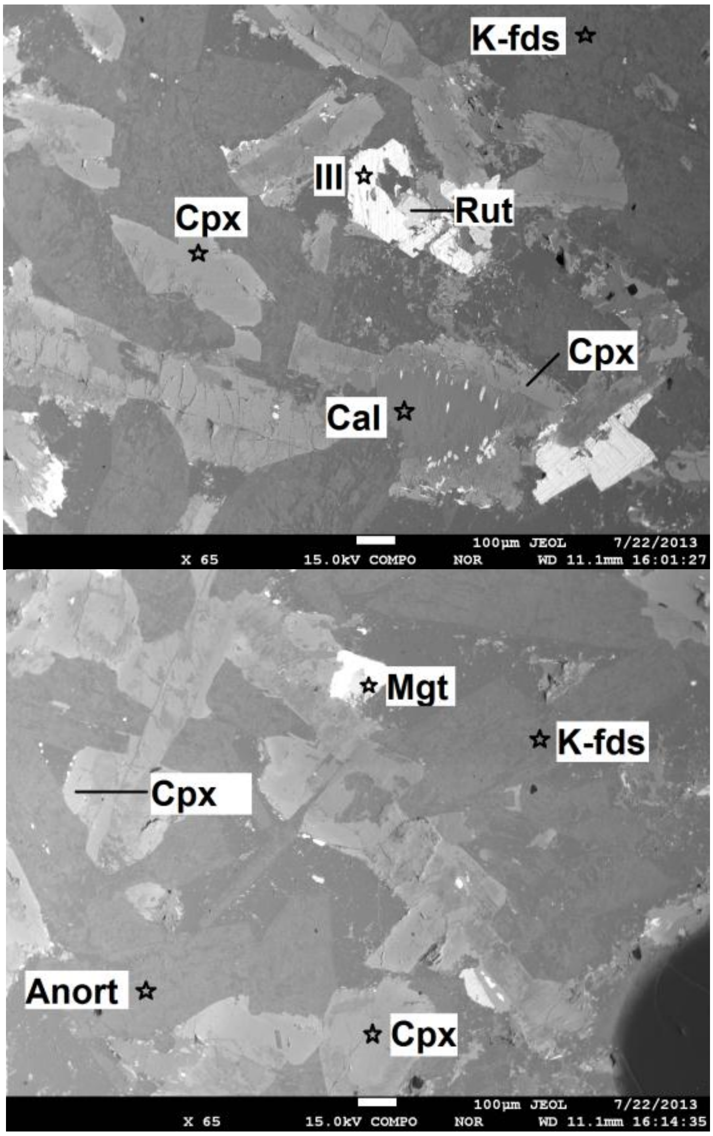

Figure 4-13 Microprob images of typical minerals in assemblages in Middelplaats igneous sample MP54_S3. Key: K-fds= K-feldspar; Cpx= Clinopyroxene; Rut=Rutile; Cal=Calcite; And= Andradite; Mgt=Magnetite; Anort=Anorthite; Ill=Ilmenite

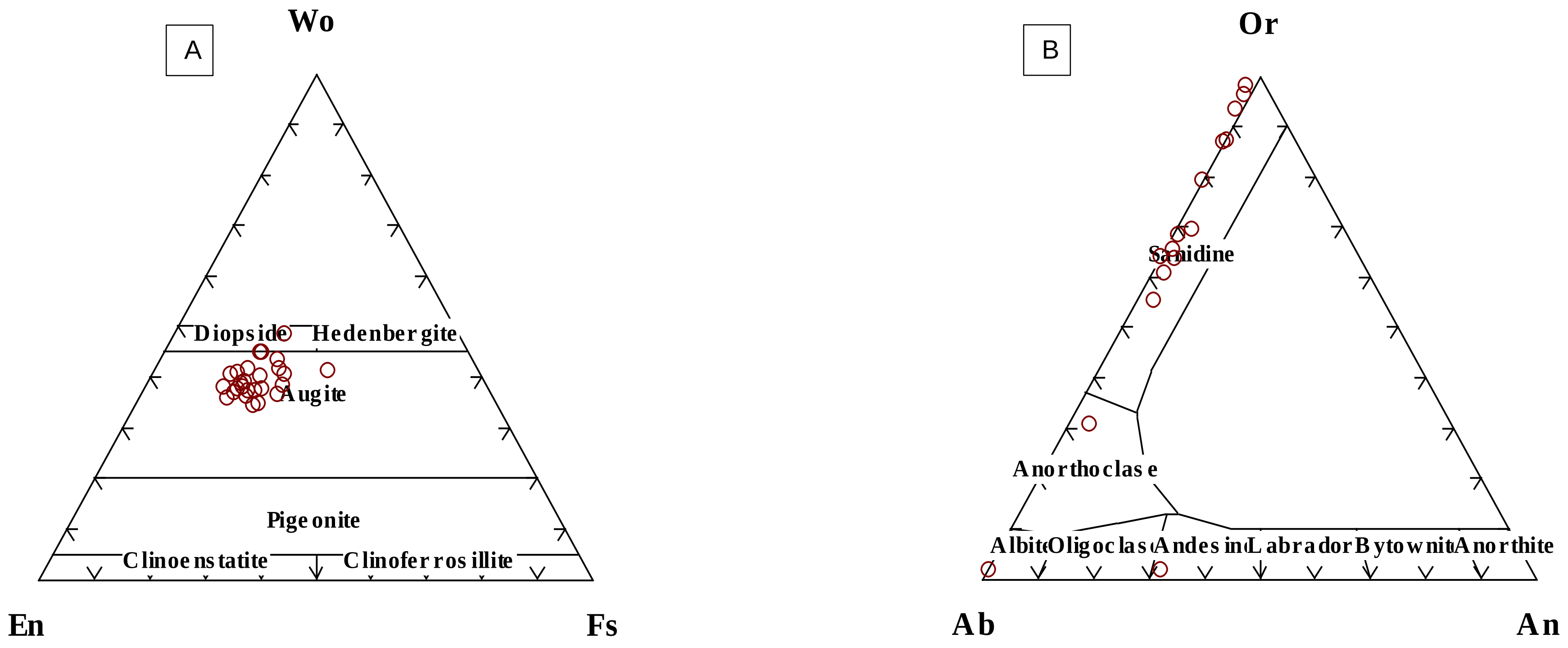

Figure 4-14 A) Ternary end member diagram for pyroxenes (Morimoto, 1988), and B) Feldspar end member diagram (Deer, et al., 1992) for dolerite MP54_S2.

Table 4-3 Representative mineral composition of sample MP54_S2

Sample Name	Mineral Name	Na_2O	SiO_2	CaO	Cr_2O_3	MgO	Al_2O_3	FeO	K_2O	TiO_2	MnO	Total			
MP54_S2	Epidote	0.30	38.78	5.22	0.05	17.59	10.58	18.76	0.03	0.02	0.43	**91.76**			
MP54_S2	Garnet	0.01	37.74	23.19	0.03	0.02	22.33	13.68	0.00	0.00	0.35	**97.34**			
MP54_S2	Amphibole	1.14	52.92	22.99	0.04	10.71	0.45	11.84	0.01	0.05	1.10	**101.24**			
Sample Name	Mineral	SiO_2	TiO_2	Al_2O_3	FeO	Cr_2O_3	MnO	MgO	CaO	Na_2O	K_2O	**Total**	WO	EN	FS
MP54_S2	Augite	53.2	0.21	1.374	11.04	0.07	0.323	17.16	17.2	0.17	0.01	**100.8**	34	47.7	17.2
MP54_S2	Augite	52.4	0.26	1.711	11.32	0.094	0.42	16.22	17.6	0.2	0.01	**100.3**	35.1	45.7	17.9
MP54_S2	Diopside	51.7	0.11	0.639	12.3	0.125	0.523	10.11	21.6	0.95	0.01	**98.05**	45.9	29.9	20.4
Sample Name	Mineral	SiO_2	TiO_2	Al_2O_3	FeO	MnO	MgO	CaO	Na_2O	K_2O		**Total**	Ab	An	Or
MP54_S2	K-Feldspar	58.77	0.01	31.59	1.29	0.01	0.60	0.54	2.17	6.29		**101.25**	32.90	4.50	62.70
MP54_S2	Andesine	68.33	0.01	19.89	2.47	0.06	0.00	4.92	5.48	0.08		**101.25**	66.40	32.90	0.70
MP54_S2	K-Feldspar	58.91	0.02	30.19	1.73	0.08	1.05	0.57	1.77	6.84		**101.15**	26.90	4.80	68.30
MP54_S2	Anorthoclase	67.20	0.02	24.42	0.73	0.02	0.36	0.67	4.27	2.99		**100.67**	64.70	5.60	29.70
MP54_S2	K-Feldspar	60.05	0.01	29.21	2.48	0.03	0.93	0.32	1.95	6.62		**101.60**	30.10	2.70	67.20
MP54_S2	Albite	59.52	0.00	20.49	5.27	0.14	6.08	0.21	6.22	0.07		**97.98**	97.50	1.80	0.80
Sample Name	Mineral Name	Na_2O	SiO_2	CaO	Cr_2O_3	MgO	Al_2O_3	Fe_2O_3	K_2O	TiO_2	MnO	**Total**			
MP54_S2	Magnetite	0.02	2.18	1.90	0.05	0.00	0.23	78.07	0.00	16.62	0.03	**99.10**			
MP54_S2	Ilmenite	0.04	0.33	0.31	0.04	0.02	0.53	38.34	0.03	55.68	0.61	**95.93**			
MP54_S2	Magnetite	0.00	0.12	0.18	0.01	0.00	0.28	83.71	0.00	13.77	0.04	**98.11**			
MP54_S2	Ilmenite	0.00	0.12	0.03	0.00	0.02	0.00	50.45	0.01	47.73	0.41	**98.77**			

4.1.4 Middelplaats igneous rock sample MP54_CS3; contact between the igneous rock and the manganese ore

Sample MP54_CS3 was selected on the basis of its position directly on the contact between the manganese ore and the dolerite (Figure 4-15). As such, the chemical composition is diverse. Representative mineral compositions taken from the microprobe are shown in Table 4-4 and Table 4-5.

Figures 4-15 to 4-18 depict the complex chemical changes occurring along the contact between the manganese ore and the dolerite. Within the doleritic material, magnetite (Fe_3O_4) is the only oxide mineral present. After (or at) the contact with the manganese ore, the oxide phase changes to Bixbyite (Mn^3+, $Fe^3+)_2$ O_3. Garnets, which in the lesser-altered dolerite samples located away from the ore (samples MP54_S1, S2 and MP53_S1, S2) are dominantly grossular, show a gradual change approaching the interaction area to andradite. Within the ore zone (Samples MP54_567 and MP54_515), andradite becomes the only garnet phase (Table 4-1and Table 4-2). Andradite can also be seen as a replacement phase encapsulating the magnetite and occurring interstitially to the CPX (Figure 4-16). Feldspar composition varies slightly across the contact but is generally in the plagioclase range (~ An 30 to Ab 99; Figure 4-19B and Table 4-5).

Minerals located within the contact zone are subhedral and irregular. Optically the minerals appear blackened and burnt (glassy). Optical recognition of non-opaque minerals is impossible as transmitted light (both plane polarized and crossed poles) show all minerals as black. Andradite is seen to be replacing grossular until it is the only remaining amphibole phase. Microprobe examination shows evidence of secondary mineral growth with (e.g. andradite's noted above, not easily visible optically due to the effects of the contact metamorphism) some euhedral replacement minerals and grain boundaries exhibiting classical 60/120 metamorphic re-equilibration. Also, from examination of the contact zone (Figure 4-15), it is important to note there is no evidence of a primary sedimentary contact in which the manganese ore was deposited onto a pre-existing flow. There is also no evidence of erosion or unconformity that one would expect if this contact were sedimentary in nature (this supports the use of the plutonic rock classification above).

Elemental maps of the contact zone between the Mn ore and dolerite show a coalescence of magnesium along the contact and a slight but definite increase in aluminium content (on the dolerite side) whilst Si is accumulating on the Mn ore side as andradite (Figure 4-18).

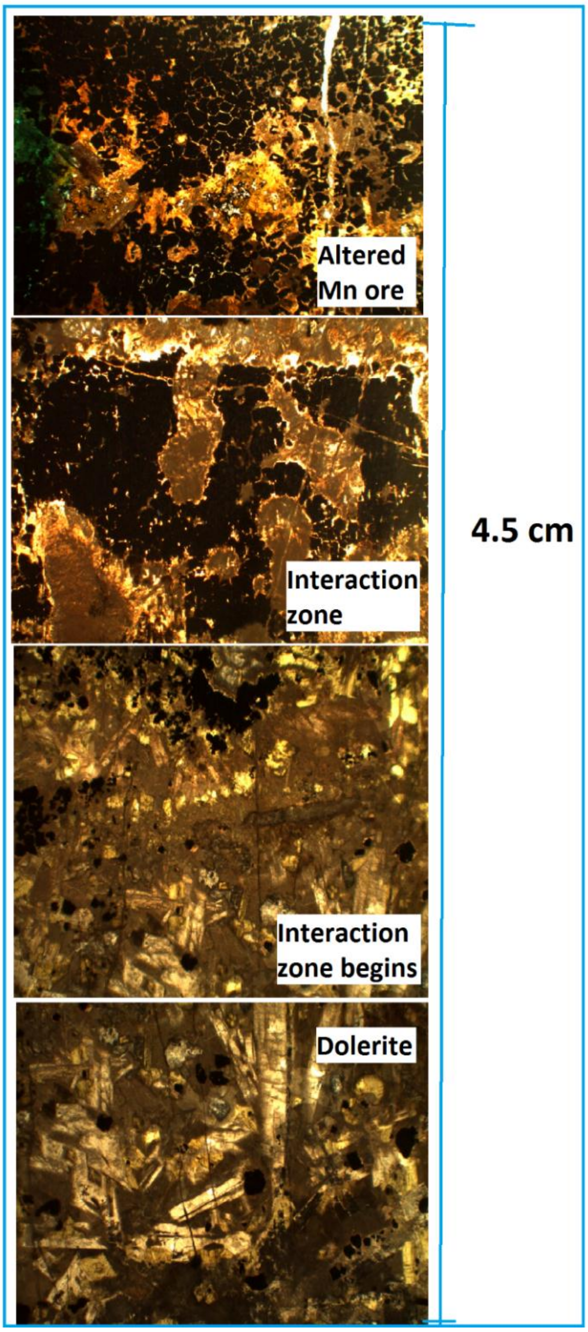

Figure 4-15 Composite photo of the thin section of sample MP54_CS3 contact between the dolerite and manganese ore. Photo shows the "normal dolerite" at the bottom grading into the contact with the Mn ore and glassy metamorphosed altered Mn ore at the top.

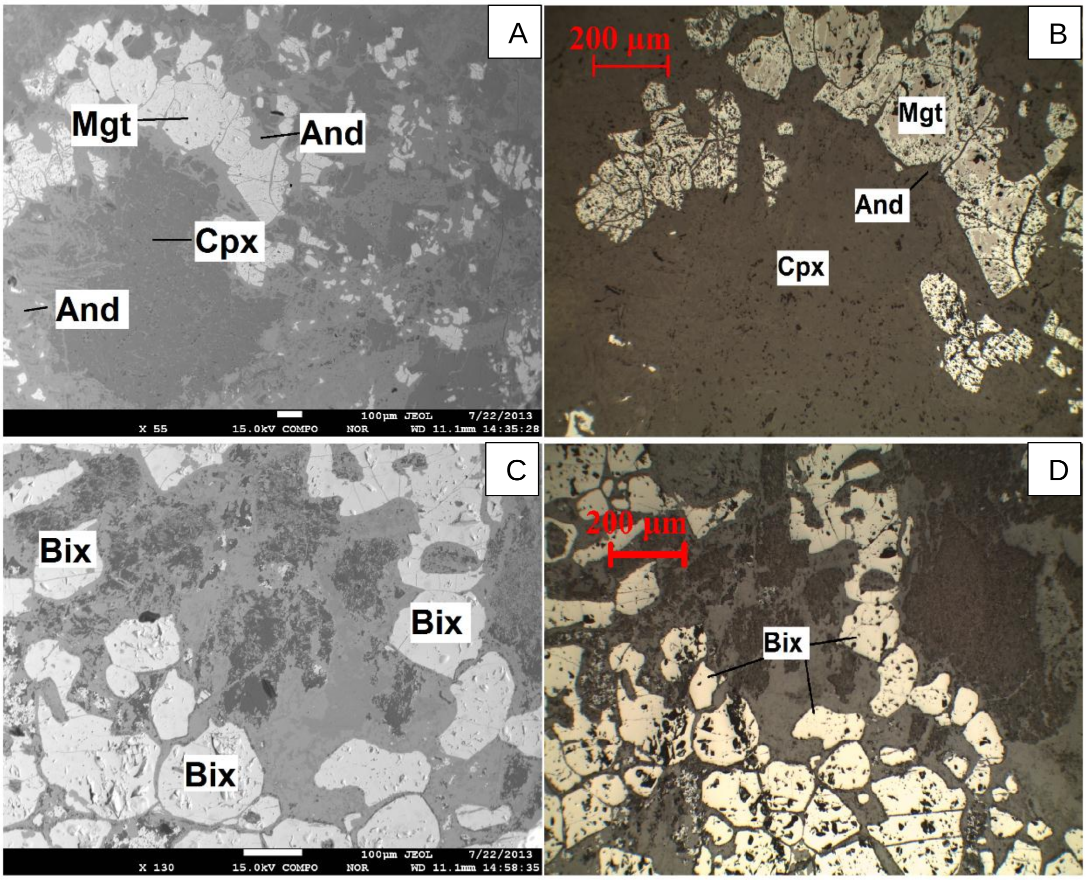

Figure 4-16 Photomicrographs (B & D) and backscatter microprobe images (A & C) of the contact between the dolerite and manganese ore sample MP54_CS3. Images A & B correspond as do C & D. The location on the thin section is shown on Figure 4-15 above as “interaction zone”. Key: Bix= bixbyite; Cpx=clinopyroxene; And=andradite; Mag=magnetite.

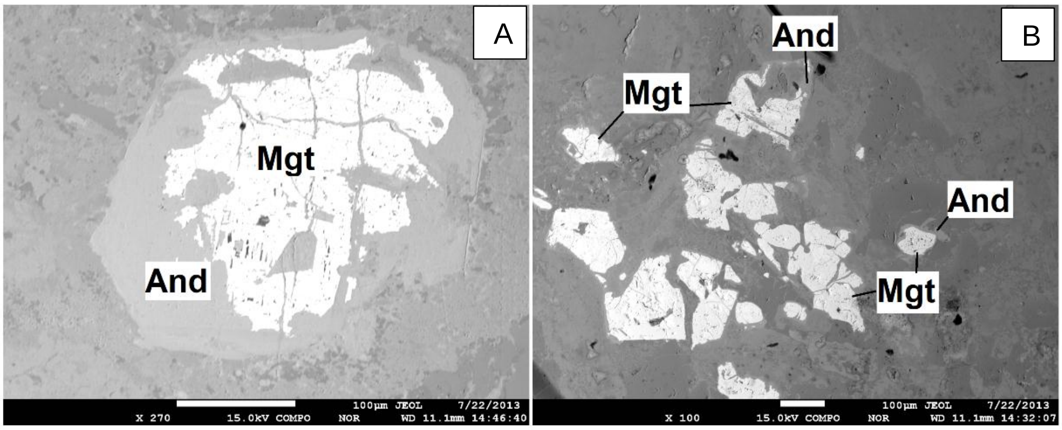

Figure 4-17 Backscatter microprobe images of sample MP54_CS3 showing A) Euhedral andradite replacing magnetite; B) Andradite surrounding magnetite. Key as above.

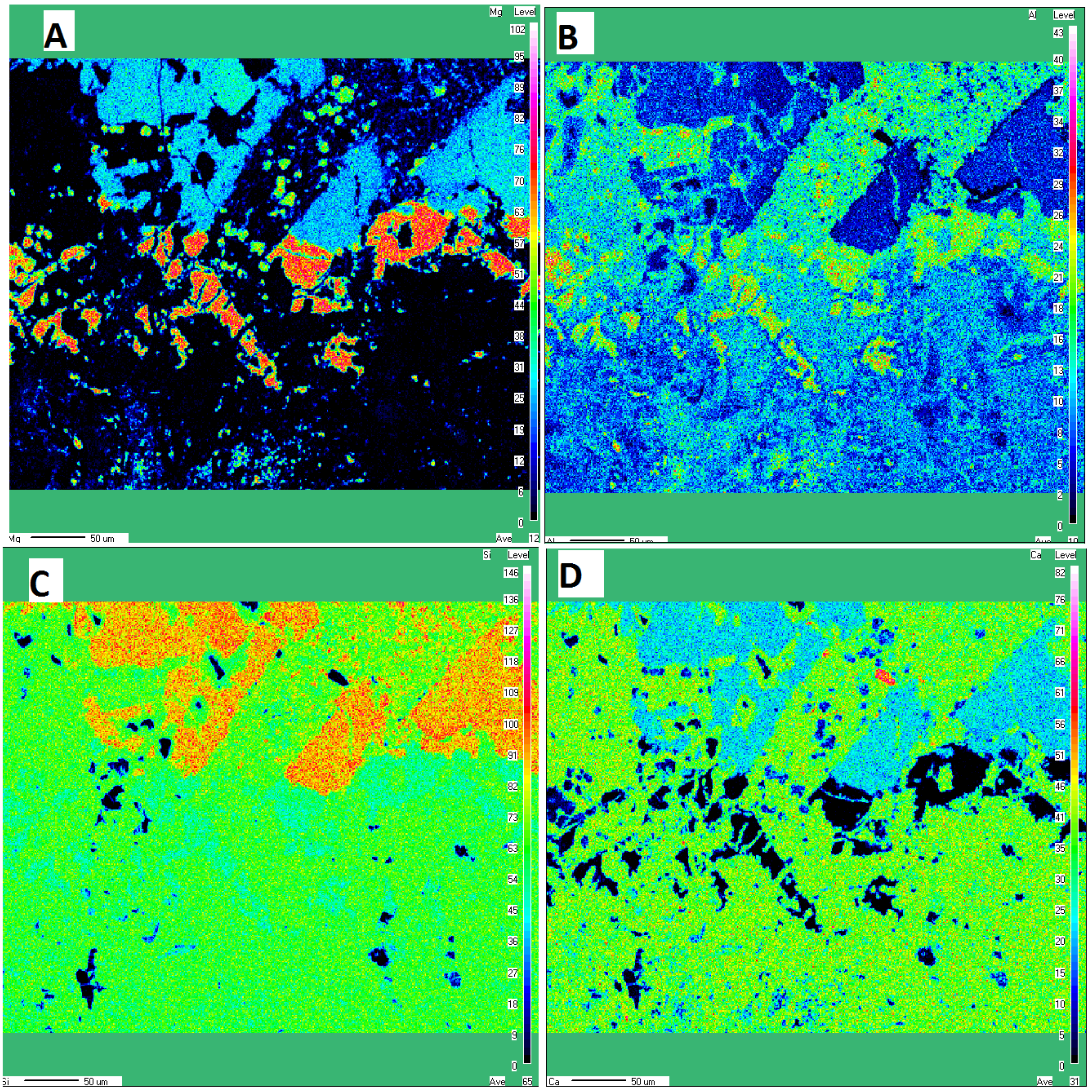

Figure 4-18 Elemental composition maps of the interaction zone between the Mn ore and the dolerite MP54_CS3. Elements shown are -- A) Mg; B) Al; C) Si; D.

Table 4-4 Representative mineral compositions of sample MP54_CS3 (continued on next page).

Sample Name	Mineral Name	SiO_2	CaO	Cr_2O_3	MgO	Al_2O_3	TiO_2	V_2O_3	MnO	Mn_2O_3	FeO	Fe_2O_3	NiO	**Total**
MP54_S3C	Bixbyite	0.07	0.18	0.03	3.45	2.33	1.66	0.00	24.50	18.79	1.00	48.07	0.02	**100.10**
MP54_S3C	Bixbyite	0.13	0.12	0.00	4.14	3.06	1.41	0.00	24.00	19.72	1.00	46.26	0.06	**99.90**
MP54_S3C	Ilmenite	0.21	0.46	0.00	1.36	0.07	45.93	0.00	15.00	9.34	19.45	6.17	0.19	**98.73**
MP54_S3C	Magnetite	0.04	0.00	0.03	7.22	2.29	1.36	0.00	6.00	0.49	13.50	67.66	0.30	**98.89**
MP54_S3C	Magnetite	0.05	0.00	0.09	7.59	0.84	0.95	0.00	5.00	0.19	13.75	69.56	0.34	**98.36**
MP54_S3C	Mineral	SiO_2	TiO_2	Al_2O_3	FeO	Cr_2O_3	MnO	MgO	CaO	Na_2O	K_2O	**Total**		
MP54_S3C	Amphibole	51.25	0.00	3.58	6.19	0.03	0.41	17.43	18.15	0.44	1.21	98.68		
MP54_S3C	Amphibole	50.48	0.00	3.30	6.06	0.06	0.43	16.45	19.84	0.42	1.10	98.08		
MP54_S3C	Mineral Name	Na2O	SiO2	CaO	Cr2O3	MgO	Al2O3	FeO	K2O	TiO2	MnO	**Total**		
MP54_S3C	Calcite	0.00	0.00	58.84	0.00	0.17	0.02	0.10	0.01	0.00	7.45	**66.59**		
MP54_S3C	Calcite	0.00	0.00	62.30	0.00	0.03	0.00	0.07	0.01	0.01	4.33	**66.75**		
MP54_S3C	Mineral	SiO_2	TiO_2	Al_2O_3	Cr_2O_3	FeO	MnO	MgO	CaO	Na_2O	K_2O	**Total**		
MP54_S3C	Talc-Chlorite	38.44	0.02	6.38	0.00	1.75	1.13	37.63	0.18	0.02	0.03	**85.58**		
MP54_S3C	Penninite	33.72	0.00	14.34	0.05	1.12	0.48	34.86	0.10	0.03	0.01	**84.70**		

Table 4-5 Representative mineral compositions of sample MP54_CS3.

MP54_S3C	Mineral Name	SiO_2	TiO_2	Al_2O_3	Cr2O3	FeO	MnO	MgO	CaO	Na_2O	**Total**	Alm	And	Gross	Pyrope	Spess	Uvaro
MP54_S3C	Garnet	42.72	0.13	8.40	0.02	12.55	0.38	5.17	31.64	0.90	**101.89**	0.00	50.13	22.86	25.84	1.08	0.09
MP54_S3C	Garnet	38.63	0.07	22.07	0.01	1.19	0.45	0.08	37.88	0.00	**100.37**	1.95	1.90	94.86	0.31	0.97	0.02
MP54_S3C	Garnet	37.73	0.00	22.29	0.00	1.27	0.25	0.03	38.68	0.00	**100.25**	0.00	2.11	97.19	0.13	0.56	0.00
MP54_S3C	Garnet	38.33	0.09	18.38	0.00	4.93	1.19	0.11	37.09	0.02	**100.13**	0.00	8.69	88.03	0.45	2.83	0.00
MP54_S3C	Garnet	36.11	0.39	10.57	0.00	11.84	3.65	4.09	33.26	0.00	**99.90**	0.00	28.43	36.36	23.38	11.83	0.00
MP54_S3C	Mineral	SiO_2	TiO_2	Al_2O_3	FeO	Cr_2O_3	MnO	MgO	CaO	Na_2O	K_2O	**Total**	WO	EN	FS	WEF	
MP54_S3C	Diopside	52.74	0.05	1.27	1.39	0.00	4.45	14.54	25.76	0.15	0.01	**100.36**	50.91	39.99	9.10	98.95	
MP54_S3C	Augite	49.32	0.21	4.11	3.90	0.00	12.72	13.81	15.73	0.43	0.01	**100.23**	32.74	40.00	27.26	96.89	
MP54_S3C	Augite	48.77	0.34	5.12	7.90	0.06	0.63	15.79	21.09	0.32	0.01	**100.03**	42.41	44.19	13.40	97.71	
MP54_S3C	Clinoenstatite	53.67	0.16	3.02	10.18	0.00	1.10	29.83	2.04	0.01	0.01	**100.01**	3.89	79.28	16.83	99.96	
MP54_S3C	Mineral	SiO_2	TiO_2	Al_2O_3	FeO	MnO	MgO	CaO	Na_2O	K_2O	**Total**	Ab	An	Or			
MP54_S3C	Anorthite	40.31	0.23	18.47	1.64	0.41	2.14	36.02	0.04	0.00	**99.25**	0.20	99.80	0.00			
MP54_S3C	Labradorite	56.46	0.02	2.33	0.31	0.68	0.00	30.19	8.44	0.18	**98.61**	33.40	66.10	0.50			
MP54_S3C	Andesine	64.56	0.03	12.17	0.02	0.09	0.05	13.73	7.89	0.05	**98.57**	50.90	48.90	0.20			
MP54_S3C	Anorthoclase	64.79	0.02	23.46	0.08	0.02	0.46	0.41	5.76	2.07	**97.07**	78.40	3.10	18.50			

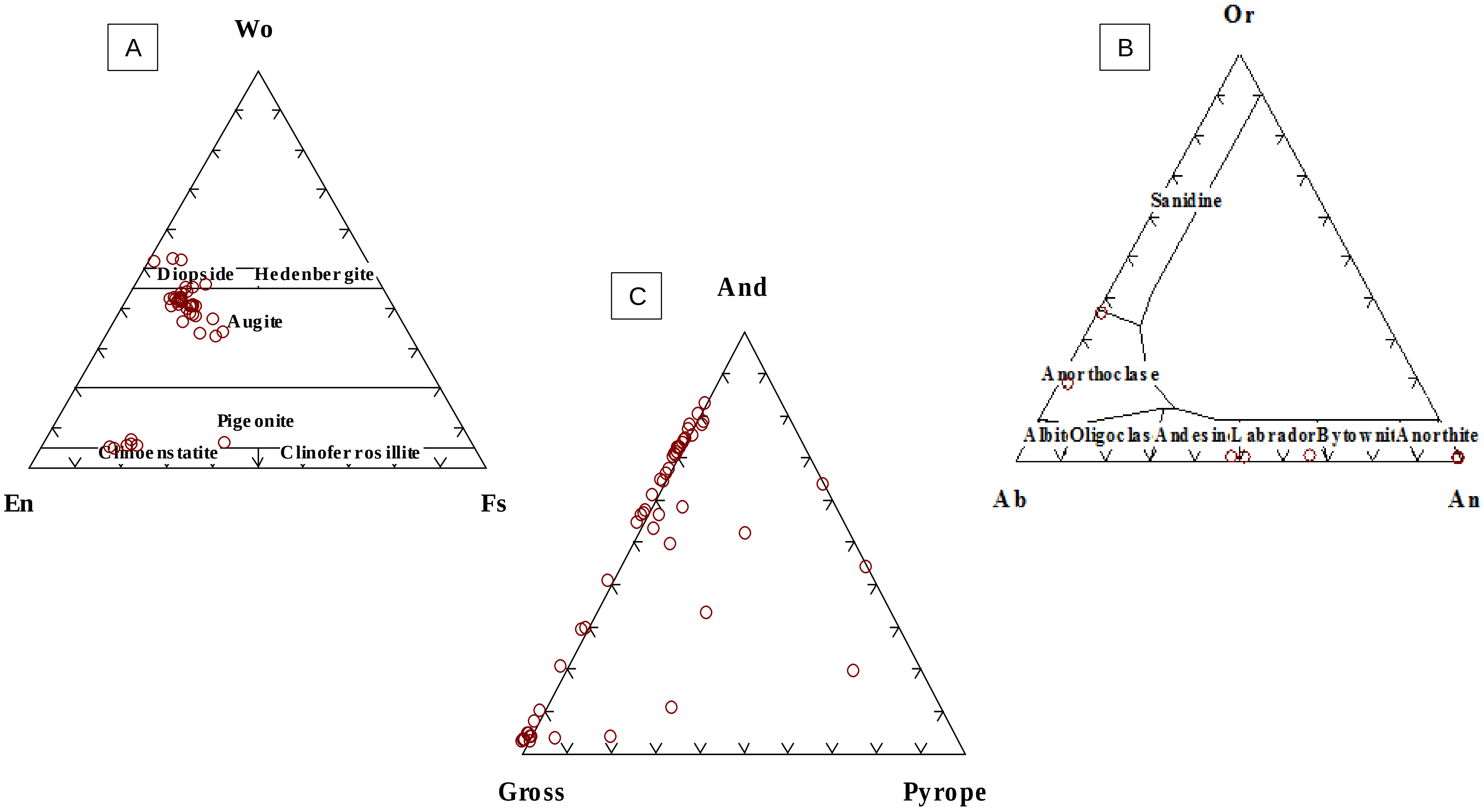

Figure 4-19 Ternary diagrams showing mineral classifications for sample MP54_CS3, A) Ternary end member diagram for pyroxenes (Morimoto, 1988); B) Feldspars by end members (Deer, et al., 1992); C) Garnets by end members. End member calculations from Deer, et al., (1992).

4.1.5 Middelplaats igneous rock sample MP53_BIF; igneous material with BIF xenolith

Sample MP53_BIF (Figure 4-20) was taken from a stratigraphically similar location to MP54_CS3 from the adjacent MP53 drill hole where the Mn ore is directly in contact with the igneous rock. The sample consists of a BIF xenolith intercalated with dolerite. The sample is highly altered with most grains subhedral to anhedral and many showing grain boundary dissolution and replacement rims (Figure 4-21 A-F). Grain size ranges from 25 µm to 200 µm. Feldspars similarly to MP54_S2 appear optically to be plagioclase that has undergone alteration to k-feldspar and/or chlorite, epidote and calcite. Representative mineral compositions from microprobe analysis are shown in Table 4-6 and mineral classification diagrams as (Figure 4-22). Similar to MP54_CS3 the range of garnets is dominantly grossular and andradite and the major species of amphibole actinolite and silicic edenite, with augite the major pyroxene. It should be noted that due to the extremely high level of alteration microprobe analyses, even after stoichiometric re-balancing, failed to positively identify most species, indicating that within this sample most mineral species are complex metasomatic alteration phases. In addition, as with sample MP54_CS3, this contact shows no primary sedimentary features and the incorporation of the BIF xenolith is indicative of an intrusive contact.

Figure 4-20 Thin section of MP53_BIF showing BIF xenolith intercalated with dolerite material.

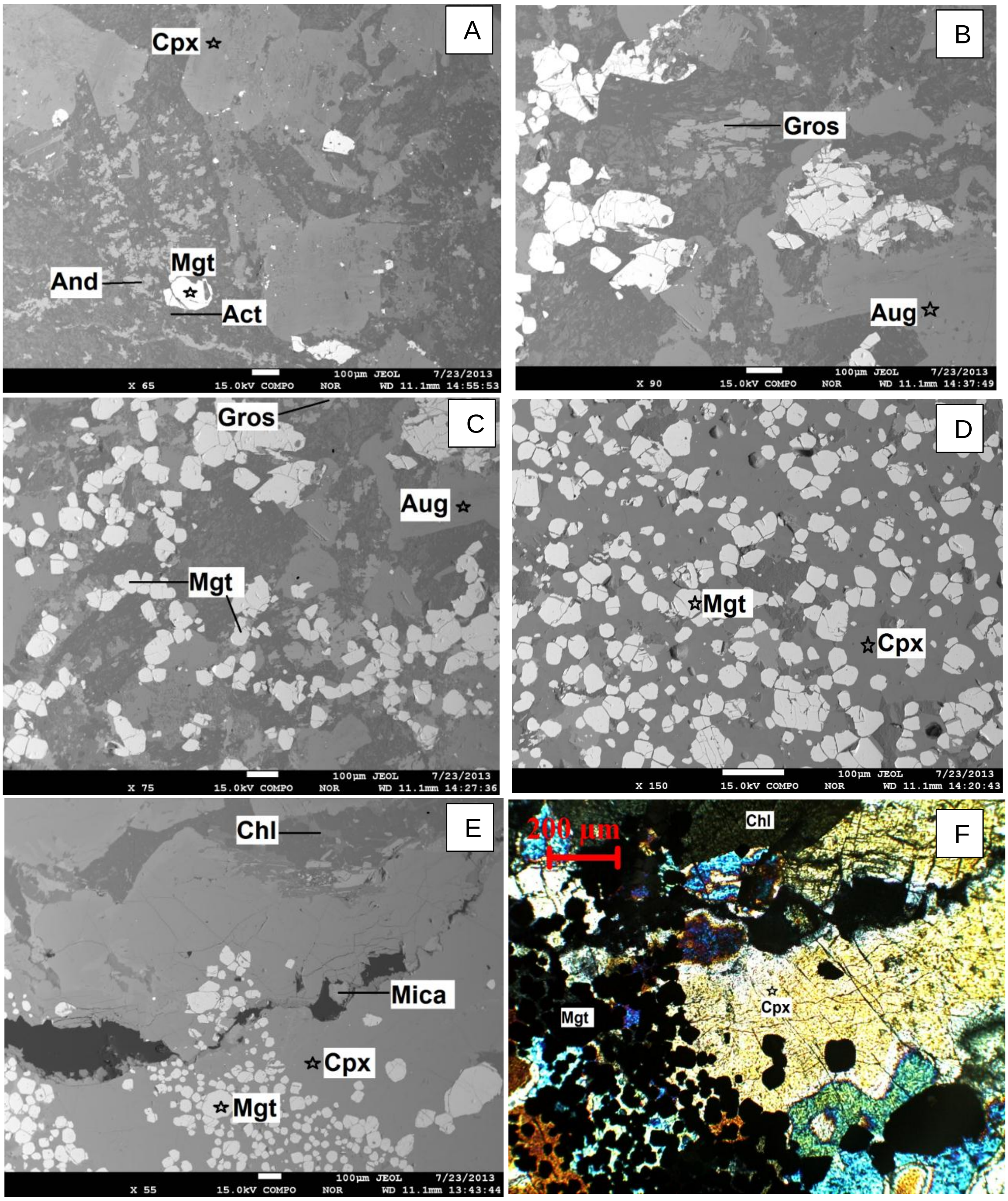

Figure 4-21 (A-F) Microprobe and optical (XPL) micrographs showing mineral identifications within sample MP53_BIF: Key- MGT= magnetite; CPX= clinopyroxene; Gross=grossular, mica=mica; Chl= chlorite; And= andradite; Act= actinolite; Aug= augite

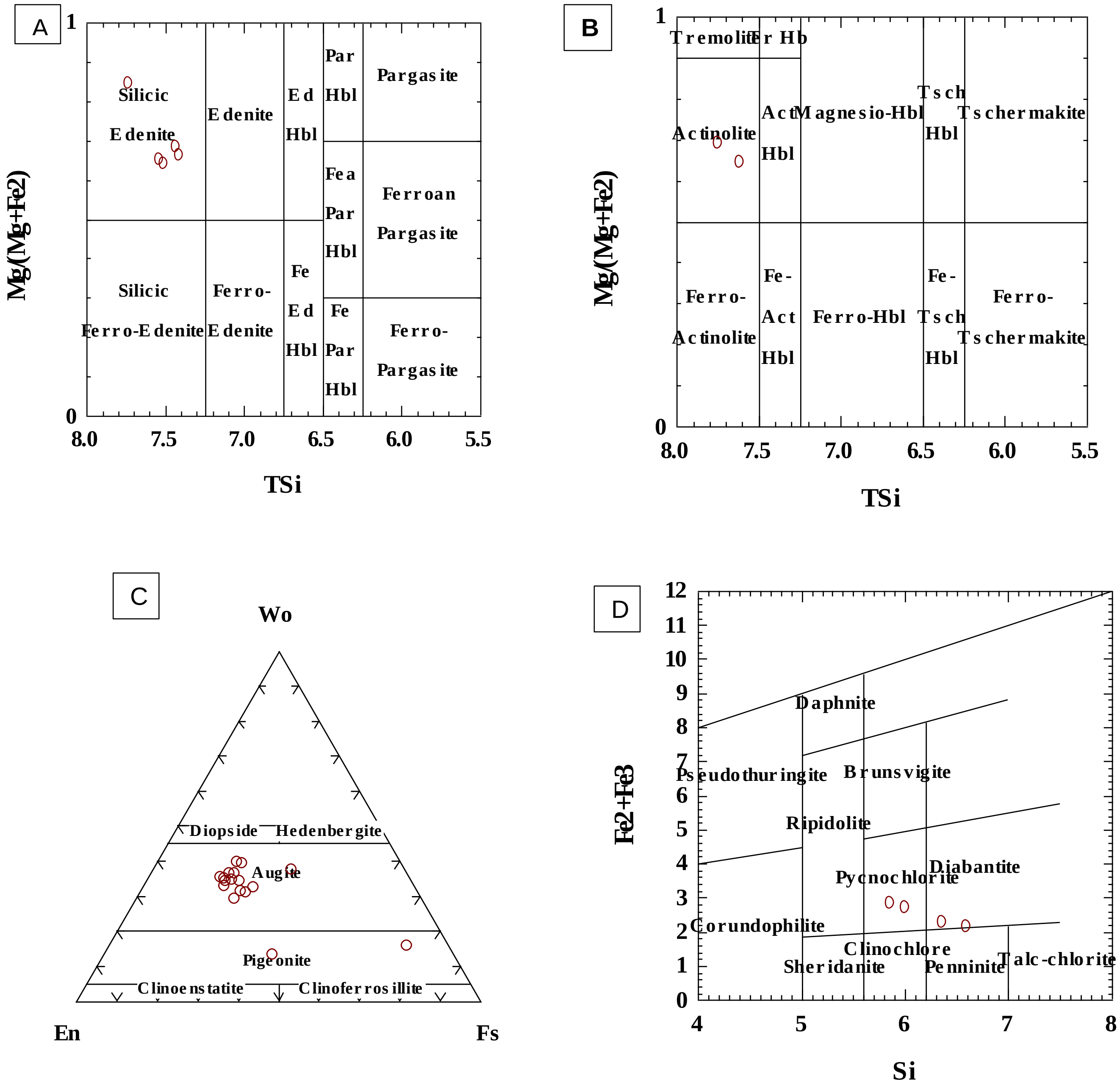

Figure 4-22 Mineral classification plots of sample MP53_BIF: A) Amphibole Total Si vs Mg(Mg+Fe$_2$) plot; ANa+AK>.05 (Hawthorne, 1981). B) Amphibole Total Si vs Mg(Mg+Fe$_2$) plot for calcic group ANa+AK <.05 (Hawthorne, 1981). C) Ternary end member diagram for pyroxenes (Morimoto, 1988) -D) Classification of Chlorite Microprobe Analyses (after Deer, et al., 1972).

Table 4-6 Representative mineral compositions MP54_BIF

Sample	Mineral	SiO_2	TiO_2	Al_2O_3	Cr_2O_3	Fe_2O_3	MnO	MgO	CaO	Na_2O	Total	Alm	And	Gross	Pyrope	Spess	Uvaro
MP53_BIF	Garnet	36.93	0.38	11.65	0.02	13.89	9.22	0.26	27.81	0.03	100.16	0.00	27.55	43.59	1.36	27.43	0.07
MP53_BIF	Garnet	36.32	0.54	10.14	0.02	16.83	5.91	0.79	29.47	0.03	100.04	0.00	34.60	42.80	4.31	18.23	0.07
MP53_BIF	Garnet	35.26	0.59	9.13	0.02	18.73	4.84	0.12	31.09	0.01	99.76	1.85	55.88	30.31	0.48	11.41	0.08
MP53_BIF	Garnet	36.50	0.43	9.31	0.00	16.57	7.19	0.05	29.61	0.04	99.71	0.00	51.90	30.08	0.24	17.79	0.00
MP53_BIF	Garnet	35.92	0.55	10.57	0.06	15.57	7.13	0.31	29.28	0.01	99.34	0.00	31.89	44.26	1.67	21.93	0.25

Sample	Mineral	Na_2O	SiO_2	CaO	Cr_2O_3	MgO	Al_2O_3	FeO	K_2O	TiO_2	MnO	Fe_2O_3	Mn_2O_3	Total
MP53_BIF	Amphibole	0.21	50.57	15.23	0.01	12.97	2.67	13.56	3.19	0.01	0.29			98.71
MP53_BIF	Amphibole	0.17	51.01	15.59	0.01	13.71	1.84	13.66	2.89	0.01	0.31			99.20
MP53_BIF	Amphibole	0.13	51.52	15.68	0.00	12.82	2.27	13.15	2.65	0.00	0.35			98.58

Sample	Mineral Name	Na_2O	SiO_2	CaO	Cr_2O_3	MgO	Al_2O_3	FeO	K_2O	TiO_2	MnO	Total
MP53_BIF	Fe Chlorite	0.02	28.95	0.07	0.01	18.92	18.34	15.82	0.02	0.00	6.53	88.67
MP53_BIF	Fe Chlorite	0.02	28.98	0.07	0.04	18.95	16.99	14.92	0.03	0.00	6.32	86.32
MP53_BIF	Fe Chlorite	0.01	32.70	0.12	0.00	22.48	16.11	13.11	0.04	0.00	5.26	89.83

Sample	Mineral	Na_2O	SiO_2	CaO	Cr_2O_3	MgO	Al_2O_3	FeO	K_2O	TiO_2	MnO	Fe_2O_3	Total
MP54_BIF	Pyroxene	0.27	50.55	16.30	0.06	15.68	2.68		0.04	0.26	1.80	12.02	99.66
MP54_BIF	Pyroxene	0.43	51.15	17.24	0.00	9.37	0.35	10.00	0.00	0.07	8.49	3.49	100.60
MP54_BIF	Pyroxene	0.18	48.14	15.27	0.09	15.44	2.74	15.00	0.01	0.23	2.14	1.27	100.51

Sample	Mineral	SiO_2	TiO_2	Al_2O_3	Fe_2O_3	FeO	MnO	MgO	CaO	Na_2O	K2O	Total
MP54_BIF	Feldspar	54.27	0.23	2.97	0	9.11	4.39	10.89	17.50	0.49	1.09	100.94

Sample	Mineral Name	SiO_2	CaO	Cr_2O_3	MgO	Al_2O_3	Fe_2O_3	FeO	Mn_2O_3	MnO	TiO_2	V2O3	NiO	Total
MP54_BIF	Magnetite	0.07	0.02	0.78	0.00	1.00	57.31	29.00	3.88	1.80	5.76	0.00	0.16	99.78
MP54_BIF	Magnetite	0.10	0.00	0.00	0.00	1.47	53.53	30.00	4.81	2.00	7.31	0.00	0.00	99.21
MP54_BIF	Magnetite	0.04	0.01	0.00	0.00	1.22	54.20	30.00	4.64	2.00	6.75	0.00	0.11	98.96

Chapter 5 Geochemical Results

The Middelplaats rock samples analysed for this report consist of two different rock types: 1) Intrusive igneous rocks and 2) Chemical sedimentary ore. Therefore, this chapter will present the data by rock type, as the method of analysing the results is quite different. The igneous results will be shown with accompanying plots and graphs, whereas the manganese ore results will largely consist of data in a table as the bulk of the analysis needed is comparative in nature, and will be discussed in Chapter 6.

5.1 *Middelplaats igneous rock geochemical results*

5.1.1 Major and trace element analysis of the Middelplaats igneous rocks

Major and trace element results from XRF analysis of the Middelplaats igneous rocks are presented as Table 5-1. These data for the igneous samples were first plotted on the total alkalis versus silica (TAS) diagram (Figure 5-1) of Middlemost, (1994) to determine the geochemical rock classification. All igneous samples were found to be “gabbroic diorite” which is congruent with the QAPF classification of “Dolerite”. Trace element plots “Spider diagrams” of the Middelplaats igneous samples were then plotted normalized to MORB using values from McDonough & Sun (1995) and are presented as Figure 5-2. The Middelplaats igneous samples show enrichments in the large ion lithophile elements (LILE) K, Rb and Sr, light rare earth elements (LREE) La, Ce and Nb. The samples also show a depletion in HFSE Ti and Y however, Th is enriched. This is consistent with published data on mafic dyke swarms emplaced during the Proterozoic (Tarney & Weaver, 1987).

Three different plots have been used in order to establish a probable source region and characterization for the Middelplaats igneous rock samples. This is in part due to examination of the TAS diagram and trace element plots “spider diagrams” and prior classification of the Ongeluk lavas by other researchers (e.g. Eriksson, et al., 1993; Cornell, et al., 1996). N-type MORB basalts from “normal” mid-ocean ridge environments are depleted in incompatible trace elements and E-Type MORB ocean floor basalts from plume influenced regions such as the lavas currently forming in Iceland are generally enriched in incompatible trace elements (Fitton, et al., 1997). Figure 5-3 is a variation diagram after Meschede (1986) and Figure 5-4 is from Fitton et al., (1997). Both use the elements Nd, Y and Zr to exploit the unusual behaviour of Nb during the melting processes that results in a generally depleted upper mantle (Rollinson, 1993; Fitton, et al., 1997). Figure 5-3 shows all samples plot within the “within plate tholeiites and volcanic-arc basalts” field and Figure 5-4 shows the Middelplaats igneous samples could have a plume-related source. Figure 5-5 plots molar weights of Na_2O, K_2O and Al_2O_3. Igneous rocks are subdivided into three groups according to this classification: peraluminous, metaluminous and peralkaline. All Middelplaats igneous samples plotted as metaluminous ($Na_2O+K_2O+CaO>Al_2O_3$).

Table 5-1 Major and trace element data for Middelplaats igneous samples. Major elements are in wt% and trace elements in ppm.

Sample name	**MP53-S1**	**MP53-S2**	**MP54-S1**	**MP54-S2**
SiO_2	54.4	54.925	52.484	55.112
TiO_2	0.436	0.579	0.457	0.567
Al_2O_3	11.866	13.941	13.497	14.76
Fe_2O_3	11.492	11.151	10.645	11.181
MnO	0.209	0.25	0.2	0.195
MgO	11.409	6.188	7.074	5.424
CaO	6.27	8.133	9.259	6.238
Na_2O	1.338	1.965	1.762	3.145
K_2O	1.469	1.763	1.34	1.773
P_2O_5	0.069	0.098	0.078	0.099
LOI	1.59	1.89	3.23	2.49
H_2O	0.38	0.42	0.32	0.24
Total	100.927	101.303	100.344	101.224
Sample Name	MP53_S1	MP53_S2	MP54_S1	MP54_S2
V	190.7	206.2	182.6	199
Cr	842.4	218.3	380	123.4
Mn	1604.5	1902.3	1529.9	1529.3
Co	59	45.4	52.2	50.1
Ni	222	99.5	140.6	89
Cu	54.8	76.9	60.5	78.4
Zn	81	76.4	77.4	85.1
Rb	80.5	97.7	84.4	122.6
Sr	129.5	209.5	133.8	138.4
Y	16.1	21.3	17.8	21.1
Zr	72.3	98.9	77.9	97.6
Nb	5.1	6.4	5.8	6.6
La	13.2	15.1	12.5	15.3
Ce	24.3	39.9	30.3	35.2
Nd	10.7	18.7	12.5	14.8
Pb	11	9.4	9.2	6.3
Th	4.9	8.5	6.7	6.5
U	2.3	2.1	2.2	1.7

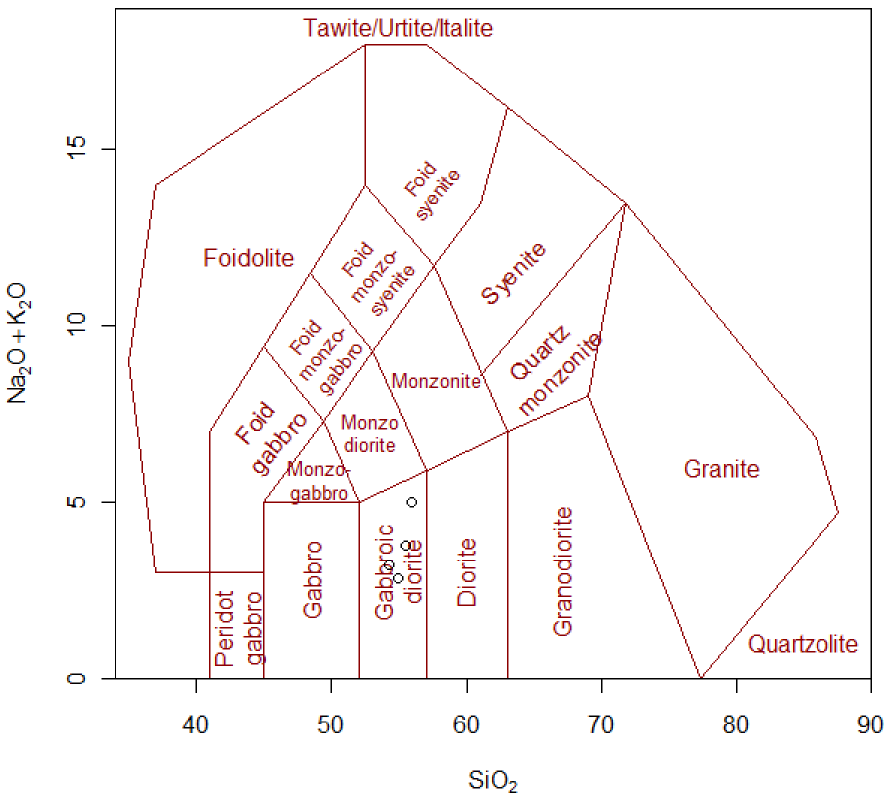

Figure 5-1 Total alkali vs. silica TAS classification diagram for the Middelplaats igneous samples. After Le Maitre, et al., (2002)

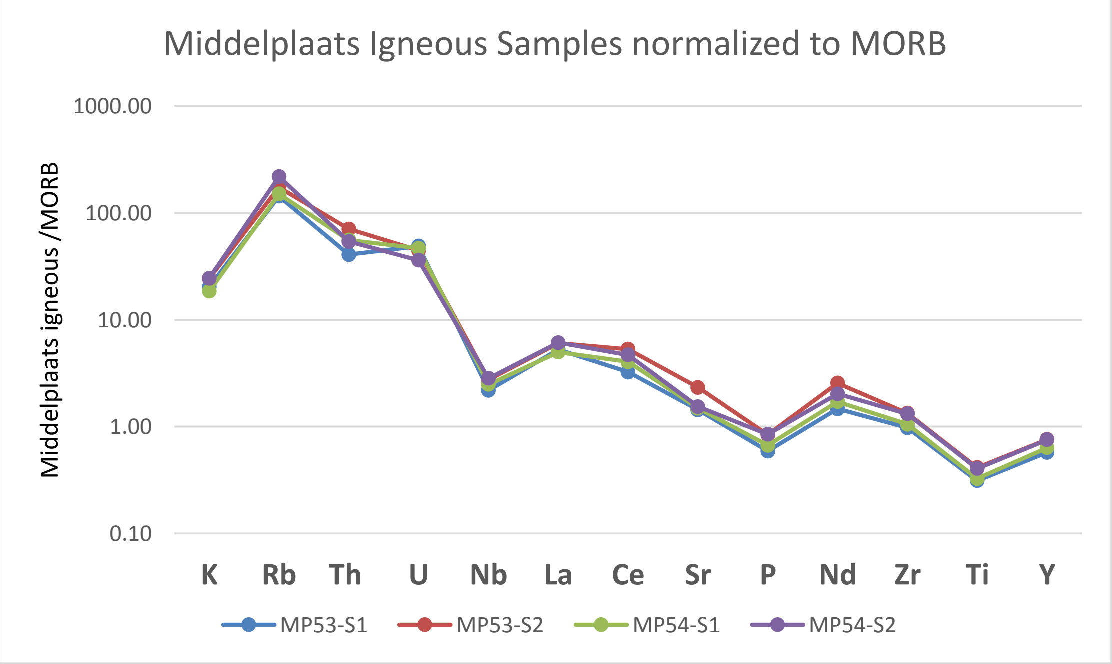

Figure 5-2 Trace element plots for the Middelplaats igneous samples normalized to MORB.

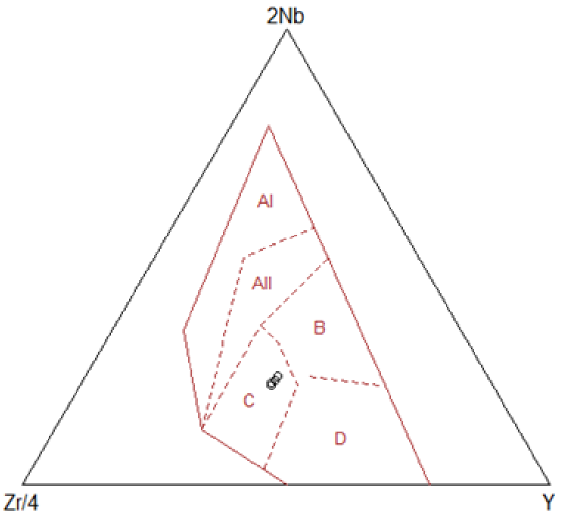

Figure 5-3 Discrimination diagram from Meschede (1986) Zr/4-2Nb-Y for Middelplaats igneous samples; The fields are defined as follows: AI- within plate alkali basalts; AII- within plate alkali basalts and within plate tholeiites; B- E-Type MORB; C- within plate tholeiites and volcanic-arc basalts; D- N type MORB and volcanic-arc basalts.

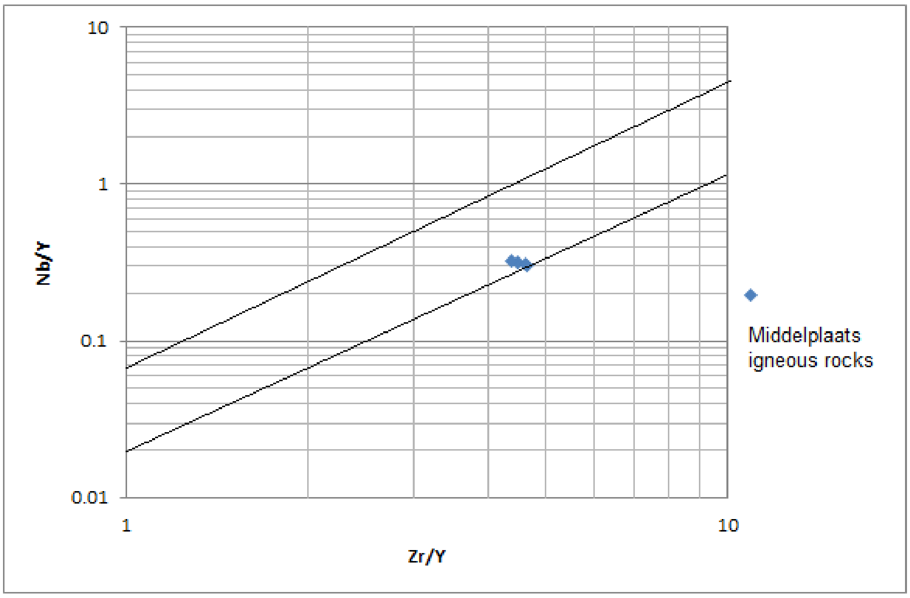

Figure 5-4 Variation diagram of Fitton, et al., (1997); this plot uses Nb/Y versus Zr/Y to exploit the behaviour of Nb during melting processes that results in a generally depleted upper mantle; Rocks that plot within the parallel blue lines have been demonstrated to have a plume related source region. All Middelplaats igneous samples plot within the "plume related" field.

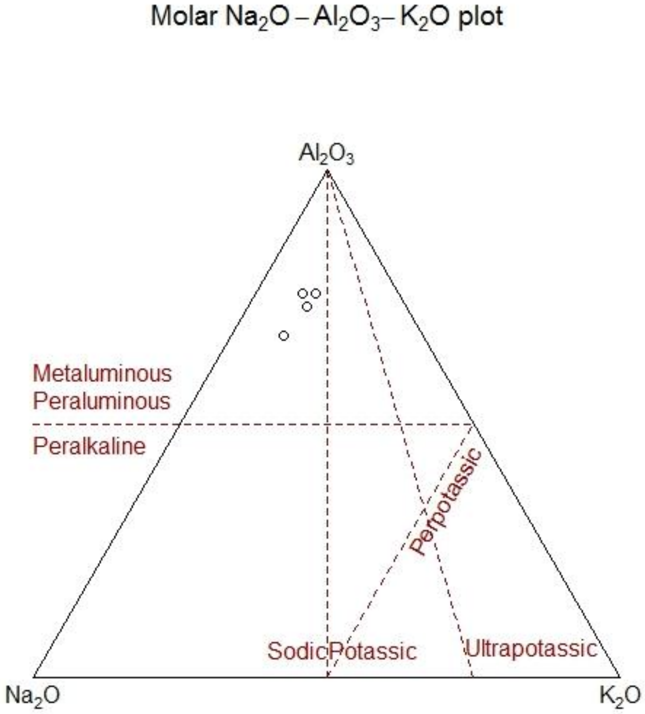

Figure 5-5 Molar weights of Na2O, K2O and Al2O3 for the Middelplaats igneous samples. After Le Maitre, et al., (2002)

5.1.1.1 Alteration of the Middelplaats igneous rocks

The Middelplaats igneous samples also show a slight but significant increase in K. Published data on dolerites occurring in Southern Africa from Huntner & Halls, (1992) and Bullen, et al.,(2012) report average K for dolerites of ~ 0.6 to 0.9 wt%, whereas the Middelplaats samples average 1.59 wt%. As noted in section 4.1.3, most of the origional plagioclase feldspars appear altered to a potassic feldspar and to a lesser degree chlorite and epidote. Clinopyroxenes also show some alteration to amphibole, chlorite, epidote and calcite. This mineral assemblage is consistent with a potassic or alkali hydrothermal fluid (Figure 5-6).

In addition, although no ¼ core off cuts were available from Middelplaats sample MP54_CS3 for testing, microscopic examination of the thin section shows a similar potassic alteration in the lower portion of the sample away from the effects of the contact metamorphism.

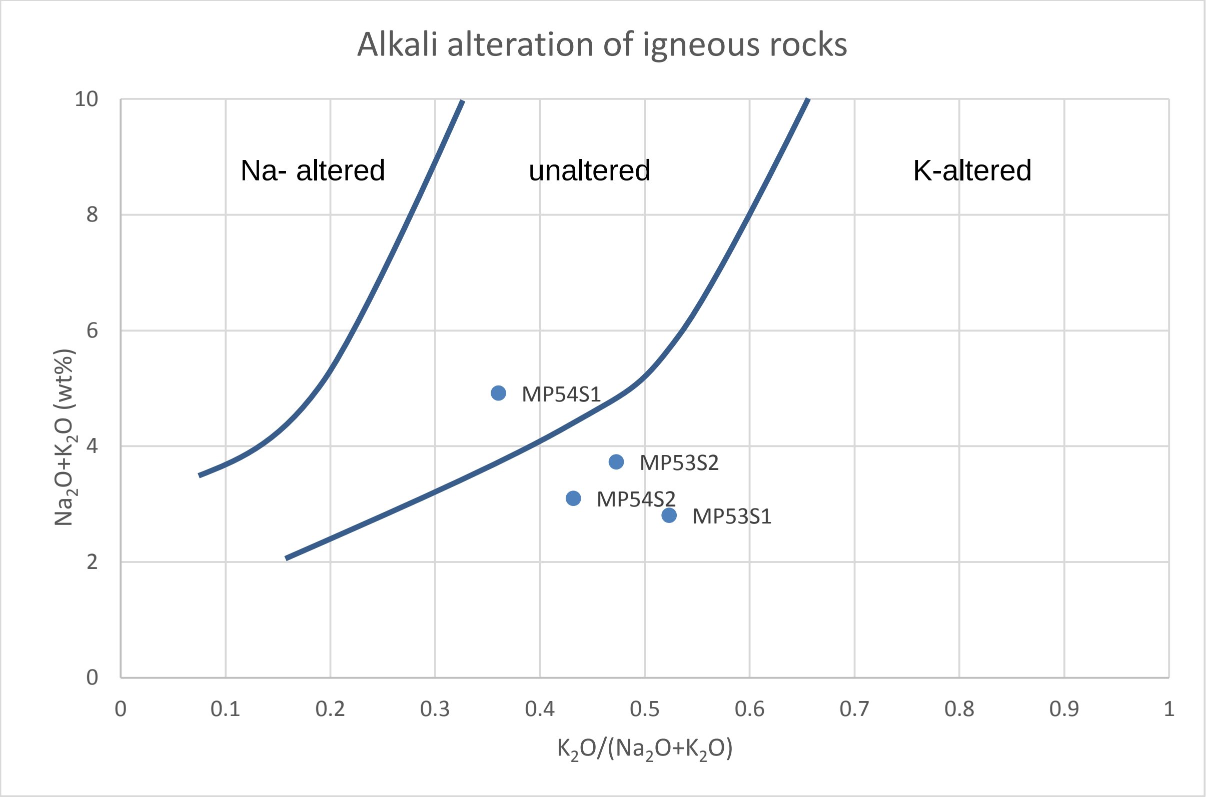

Figure 5-6 K and Na alteration of the Middelplaats igneous rocks plotted on the classifaction diagram of Hughes, (1973). The Middelplaats rocks show a slight potassic alteration trend.

5.2 *Major and trace element analysis of the Middelplaats manganese ore samples*

Major and trace element results from XRF analysis of the Middelplaats manganese ore samples are presented as Table 5-2. As there is no standardized classification diagram for manganese ore, the main elements Fe_2O_3, MnO and CaO, have been plotted on a standard ternary diagram to illustrate the bulk chemical compositional differences between the Middelplaats low-grade and high-grade ores (Figure 5-7).

Table 5-2 Major and trace element data for Middelplaats manganese ore samples. Major elements are in wt% and trace elements in ppm. *ND= not determined - below or above detection levels.

Middelplaats manganese ore samples	MP54_567	MP54_515
SiO_2	4.3	6.62
TiO_2	0.03	0.03
Al_2O_3	0.16	0.04
Fe_2O_3	5.38	9.27
MnO	42.52	67.8
MgO	2.98	2.36
CaO	27.54	9.86
Na_2O	0	0
K_2O	0	0
P_2O_5	0.04	0.06
LOI	16.77	2.92
H_2O	0.53	0.24
Total	100.26	99.2
Sample Name	MP54_567	MP54_515
V	11.4	17.2
Cr	7.5	8.9
Mn	ND	ND
Co	15.4	8.7
Ni	16.4	14.3
Cu	30.3	45.9
Zn	36.9	35.4
Rb	0.8	0.5
Sr	189.5	13.6
Y	12.4	11.7
Zr	5.9	5.6
Nb	2.4	0.7
La	ND	ND
Ce	ND	ND
Nd	ND	ND
Pb	3.1	2.6
Th	1.7	0
U	0	0.2

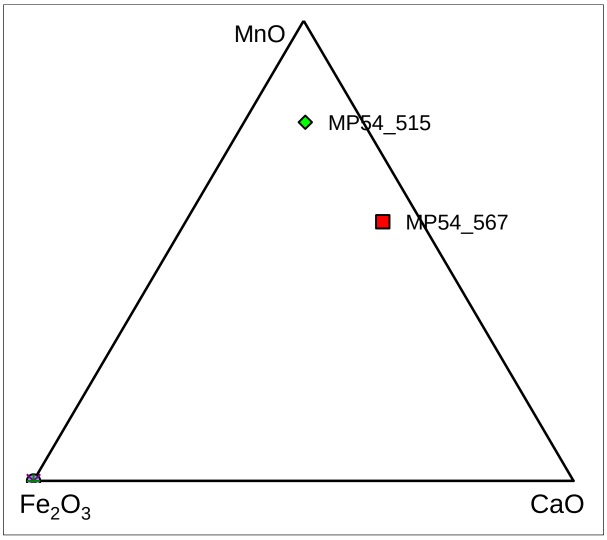

Figure 5-7 Ternary diagram showing the main elements (Fe2O3, MnO and CaO) in the Middelplaats manganese ore. Elements in wt% normalized to 100%.

Chapter 6 Discussion

As stated in section 1.5 (Project aims and objectives), one of the goals of this project is to establish if the igneous rock underlying the manganese ore in boreholes MP53 and MP54 at the Middelplaats mine have a genetic link or other relationship to the Ongeluk Formation. Additionally, to characterize what if any effect the emplacement of the igneous rocks had on the manganese ore. To facilitate this, two additional data sets will be used to develop comparative data. Regional and composite geochemical data from the Ongeluk Formation (hereafter referred to as Ongeluk data), published by Cornell, et al., (1996), and average Mamatwan-type and Wessels-type ore compositions in weight % from Miyano & Beukes, (1987). As with the preceding chapter, igneous data will be discussed and analysed first, followed by the manganese ore.

6.1 *Comparison of major and trace element data for the Ongeluk Formation with the Middelplaats igneous samples*

Regional and composite geochemical data from the Ongeluk Formation published by Cornell, et al., (1996), is presented here for comparative purposes. These data were selected from “Massive Lava”, “Pillow Core” and composite “Regional Ongeluk” to reduce the localized effects of hydrothermal and/or metamorphic alteration. Eight samples of major and trace element analysis of these published data are presented as Table 6-1. Also presented are the calculated standard deviations between elements for both sample sets (Ongeluk and Middelplaats) as Table 6-2. All plots of this data will also contain data from the Middelplaats igneous samples so that visual correlation may be made. In all cases where available, the extrusive rock plots have been used. The intent is to classify the Ongeluk samples whilst simultaneously allowing comparison of the extrusive Ongeluk Formation with the intrusive dolerites of the Middelplaats mine.

Table 6-1 Major and trace element data for Ongeluk Formation igneous samples. Major elements are in wt% and trace elements in ppm. *ND= not determined - below detection levels.

Sample Name	77392 Massive lava	77397 Massive lava	88BA6 Pillow core	90BA20 Pillow core	Regional Ongeluk n=104	Selected Ongeluk n=38	Boven Ongeluk n=7	Bosch Aar n=4
SiO_2	54.67	53.21	54.96	52.41	56.24	56.04	55.56	55.2
TiO_2	0.56	0.64	0.64	0.64	0.65	0.65	0.66	0.64
Al_2O_3	14.33	14.13	13.36	14.52	14.32	14.52	14.55	14.74
Fe_2O_3	10.33	10.03	11.44	10.09	10.65	10.78	10.89	10.86
MnO	0.14	0.13	0.14	0.15	0.14	0.14	0.15	0.14
MgO	5.75	5.79	6.71	5.73	5.84	5.93	5.8	5.86
CaO	7.96	9	5.56	9.76	8.87	8.79	9.83	8.82
Na_2O	2.64	2.52	3.69	3.89	2.66	2.77	2.64	2.87
K_2O	0.32	0.77	0.33	0.18	0.76	0.62	0.23	0.91
P_2O_5	0.08	0.08	0.1	0.11	0.1	0.1	0.09	0.1
LOI	4.11	3.81	3	2.79	ND	ND	ND	ND
H_2O	0.34	0.29	0.16	0	ND	ND	ND	ND
Total	101.23	100.4	100.09	100.27	100.23	100.34	100.4	100.14
Sample Name	77392 Massive lava	77397 Massive lava	88BA6 Pillow core	90BA20 Pillow core	Regional Ongeluk n=104	Selected Ongeluk n=38	Boven Ongeluk n=7	Bosch Aar n=4
V	202	211	218	196	201.1	203.4	211.9	217
Cr	176	88	92	93	128.4	126.6	82.7	85.5
Ni	72	81	96	80	84	85.1	86.6	87.8
Cu	63	68	65	59	62.2	61.5	66.6	70.5
Zn	69	76	92	56	69.9	73.6	76.6	79.5
Ga	11	8	11	17	14.6	14.6	15.5	ND
Rb	14	34	13	6	34.5	32.4	14.1	36.8
Sr	216	172	104	89	164.1	210	195.1	270.8
Y	23	22	23	20	22.5	22.7	24	22.8
Zr	110	105	108	91	104.2	104.5	105	104.5
Nb	7	6	6	4	5.8	5.6	5.9	5.8
Ba	141	360	124	58	256.9	268.2	145.4	312.3
Pb	ND	4	5	4	8.5	7.3	5.1	6.8
Th	7	9	6	5	6.8	6.8	5.7	6.8
U	ND	9	9	9	1.7	1.8	1.4	1.6

Table 6-2 Standard deviations between elements in the Middelplaats and Ongeluk sample sets

Sample Name+O20A1:OA1:O27	77392 Massive lava	77397 Massive lava	88BA6 Pillow core	90BA20 Pillow core	Regional Ongeluk n=104	Selected Ongeluk n=38	Boven Ongeluk n=7	Bosch Aar n=4	**MP53-S1**	**MP53-S2**	**MP54-S1**	**MP54-S2**	Standard deviation
SiO_2	54.67	53.21	54.96	52.41	56.24	56.04	55.56	55.20	54.40	54.93	52.48	55.11	1.27
TiO_2	0.56	0.64	0.64	0.64	0.65	0.65	0.66	0.64	0.44	0.58	0.46	0.57	0.08
Al_2O_3	14.33	14.13	13.36	14.52	14.32	14.52	14.55	14.74	11.87	13.94	13.50	14.76	0.82
Fe_2O_3	10.33	10.03	11.44	10.09	10.65	10.78	10.89	10.86	11.49	11.15	10.65	11.18	0.48
MnO	0.14	0.13	0.14	0.15	0.14	0.14	0.15	0.14	0.21	0.25	0.20	0.20	0.04
MgO	5.75	5.79	6.71	5.73	5.84	5.93	5.80	5.86	11.41	6.19	7.07	5.42	1.62
CaO	7.96	9.00	5.56	9.76	8.87	8.79	9.83	8.82	6.27	8.13	9.26	6.24	1.43
Na_2O	2.64	2.52	3.69	3.89	2.66	2.77	2.64	2.87	1.34	1.97	1.76	3.15	0.73
K_2O	0.32	0.77	0.33	0.18	0.76	0.62	0.23	0.91	1.47	1.76	1.34	1.77	0.58
P_2O_5	0.08	0.08	0.10	0.11	0.10	0.10	0.09	0.10	0.07	0.10	0.08	0.10	0.01
LOI	4.11	3.81	3.00	2.79	ND	ND	ND	ND	1.59	1.89	3.23	2.49	0.87
H_2O	0.34	0.29	0.16	0.00	ND	ND	ND	ND	0.38	0.42	0.32	0.24	0.14
Total	101.23	100.40	100.09	100.27	100.23	100.34	100.40	100.14	100.93	101.30	100.34	101.22	0.46
Sample Name	77392 Massive lava	77397 Massive lava	88BA6 Pillow core	90BA20 Pillow core	Regional Ongeluk n=104	Selected Ongeluk n=38	Boven Ongeluk n=7	Bosch Aar n=4	MP53_S1	MP53_S2	MP54_S1	MP54_S2	
V	202.00	211.00	218.00	196.00	201.10	203.40	211.90	217.00	190.70	206.20	182.60	199.00	10.49
Cr	176.00	88.00	92.00	93.00	128.40	126.60	82.70	85.50	842.40	218.30	380.00	123.40	218.42
Ni	72.00	81.00	96.00	80.00	84.00	85.10	86.60	87.80	222.00	99.50	140.60	89.00	41.53
Cu	63.00	68.00	65.00	59.00	62.20	61.50	66.60	70.50	54.80	76.90	60.50	78.40	7.03
Zn	69.00	76.00	92.00	56.00	69.90	73.60	76.60	79.50	81.00	76.40	77.40	85.10	8.90
Rb	14.00	34.00	13.00	6.00	34.50	32.40	14.10	36.80	80.50	97.70	84.40	122.60	38.68
Sr	216.00	172.00	104.00	89.00	164.10	210.00	195.10	270.80	129.50	209.50	133.80	138.40	53.06
Y	23.00	22.00	23.00	20.00	22.50	22.70	24.00	22.80	16.10	21.30	17.80	21.10	2.34
Zr	110.00	105.00	108.00	91.00	104.20	104.50	105.00	104.50	72.30	98.90	77.90	97.60	11.98
Nb	7.00	6.00	6.00	4.00	5.80	5.60	5.90	5.80	5.10	6.40	5.80	6.60	0.76
Pb	ND	4.00	5.00	4.00	8.50	7.30	5.10	6.80	11.00	9.40	9.20	6.30	2.35
Th	7.00	9.00	6.00	5.00	6.80	6.80	5.70	6.80	4.90	8.50	6.70	6.50	1.22

Figure 6-1 plots the Ongeluk and Middelplaats data on the extrusive rock TAS diagram of Le Maitre, et al., (2002). All samples plotted as “basaltic andesite”. Trace element plots “Spider diagrams” of the Ongeluk and Middelplaats samples were plotted normalized to MORB using values from McDonough & Sun (1995) and are presented as Figure 6-2. (Please note, the elements U, La and Ce used in the Middelplaats spider diagram above were not available for the Ongeluk). The Ongeluk and Middelplaats data are quite similar, with the variance between the Middelplaats rocks and the Ongeluk data being smaller than the variance between the various Ongeluk samples. All samples show enrichments in K, Rb, Sr, Th and Nb, with depletions in Ti and Y. Geotectonic classification for the Ongeluk data uses the same Zr/4 -2Nb-Y diagram (Figure 5-3) of Meschede, (1986) and Nb/Y-ZrY of Fitton, et al., (1997) as above. Both the Ongeluk and Middelplaats data plot in the “within plate tholeiites and volcanic-arc basalts” field and there is some overlapping of data points.

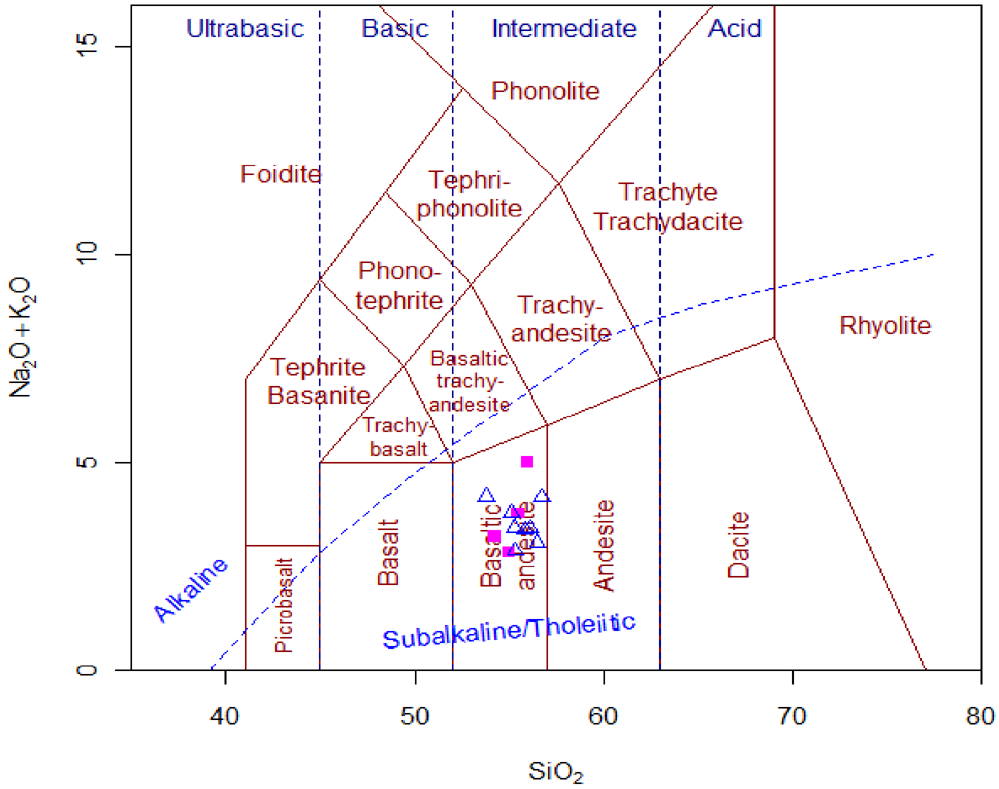

Figure 6-1 TAS classification diagram for extrusive rocks. Ongeluk sample data are blue triangles and Middelplaats igneous samples are pink squares. After Le Maitre, et al., (2002)

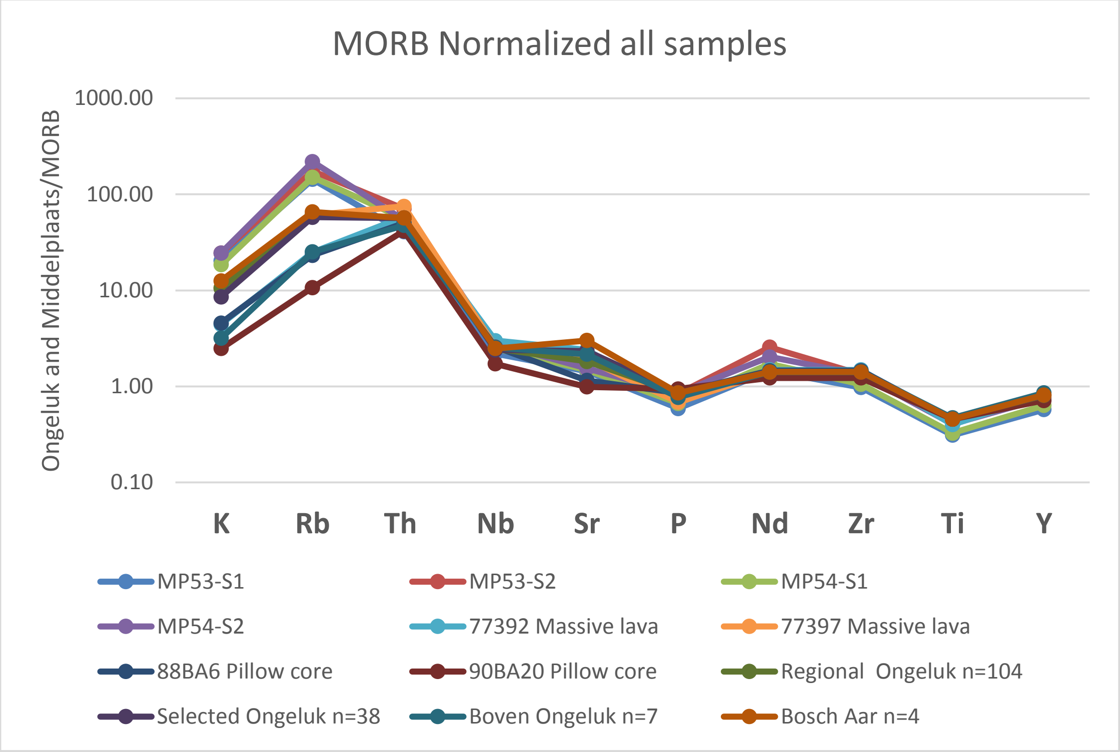

Figure 6-2 Trace element "spider diagram" plots for the Ongeluk data and Middelplaats igneous rock samples.

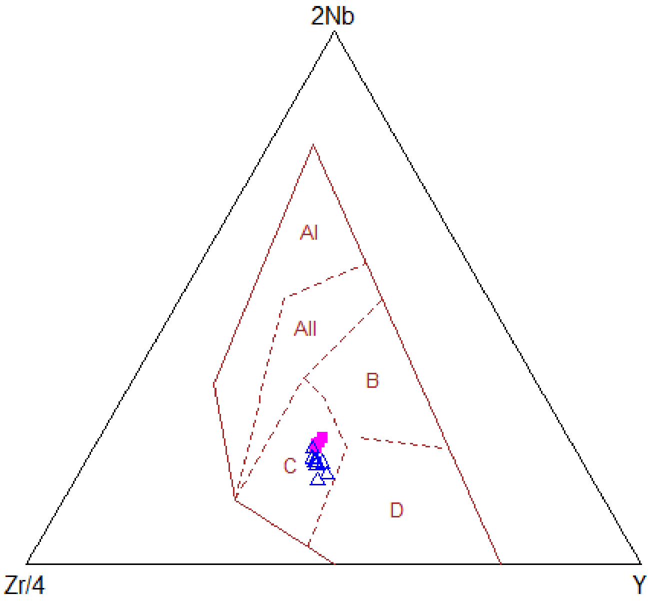

Figure 6-3 Discrimination diagram from Meschede (1986) Zr/4-2Nb-Y for the Ongeluk data and Middelplaats igneous samples; The fields are defined as follows: AI- within plate alkali basalts; AII- within plate alkali basalts and within plate tholeiites; B- E-Type MORB; C- within plate tholeiites and volcanic-arc basalts; D- N type MORB and volcanic-arc basalts. Blue triangles =Ongeluk; pink squares=Middelplaats igneous rocks.

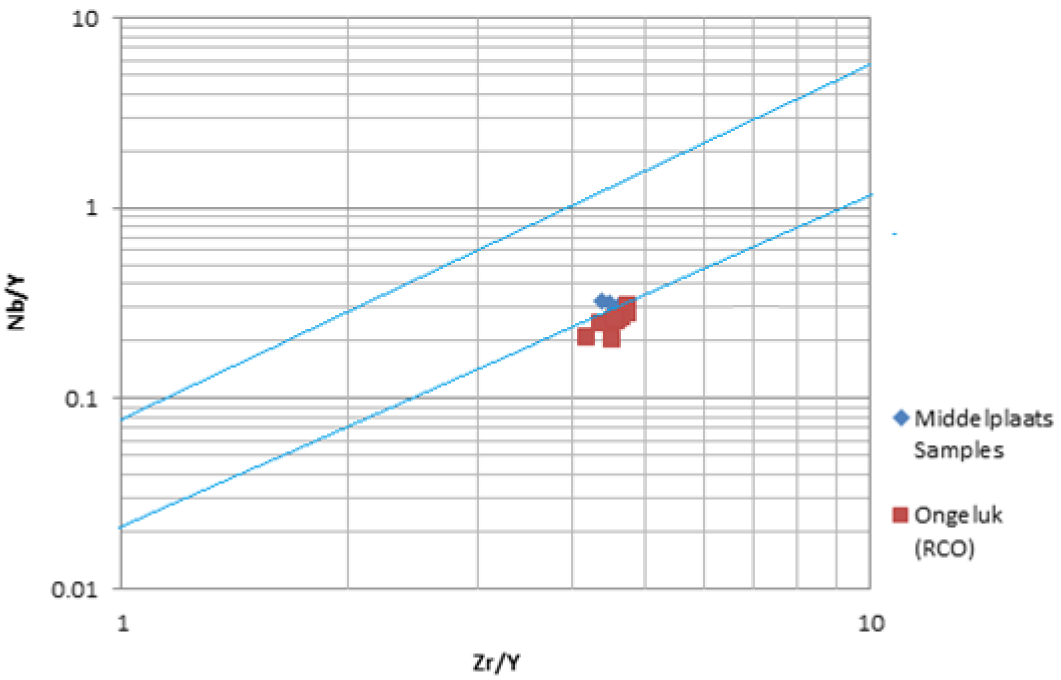

Figure 6-4 Variation diagram of Fitton, et al., (1997); this plot uses Nb/Y versus Zr/Y to exploit the behaviour of Nb during melting processes that results in a generally depleted upper mantle; Rocks that plot within the parallel blue lines have been demonstrated to have a plume related source region. All Middelplaats igneous samples plot within the "plume related" field. Ongeluk data plot on the lower limit of the established base line.

6.1.1 Element mobility- Bivariate Diagrams

According to Pearce (1968) when an immobile element is plotted on the horizontal axis of a bi-variate diagram and another generally immobile element plotted on the vertical axis; if the two elements are generally incompatible and immobile, samples originating from a co-genetic source region will plot as a straight line (i.e. unity). These plots serve two purposes: 1) establish which elements appear to be immobile and 2) examine if the rocks appear to be from a co-genetic source.

Due to the extremely small sample set and high level of hydrothermal alteration within the Ongeluk Formation Wiggering & Beukes, (1990); Cornell, et al., (1996), straight lines (unity) do not develop even within samples taken from rocks physically known to be related (i.e. MP53_S1, MP53_S2 and MP54_S1 and MP54_S2). Therefore, for the purposes of this report, a range (distance) between points will be used. The distance has been established by using the plotted distance of one element from a known genetically related sample. The relationships between elements in sample MP53_S1 and the same element in MP53_S2 will be used to determine the acceptable range. These samples are taken from a continuous drill core through the doloritic material and are separated by less than 2 meters. This method, although not exact, should provide a means to overcome the inherent variations created by the small sample set and hydrothermal alteration (Pearce, 1987; Russell & Nicholls, 1988). Furthermore, this method should compensate for the artificial variance created by using the composite and regional Ongeluk data.

Trace and REE data were first plotted against Nd (Figure 6-5) to establish and/or define the level of incompatibility and immobility of the elements available. These data were then used to plot ratio/ratio quad-variate diagrams. Please also note, in these diagrams there are three very slight trends (Ongeluk massive lava, Ongeluk regional and composite and Middelplaats). Which would be consistent with a fractionating source region.

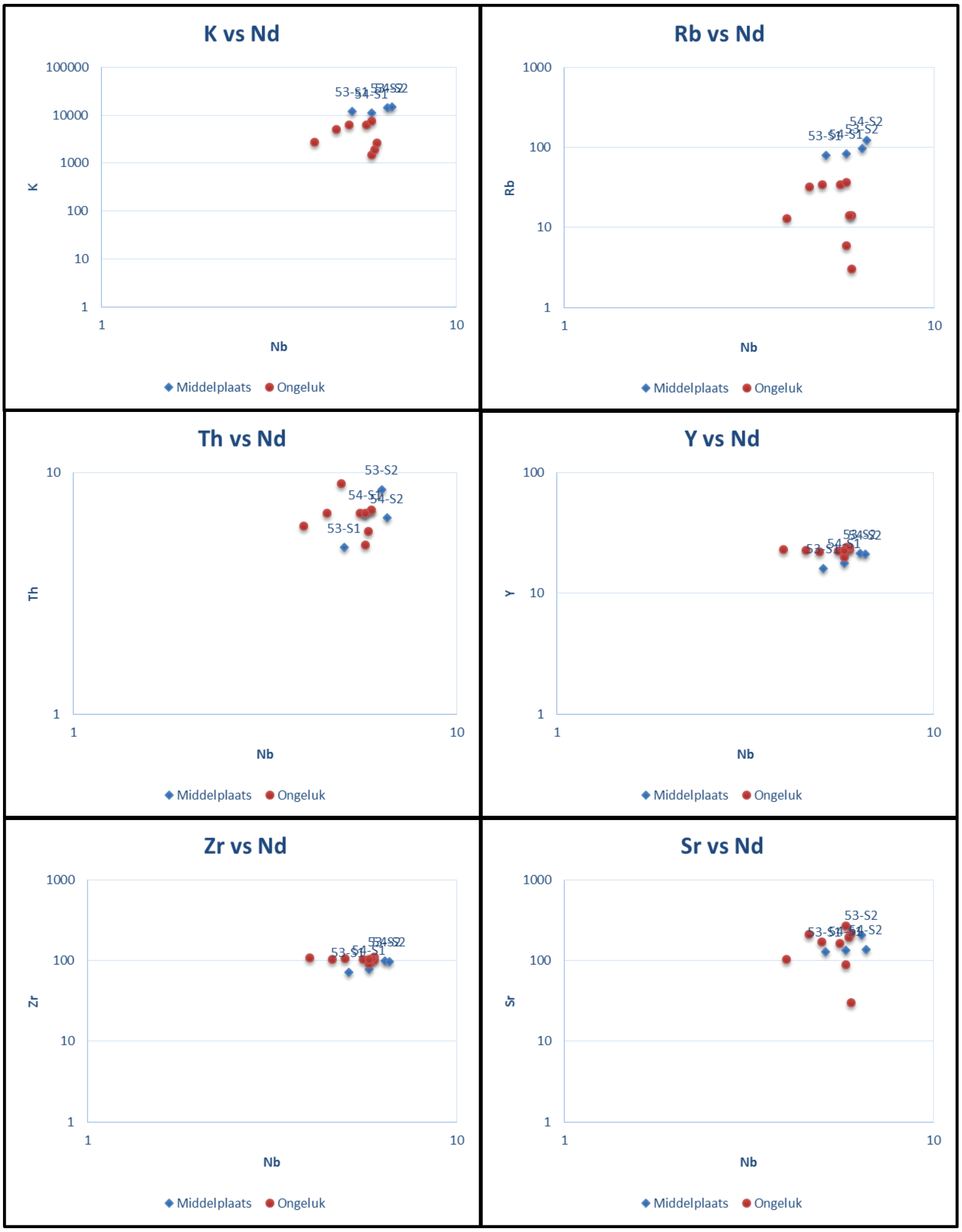

Figure 6-5 Bivariate diagrams of Nd vs other elements. Visual correlation is given by comparison of the distance between the known genetically identical samples MP53_S1 and S2 samples. Results in PPM.

6.1.2 Ratio versus ratio of generally incompatible and immobile elements

Similar to the bi-variate diagrams above; ratio/ratio diagrams put the ratio of 2 incompatible/immobile elements on the horizontal axis, and a similar ratio of incompatible/immobile elements on the vertical axis of the diagram. If the samples are from a co-genetic source region, they will plot in the in the same area (data will overlap and/or plot on top of one another) (Pearce, 1968). From examination of Figure 6-5, the least mobile elements appear to be: Sr, Y, Zr, Nb and Th. These elements show the least scatter, taking into account the acceptable range between points is equal to the distance between the points for MP53_S1 and MP53_S2. Using these apparently immobile and incompatible elements, two ratio/ratio diagrams were constructed. As with the bivariate diagrams, Figure 6-6 uses the distance between the points for MP53S1 and S2 as the acceptable range to show overlapping data.

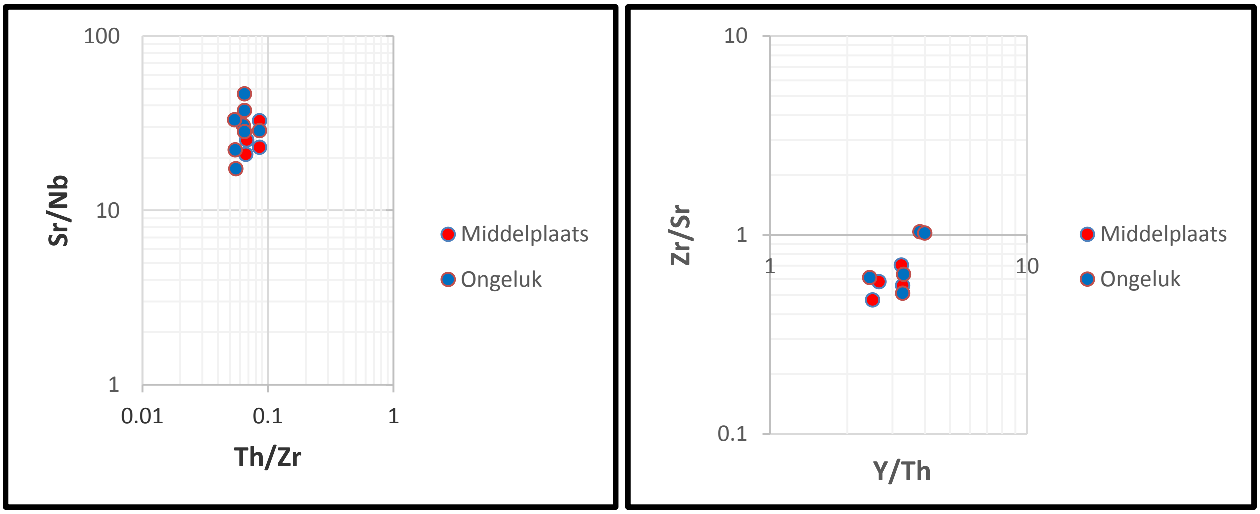

Figure 6-6 Ratio/ratio diagrams from selected elements that appear immobile and incompatible within Middelplaats igneous samples and Ongeluk data. Data reported in PPM.

6.2 *Comparison of major element data of the Middelplaats manganese ore with Wessels and Mamatwan-type ores*

6.2.1 Middelplaats manganese ore bulk rock composition

Data on the average composition of the two main types of manganese ore in the Hotazel Formation (Wessels and Mamatwan) by Miyano & Beukes, (1987) are presented as Table 6-3. These data have been used as a base line for major element analysis of the high-grade and low-grade Middelplaats ore. Spider diagrams (Figure 6-7 and Figure 6-8) of the Middelplaats samples were plotted normalized to "average" Mamatwan and Wessels-type ore. These graphs demonstrate mass enrichment and/or depletion as well as compositional variations from the two main ore types in the Hotazel Formation.

Table 6-3 Average Mamatwan and Wessels-type ore compositions in weight %. Data is from Miyano and Beukes, (1987) after SAMANCOR, (1969).

Kalahari Manganese Samples	MP54_567	MP54_515	Average Mamatwan	Average Wessels
SiO_2	4.30	6.62	4.00	6.00
TiO_2	0.03	0.03	0.00	0.00
Al_2O_3	0.16	0.04	1.00	1.00
Fe_2O_3	5.38	9.27	8.60	15.70
MnO	42.52	67.80	54.60	67.50
MgO	2.98	2.36	4.00	1.00
CaO	27.54	9.86	14.00	5.00
Na_2O	0.00	0.00	0.40	0.40
K_2O	0.00	0.00	0.05	0.02
P_2O_5	0.04	0.06	0.05	0.05
LOI*	16.77	2.92	8.80	1.02
H_2O	0.53	0.24	3.50	2.30
Total	100.26	99.20	99.00	99.99

*Loss on ignition for average Wessels and Mamatwan ores was calculated by total with H_2O minus 100 to give LOI.

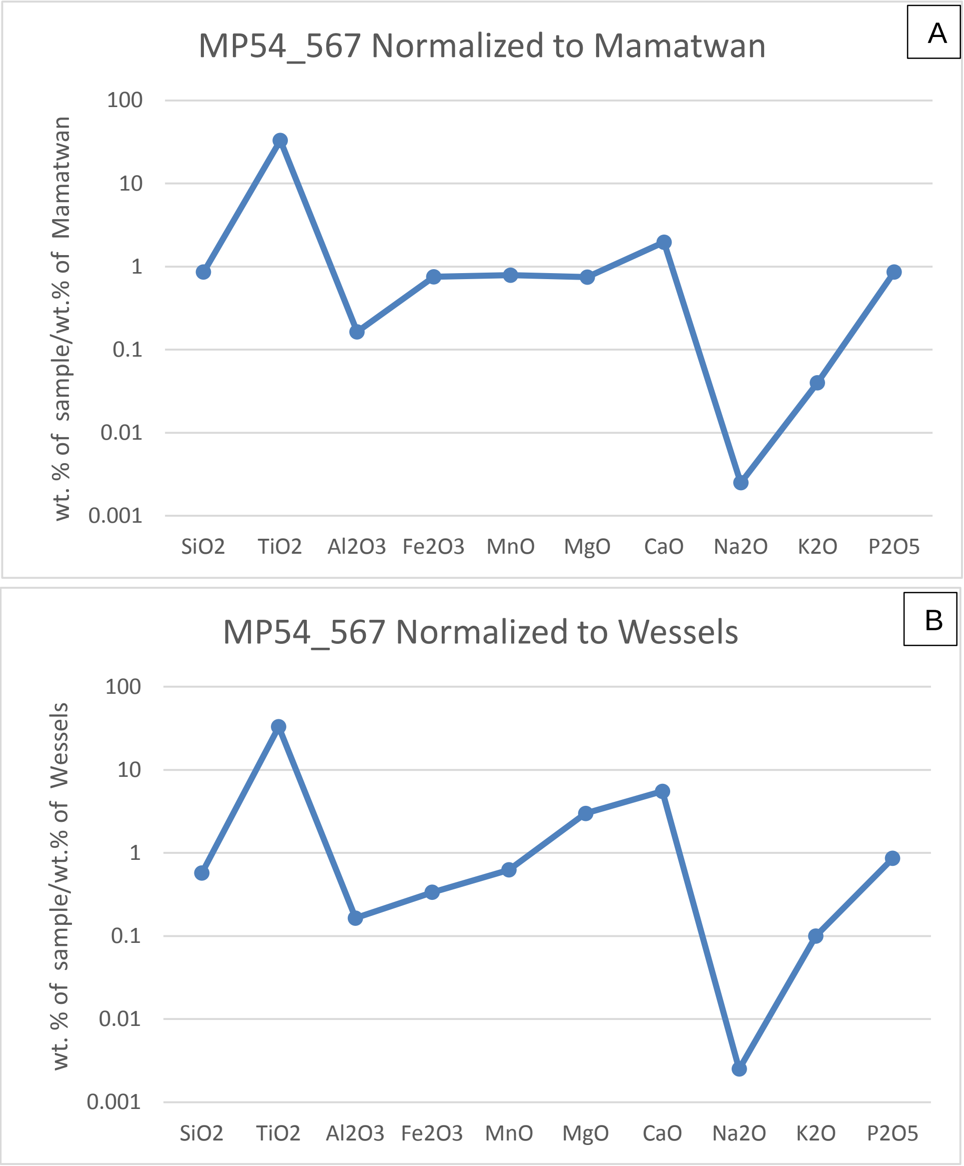

Figure 6-7 Spider diagrams of Middelplaats low-grade ore MP54_567 normalized to average - A) Mamatwan-type and -B) Wessels-type ores. Diagrams show enrichment or depletion relative to the average ore compositions

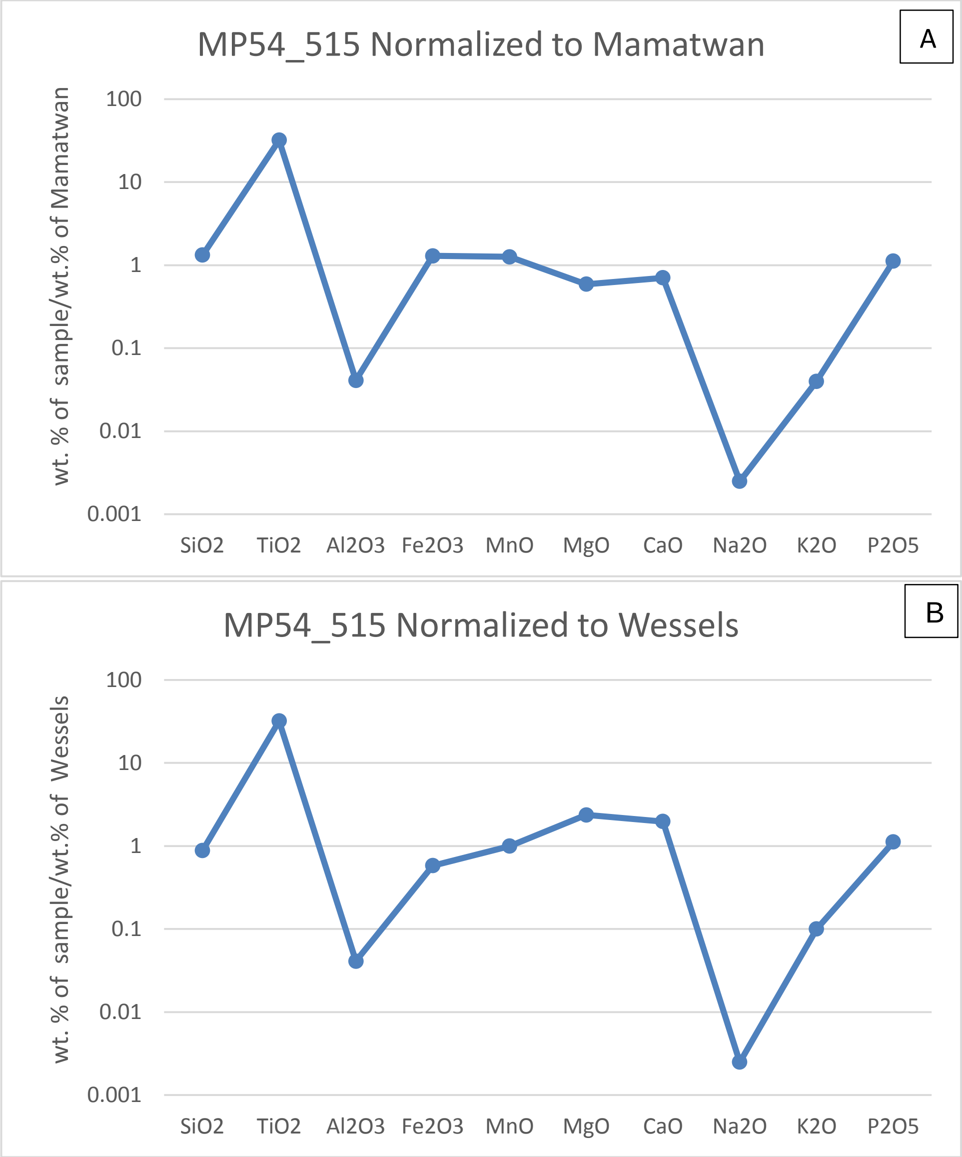

Figure 6-8 Spider diagrams of Middelplaats high-grade ore MP54_515 normalized to average - A) Mamatwan-type and -B) Wessels-type ores. Diagrams show enrichment or depletion relative to the average ore compositions.

Comparison of the Middelplaats low-grade ore (MP54_567) with Mamatwan-type ores (Figure 6-7A), shows the Middelplaats ore is depleted in TiO_2, P_2O_5, SiO_2, Na_2O, Fe_2O_3, Al_2O_3, MgO and MnO and has a pronounced enrichment in CaO. The comparison to Wessels-type ore (Figure 6-7B) is poor. Depletions are shown in P_2O_5, SiO_2, Na_2O, Fe_2O_3, Al_2O_3, and MnO. Elements MgO, CaO and TiO_2 displayed as enriched.

Figure 6-8A shows the Middelplaats high-grade ore (MP54_515) is slightly enriched in SiO_2, TiO_2, Fe_2O_3, and P_2O_5, whilst depleted in CaO and MgO compared to Mamatwan-type ore. The comparison to Wessesl-type ore (Figure 6-8B) shows the Middelplaats high-grade ore is enriched in TiO_2, MgO and CaO and depleted in Al_2O_3 and Fe_2O_3.

However, the apparent compositional similarities shown in the spider diagrams, particularly the Mamatwan-type ore comparisons might be somewhat misleading. The spidergrams represent bulk rock composition and not mineralogical composition. The mineralogical composition of the Middelplaats ore samples varies significantly from the published composition of the Wessels and Mamatwan-type ores. Mamatwan-type ore is typically described as containing braunite, hematite, kutnohorite and manganocalcite and the high-grade Wessels-type ore as being composed of braunite, bixbyite and hausmannite (Gutzmer & Beukes, 1996; Gutzmer & Beukes, 1997; Astrup & Tsikos, 1998), whereas both Middelplaats ore samples are composed of only hausmannite, andradite and calcite with minor amounts of braunite (see Chapter 4 petrography).

6.2.2 Middelplaats manganese ore mineral composition

Although the Middelplaats manganese ore samples appear quite different in thin section, hand sample and microscopically (Figure 4-5 to 4-10), the mineralogical composition of the two ore samples is similar. Figure 6-9 is a composite of XRD powder diffraction patterns of common manganese ore and gangue minerals along with the diffraction patterns of the two manganese ore samples. The XRD spectral analysis shows the two ore samples to be composed of almost identical mineral phases. The primary difference in mineralogy, being the low-grade sample MP54_567 contains small amounts of braunite and the appearance of ferroan-hausmannite in MP54_515.

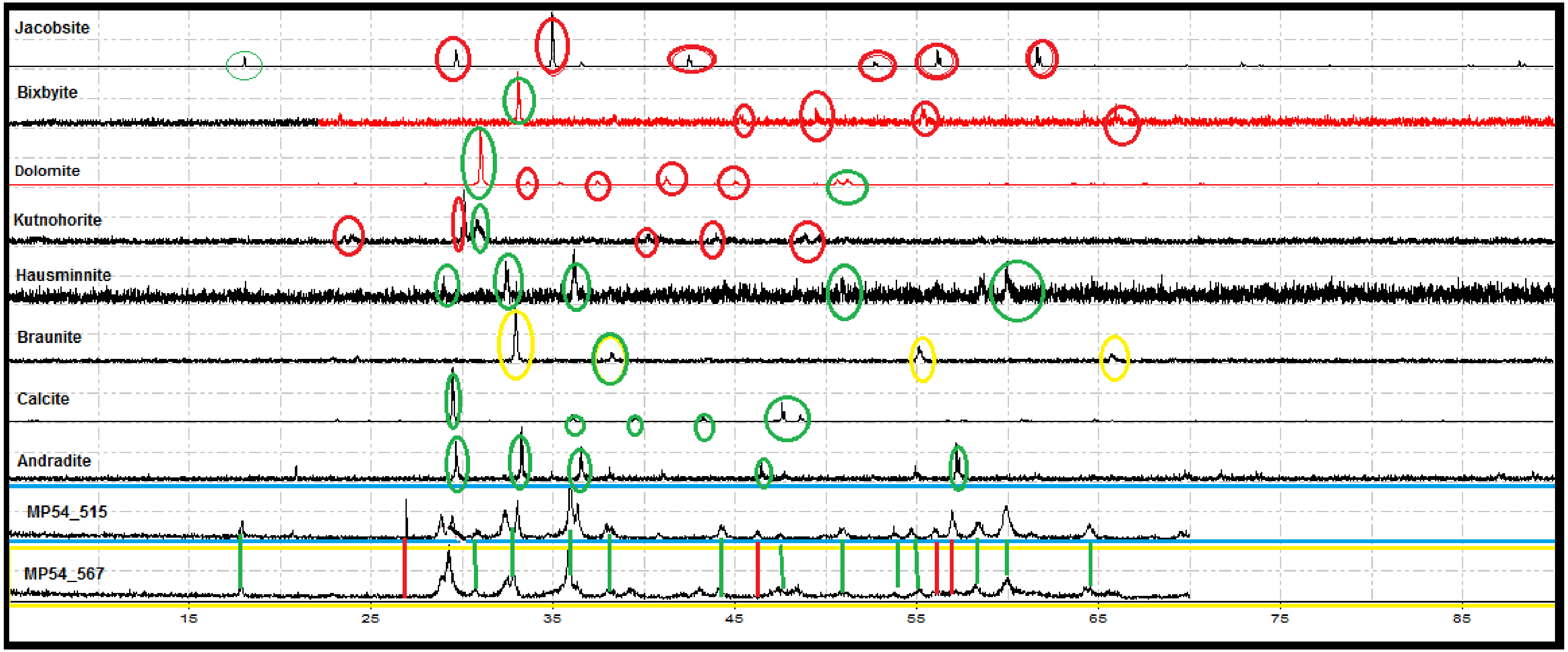

Figure 6-9 Combined XRF mineral phase graph of manganese ores. Red circles indicate no peak match, green circles match both samples and yellow match only MP54_567. Red and green lines show similarity between the 2 manganese ores. Please note the almost identical patterns between the 2 samples (MP54_515 and MP54_567).

6.2.3 Middelplaats manganese ore alteration processes

In the high-grade Middelplaats ore, SiO_2, Fe_2O_3 and MnO appear to be increasing proportionally to a decrease in CaO (Table 6-1). Based on mineral compositions of both the high-grade and low-grade ores, the reaction would appear to be one in which the CaO (from the calcites) and silica (from the braunite) in the low-grade ores (MP54_567) are being re-mobilized into andradite whilst the excess CaO and CO_2 are being driven off. This leaves a residual ore highly concentrated with Mn, Fe_2O_3 and SiO_2, and almost no calcite. Compositionally this ore is almost pure hausmannite and andradite. Gutzmer and Beukes (1997) proposed similar metasomatic process for fault controlled hydrothermal upgrading of ore in the northwestern part of the Kalahari manganese field.

Bulk chemical composition of both Middelplaats high-grade and low-grade ore samples appears to represent a differing stage of alteration. This is supported by the fractionated patterns seen in the normalized spider diagrams. Therefore, without a protolith ore to use as base, calculations of actual mass loss/gain between these two samples yields a somewhat skewed result. However, in an effort to establish the basic alteration process involved in the mass loss/gain between the Middelplaats low-grade (MP54_567) and high-grade (MP54_515) ores, calculations of mass loss and mass gain have been calculated based on common LOI and CaO (data is taken from Table 6-4). This simplified view of elemental mass loss/gain between the high-grade and low-grade Middelplaats ore samples may elucidate the general processes occurring during the metasomatic upgrading of these ores.

In order to quantify this, Table 6-4 replaces the values of LOI, CaO and H_2O within the Middelplaats low-grade ore (MP54_567), with the values from the Middelplaats high-grade ore (this led to a substantial decrease in the total mineral assemblage percentage). The composition of the Middelplaats low-grade ore was then normalized back to 100% in order to examine if the loss of CO_2, H_2O and CaO would produce the high-grade MP54_515 ore.

As one can see from the mass loss/gain section of Table 6-4 it would appear that the predominant process is indeed one of devolatilization with the loss of CO_2 as well as a loss of and/or re-mobilization or CaO, which changes with distance from the contact.

The main immobile element Mn, increases proportionally to the loss of volatiles as does silica and phosphorus. However, without the proper protoliths the reaction with regard to all other minerals fails to balance showing notable increases of ~ 148 weight % in several mineral phases. This, combined with mineral compositions analysed within the contact zone in samples MP54_CS3 and MP53_BIF, are indicative of a more complex process in which one event is overprinting another. However, for illustrative purposes, this same calculation has been used to show if this process would work if the protolith were the Mamatwan or Wessels-type ores.

Table 6-4 Mass loss/gain calculation: bulk rock compositions of the 2 Middelplaats ores (Left) and the low grade MP54_567 with LOI and CaO set to values of High-grade MP54_515 then normalized back to 100%. Table calculates the mass loss/gain if the reaction involves only the loss of LOI, CaO and H_2O

Sample name	**MP54_567**	**MP54_515**	MP54_567 Set to equivalent LOI and CaO of MP54_515	MP54_567 Normalized to 100%	Relative Mass loss/gain between devolatilized MP54_567 and 515. This shows % change in elemental composition for this reaction.
SiO_2	4.295	6.620	4.295	6.275	94.80%
TiO_2	0.033	0.032	0.033	0.048	150.68%
Al_2O_3	0.164	0.041	0.164	0.240	584.44%
Fe_2O_3	5.377	9.267	5.377	7.856	84.78%
MnO	42.523	67.800	42.523	62.131	91.64%
MgO	2.984	2.364	2.984	4.360	184.43%
CaO	27.537	9.863	9.86	14.407	146.07%
K_2O	0.002	0.002	0.002	0.003	146.11%
P_2O_5	0.043	0.056	0.043	0.063	112.19%
LOI	16.770	2.920	2.92	4.266	146.11%
H_2O	0.530	0.240	0.24	0.351	146.11%
Total	100.257	99.204	68.441	100.000	100.80%

Table 6-5 Mass loss/gain calculation: The Mamatwan-type ore has been set to the LOI and CaO values of high-grade MP54_515 then normalized back to 100%. Table calculates the mass loss/gain if the reaction involves only the loss of CaO, CO_2.

Sample name	**Average Mamatwan**	**MP54_515**		Mamatwan-typeset to equivalent LOI and CaO of MP54_515	Mamatwan-typeNormalized to 100%	Relative Mass loss/gain between devolatilized Mamatwan-type ore and MP54_515. This shows % change in elemental composition for this reaction.
SiO_2	4	6.62		4	4.66	70.53%
TiO_2	0	0.032		0	0	0.00%
Al_2O_3	1	0.041		1	1.16	2847.00%
Fe_2O_3	8.6	9.267		8.6	10.03	108.33%
MnO	54.6	67.8		54.6	63.73	94.00%
MgO	4	2.364		4	4.66	197.51%
CaO	14	9.863		9.86	11.50	116.69%
K_2O	0.05	0.002		0.4	0.46	23345.40%
P_2O_5	0.05	0.056		0.05	0.05	104.22%
LOI	8.8	2.92		2.92	3.40	116.73%
H_2O	3.5	0.24		0.24	0.28	116.73%
Total	99	99.204		85.67	100	100.80%

Table 6-6 Mass loss/gain calculation: The Wessels-type ore has been set to the LOI and CaO values of high-grade MP54_515 then normalized back to 100%. Table calculates the mass loss/gain if the reaction involves only the loss of CaO, CO2.

Sample name	**Average Wessels**	**MP54_515**		Wessels set to equivalent LOI and CaO of MP54_515	Wessels Normalized to 100%	Relative Mass loss/gain between volatilized Wessels-type ore and MP54_515. This shows % change in elemental composition for this reaction.
SiO_2	6	6.62		6	5.75	86.93%
TiO_2	0	0.032		0	0	0.00%
Al_2O_3	1	0.041		1	0.95	2339.37%
Fe_2O_3	15.7	9.267		15.7	15.05	162.50%
MnO	67.5	67.8		67.5	64.74	95.49%
MgO	1	2.364		1	0.95	40.57%
CaO	5	9.863		9.86	9.45	95.88%
K_2O	0.02	0.002		0.02	0.019	959.14%
P_2O_5	0.05	0.056		0.02	0.019	34.26%
LOI	1.02	2.92		2.92	2.80	95.91%
H_2O	2.3	0.24		0.24	0.23	95.91%
Total	99.99	99.204		104.26	100	100.80%

Table 6-5 and Table 6-6 both produce interesting and potentially useful results. The reaction using Mamatwan-type ore fails to produce enough Mn, which is the principal immobile element. However, the other elements seem to have slightly better results.* The reaction using the Wessels-type ore produces the best overall results with manganese, LOI, CaO and H_2O all around 95.5%. Both of these reactions also produce excess Fe_2O_3 (which is consistent with the composition of the Middelplaats high-grade ore, MP54_515) and excess potassium. The Wessels-type ore reaction produced 960% K and the Mamatwan-type reaction 23,345%. These reactions would seem to indicate that the actual protolith was a higher-grade ore than either the Mamatwan-type or the Middelplaats low-grade ore.

* The original data for the Wessels and Mamatwan-type ore reported by Miyano and Beukes, (1987) is after SAMANCOR, (1969). This is a brochure produced for investors and the general public in 1969. The chemical data reported therein for the Al would seem to be spurious. All elements are rounded to 2 digits after 0. It seems unlikely that in both ores the actual values were between 1.04 and 0.95. Therefore it is the authors belief these Al results should be disregarded.

Chapter 7 Conclusions, Future Work and Exploration

7.1 *Conclusions*

7.1.1 Combined igneous and manganese alteration

The reaction zone between the manganese ore and the igneous rocks (sample MP54_CS3) appears to be the result of contact metamorphism. This is based on the stratigraphic field relationships, petrographic and geochemical results in this report. From the data produced with regards to the devolatilization reaction, (Tables 6-3 to 6-5) and the apparent potassic alteration of the igneous rocks, (Figure 5-6). It is clear there are 2 to 3 metasomatic alteration events occurring which are also likely overprinting one another (devolatilization in the manganese ore, wide spread K-alteration in the dolerites and localized K alteration near the contact zone or Fe alteration around the interaction area with the underlying BIF). As an example, if one considers the Middelplaats dolerites had to pass stratigraphically through the underlying BIF (as demonstrated by the incorporation of a BIF xenolith in sample MP54_CS3); there should be excess iron available for re-distribution. This could account for the replacement of grossular with andradite without any interaction with the manganese ore. The reaction is:

$3SiO_2 + 3CaCO_3 + \frac{1}{4} Fe_2O_3 + 1/8\ O_2 = Ca_3Fe_2Si_3O_{12} + 3CO_2$ (andradite)

In addition, one cannot discount that all the reactions modelled for the devolatilization of the manganese ores produced excess potassium. The maximum thickness of the lower manganese bed in the Hotazel Formation is reported to be 45m in the Mamatwan mine area (Gutzmer & Beukes, 1995a). This volume of manganese ore would likely be insufficient to produce the required potassium to account for the bulk rock composition of the Middelplaats dolerites (with the caveat the thickness of the Middelplaats dolerites is unknown as the drilling stopped upon encountering the igneous rock). Therefore, it is likely there was an additional potassic fluid sometime after emplacement that resulted in the widespread alteration within the dolerites.

7.1.2 The relationship of the Middelplaats dolerites to the Ongeluk Formation

Geochemically these two sample sets are quite similar. Both data sets plot in the same areas on the various classification charts, which is a good indication of similar bulk rock composition. The trace element spider diagrams (Figure 6-2) of the two sample sets are substantially identical with the Middelplaats samples showing a variation that is well constrained by the variation within the Ongeluk Formation sample data. The bulk rock and trace element composition of the two sample sets also show low standard deviations between the reported elements. Although standard deviation in a combined sample set is not direct evidence of relationship between two data sets, it does highlight that there is little difference between the two sets of data.

Examination of the bivariate diagrams displays reasonable trends that are suggestive of a relationship. These diagrams also show some very slight indication for three separate but congruent trends (Ongeluk massive lava, Ongeluk regional and composite and Middelplaats) which may be indicative of progressive fractionation within a source region.

The ratio/ratio quad-variate diagrams show very reasonable overlap of data for both the Middelplaats samples internally and correlation between the Middelplaats samples and the Ongeluk Formation data. This must however be considered within the constraints of the established correlative range set by the relationship of sample MP53_S1 and S2. Therefore, within this data set, there is reasonable evidence to propose a geochemically similar source region for the Middelplaats dolerites and the larger Ongeluk Formation. Also, based on the stratigraphic and crosscutting relationships to the manganese ore and field relationships reported by Jennings, (1986), the timing of emplacement of the MP53 and MP54 dolerites can be constrained to post-Transvaal but pre-Karoo. This would indicate some sort of re-activation of the Ongeluk Formations source region.

This is also not without precedent. Schutte, (1992) in his discussion of the Ongeluk with relation to the Hotazel formation “The Kalahari Ongeluk lava or Ongeluk sensu lato” section 2.4.4. The author describes dolerite dykes and sills with a NNE trend (the same as the Middelplaats intrusion) saying “Dolerite dykes and sills occur throughout the area; they represent several episodes of intrusion from Ongeluk to Karoo times”.

He goes on to say, “These dykes might be feeder dykes of the Ongeluk lava. Coarse-grained dolerite is seen to intrude rocks of the Ongeluk Lava on Bovenongeluk 29 and in several boreholes (Wessels Mine, Black Rock). The dyke contacts are sharp and sometimes exhibit a narrow, fine grained chilled margin”. Schutte further describes a rock composition of “essentially plagioclase and augite”. This author’s description is consistent with the observed dolerite petrography and the contact with the manganese ore in the Middelplaats mine area.

Finally, it must be mentioned that although the data presented herein demonstrates a relationship between the Middelplaats dolerites and the Ongeluk Formation. The sample set is far too small to suggest this relationship would hold true under more rigorous testing with a larger data set. Although the statistical method used herein to establish a correlative range for the data is scientifically valid, the size of the sample set inherently introduces a large error range. The fact that there is a discernable difference between two genetically related samples taken just a few meters apart would indicate the need to use a much larger dataset to overcome this inherent deviation.

7.2 *Future work*

Much work still needs to be done to understand the nature of the contact between the manganese ore and the underlying Middelplaats dolerites. Substantial knowledge could be learned by dating the time of intrusion. The exact mechanism of the metasomatic upgrading of the manganese ore also needs work. This could be accomplished by more detailed sampling of the existing core whilst investigations into the dolerites may require at least one or two new holes that penetrate the entire thickness of the intrusion. Detailed isotopic studies would also help give a better understanding the relationship between the Middelplaats dolerites and the Ongeluk Formation. The nature of the potassic alteration within the contact zone should also be explored, as there is no readily apparent source for the fluids.

7.3 *Exploration*

The most significant exploration potential in this area deals with the nature of the ore along the contact. For a distance of over 5 meters, the ore grades vary between 25 and 40% manganese. Economically the composition of the ore is important. Compositionally the manganese ore is almost 100% hausmannite, which is the purest form of manganese oxide and has a simple beneficiation method. This could make this somewhat low-grade ore economically viable. In addition, assuming the dolerites were emplaced as a sill like body one would expect to find a continuation of the Hotazel Formation manganese below the sill, which may also be economically viable.

References

Altermann, W. & Nelson, D. R., 1998. Sedimentation rates, basin analysis and regional correlations of three Neoarchaean and Paleoproterozoic sub-basins of the Kaapvaal craton as inferred from percise U-Pb zircon ages from volcaniclastic sediments. *Sidementary Geology,* Volume 120, pp. 225-256.

Armstrong, R. A. et al., 1991. Zircon ion microprobe studies bearing on the age and evolution of the Witwatersrand triad. *Precambrian Research,* Volume 53, p. 243–266.

Ashworth, J. R., 1986. Myrmekite replacing albite in prograde metamorphism. *American Mineralogist,* Volume 71, pp. 895-899.

Astrup, J. & Tsikos, H., 1998. In: M. Wilson & C. R. Anhaeusser, eds. *The Mineral Resources of South AfricaManganese.* 6TH ed. Silverton: Council for Geoscience, pp. 450-460.

Bachelor, R. A. & Bowden, P., 1985. Petrologic interpretation of granitoid rocks using multicationic parameters. *Chemical Geology,* Volume 48, pp. 43-55.

Barley, M. E., Bekker, A. & Krapez, B., 2005. Late Archean to Early Paleoproterozoic global tectonics, environmental change and the rise of atmospheric oxygen. *Earth and Planetary Science Letters,* Volume 238, pp. 156-171.

Bau, M., Romer, R. L., Luders, V. & Beukes, N. J., 1999. Pb, O, and C isotopes in silicified Moodraai dolomite (Transvaal Supergroup, South Africa): implications for the composition of Paleoproterozoic seawater and "dating" the increase of oxigen in the Precambrian atmosphere. *Earth and Planetary Science Letters,* Volume 174, pp. 43-57.

Berner, R. A., 1991. A model for atmospheric CO2 over Phanerozoic time. *American Journal of Science,* Volume 291, pp. 339-376.

Best, M. G., 2003. *Igneous and Metamorphic Petrology.* 2nd ed. Malden: Blackwell Science Ltd.

Buhn, B. & Stanistreet, I. G., 1997. Insight into the enigma of Neoproterozoic manganese and iron formations form the prespecective of supercontinental break-up and glaciation. In: K. Nicholas, J. R. Hein, B. Buhn & S. Dasgupta, eds. *Manganese Mineralization: Geochemistry and Minerology of Terrestrial and Marine Deposits, Geological Society Special Publication No. 119.* London: Geological Society, pp. 81-90.

Bullen, D. S., Hall, R. P. & Hanson, R. E., 2012. Geochemistry and petrogenesis of mafic sills in the 1.1 Ga Umkondo large igneous province, southern Africa. *Lithos,* Volume 142-143, pp. 116-129.

Calvert, S. E. & Pedersen, T. F., 1996. Sedimentary geochemistry of manganese; implications for the environment of formation of manganiferous black shales. *Economic Geology,* Volume 91, pp. 36-47.

Clarke, B., Uken, R. & Reinhardt, J., 2009. Structural and compositional constraints on the emplacement of the Bushveld Complex, South Africa. *Lithos,* Volume 111, p. 21–36.

Cornell, D. H., Schutte, S. S. & Eglington, B. L., 1996. The Ongeluk basaltic andesite formation in Griqualand West, South Africa: submarine alteration in a 2222 Ma Proterozoic sea. *Precambrian Research,* Volume 79, pp. 101-123.

Deer, W. A., Howie, R. A. & Zussman, J., 1972. *Rock Forming Minerals, Vol. l, Ortho- and Ring Silicates.* London: Longmans Group Ltd..

Deer, W. A., Howie, R. A. & Zussman, J., 1992. *An Introduction to the Rock-Forming Minerals.* 2nd ed. Essex: Pearson Education LTD.

Des Marais, D. J., 1994. The Archean atmosphere: its composition and fate. In: K. C. Condie, ed. *Archean Crustal Evolution. Developments in Precambrian Geology.* Amsterdam: Elsevier, pp. 505-522.

DeYoung, J. H., Sutphin, D. M. & Cannon, W. F., 1984. International strategic minerals inventory summary report - Manganese. *USGS circular 930-A,* p. 22.

Downs, T. R., 2006. *The RRUFF Project: an integrated study of the chemistry, crystallography, Raman and infrared spectroscopy of minerals Program and Abstracts of the 19th General Meeting of the International Mineralogical Association.* Kobe, International Mineralogical Association.

Duncan, A. R., Erlank, A. J. & Marsh, J. S., 1984. Regional Geochemistry of the Karoo Igneous Provence. *Special Pulication of the Geological Society of Aouth Africa,* Volume 13, pp. 355-388.

Eriksson, P. G. & Altermann, W., 1998. An overview of the geology of the Transvaal Supergroup dolomites (South Africa).. *Environmental Geology,* Volume 36, pp. 179-188.

Eriksson, P G; Lenhardt, N; Wright, D T; Mazumder, R; Bumby, A J., 2001. Major influences on the evoultion of the 2.67-2.1 Ga Transvaal basin, Kaapvaal craton. *Sedimentary Geology,* Volume 141-142, pp. 205-231.

Eriksson, P. G. & Clendenin, C. W., 1990. A review of the Transvaal Sequence, South Africa. *Journal of African Earth Science,* 10(1/2), pp. 101-116.

Eriksson, P G; Lenhardt, N; Wright, D T; Mazumder, R; Bumby, A J., 2011. Late Neoarchaean-Paleoproterozoic supercrustal basin-fills of the Kaapvaal craton: Relevance of the supercontinent cycle, the "great Oxidation Event" and "Snowball Earth". *Marine and Petroleum Geology,* Volume 28, pp. 1385-1401.

Eriksson, P G; Schweitzer, J K; Bosch, P J; Schereiber, U M; Van Deventer, J L; Hatton, C., 1993. The Transvaal Sequence:an overview. *Journal of African Earth Science,* Volume 16, pp. 25-51.

Evans, A. M., 1993. *Ore Geology and Industrial Minerals.* 3Rd ed. Malden: Blackwell Publishing.

Fitton, J G; Saunders, A D; Norry, M J; Hardarson, B S; Taylor, R N., 1997. Thermal and chemical structure of the Iceland plume. *Earth and Planetary Science Letters,* Volume 153, pp. 197-208.

Frauenstein, Frank; Viezer, Jan; Beukes, N; Van Niekerk, H S; Coetzee, L., 2009. Transvaal Supergroup carbonates: Implications for Paleoproterozoic δ18O and δ13C records. *Precambrian Research,* Volume 175, pp. 149-160.

Glasby, G., 1988. Manganese Deposition Trough Geological Time: Dominance of the Post-Eocene Deep-Sea Environment. *Ore Geology Reviews,* Volume 4, pp. 135-144.

Griffin, W. L., Graham, S., O'Reilly, S. Y. & Pearson, N. J., 2004. Lithosphere evolution beneath the Kaapvaal Craton: Re–Os systematics of sulfides in mantle-derived peridotites. *Chemical Geology,* Volume 208, pp. 89-118.

Gurnis, M., 1988. Large-scale mantle convection and aggreation and dispersal of supercontinents. *Nature,* Volume 332, pp. 695-699.

Gutzmer, J. & Beukes, N. J., 1995a. Fault-Controlled Metasomatic Alteration of Early Proterozoic Sedimentary anganese Ores in the Kalahari Manganese Field, South Africa. *Economic Geology,* Volume 90, pp. 823-844.

Gutzmer, J. & Beukes, N. J., 1995b. Magentic hausmannite from hydrothermally altered manganese ore in the Paleoproterozoic Kalahari manganese deposit, Transvaal Supergroup, South Africa. *Mineralogical Magazine,* Volume 59, pp. 703-716.

Gutzmer, J. & Beukes, N. J., 1996. Mineral paragenesis of the Kalahari manganese field, South Africa. *Ore Geology Reviews,* Volume 11, pp. 405-428.

Gutzmer, J. & Beukes, N. J., 1997. Effects of mass transfer, compaction and secondary porosity on hydrothermal upgrading of Paleoproterozoic sedimentary manganese ore in the Kalahari manganese field, South Africa. *Mineralium Deposita,* Volume 32, pp. 250-256.

Gutzmer, J. & Beukes, N. J., 1998. Earliest laterites andd possible evidence for terrestrial vegetation of the Early Proterozoic. *Geology,* Volume 26, pp. 263-266.

Hannah, J. L., Bekker, A., Stein, H. J. & Holland, H. D., 2004. Primitive Os 2316 Ma age for marine shale: Implications for Paleoproterozoic glacial events and the rise of atmospheric oxigen. *Earth and Planetary Science Letters,* Volume 225, pp. 43-52.

Hawthorne, F. C., 1981. Amphibole spectroscopy. In: D. R. Veblen & P. H. Ribbe, eds. *Reviews in Mineralogy 9A.* Baltimore: Mineralogical Society of America, p. 103–139.

Hughes, C. J., 1973. Spilites, keratophyres and the igneous spectrum. *Geological magazine,* Volume 109, pp. 513-527.

Huntner, D. R. & Halls, C. H., 1992. A geochemical study of a Precambrian mafic dyke swarm, Eastern Transvaal, South Africa. *Journal of African Earth Sciences,* Volume 2, pp. 153-168.

International Manganese Institute, 2013. *International Manganese Institutite-Reserves.* [Online] Available at: http://www.manganese.org/about_mn/reserves [Accessed 21 October 2013].

James, D. E., Nui, F. & Rokosky, J., 2003. Crustal structure of the Kaapvaal craton and its significance for early crustal evolution. *Lithos,* Volume 71, pp. 413-429.

James, H. L. & Trendall, A. F., 1982. Banded iron formations: Distribution in time and paleoenvironmental significance. In: H. D. Holland, ed. *Mineral Deposits and Evolution of the Bio Sphere.* Dahlem Konferenzen: Springer, pp. 199-218.

Jennings, M., 1986. The Middleplaats Manganese Ore Deposit, Griqualand West. In: C. R. Anhaeusser & S. Maske, eds. *Mineral Deposits of South Africa Vol. 1.* Johannesberg: Geological Society of South Africa, pp. 979-983.

Kasting, J. F., 2013. What caused the rise of atmospheric O2?. *Chemical Geology,* Volume 362, pp. 13-25.

Kerr, R. A., 2005. The story of O2. *Science,* Volume 308, pp. 1730-1732.

Kirschvink, J L; Gaidos, E J; Bertani, L E; Beukes, N J; Gutzmer, J; Maepa, L N; Steinberger, R E., 2000. Paleoproterozoic Snowball Earth:Extream Climate and Geochemical Global Change and Its Biological Consequences. *Proceedings of the National Academy of Science of the United States of America,* Volume 97, pp. 1400-1405.

Klausen, M B; Soderlund, U; Olsson, J R; Ernst, R E; Armoogam, M; Petzer, G; Mkhinze, S W., 2010. Petrological discrimination among Precambrian dyke swarms: Easrtern Kaapvaal Craton (South Africa). *Precambrian Research,* Volume 183, pp. 501-522.

Kleyenstuber, A., 1984. A regional mineralogical study of the manganese bearing Voelwater Subgroup in the Northern Cape Provence. In: *PhD Thesis Unpublished.* Johansburg: RAU, p. 328.

Laetsch, T. & Downs, R. T., 2006. *Crystalslueth: Software For Identification and Refinement of Cell Parameters From Powder Diffraction Data of Minerals Using the RRUFF Project and American Mineralogist Crystal Structure Databases,* Kobe: International Mineralogical Association.

Maitre, R W; Streckeisen, A; Zanettin, B; Le Bas, M J; Bonin, B; Bateman, P; Bellieni, G; Dudek, A; Efremova, S; Keller, J; Lameyre, J; Sabine, P A; Schmid, R; Sorensen, H; Woolley, A R., 2002. *Igneous Rocks A Classification and Glossary of Terms.* 2nd ed. Cambridge: Cambridge University Press.

Ludeers, V., Gutzmer, J. & Beukes, N., 1999. Fluid inclusion studies in cogenetic hematite, hausmannite and gangue minerals from rich high-grade manganese ores in the Kalahari Manganese Field, South Africa. *Economic Geology,* Volume 94, pp. 589-596.

McDonough, W. F. & Sun, S., 1995. The composition of the Earth. *Chemical Geology,* Volume 120, pp. 233-253.

Meschede, M., 1986. A method of discriminating between different types of mid-ocean ridge basalts and continental tholeiites with Nb-Zr-Y diagram. *Chemical Geology,* Volume 56, pp. 207-218.

Middlemost, E. A. K., 1994. Naming materials in the magma/igneous system. *Earth-Science Reviews,* Volume 37, pp. 215-224.

Miyano, T. & Beukes, N., 1987. Physicochemical Environments for the Formation od Quartz-Free Manganese Oxide Ores from the Early Proterozoic Hotazel Formation, Kalahari Manganese Field, South Africa. *Economic Geology,* Volume 82, pp. 706-718.

Moon, C. J., Whateley, M. K. & Evans, A. M. eds., 2006. *Introduction to Mineral Exploration.* Malden: Blackwell Publishing.

Moore, J. M., Tsikos, H. & Polteau, S., 2001. Deconstructing the Transvaal Supergroup, South Africa: implications for Paleoproterozoic paleoclimate models. *African Earth Science,* Volume 33, pp. 437-444.

Morimoto, M., 1988. Nomenclature of Pyroxenes. *American Mineralogist,* Volume 73, pp. 1123-1133.

Neil, C. J., Beukes, N. J. & De Villiers, R., 1986. The manatwan mine of the Kalahari manganese field. In: C. R. Anhaeusser & S. Maske, eds. *Mineral Deposits of Southern Africa.* Johansburg: s.n., pp. 963-978.

Norrish, K. & Chappell, B. W., 1967. X-ray fluorescence spectrography. In: J. Zussman, ed. *Physical Methods in Dwterminative Minerology.* London: Academic Press, p. 514.

Norrish, K. & Hutton, J. T., 1969. An accurate X-ray spectrographic method for the analysis of a wide range of geological samples. *Geochimica et Cosmochimica Acta,* 33(4), pp. 431-453.

Pearce, T. H., 1968. A contribution to the theory of variation diagrams. *Contributions to Mineralogy and Petrology,* Volume 19, pp. 142-157.

Pearce, T. H., 1987. The identification and assessment of spurious trends in pearce-type ratio variation diagrams: a discussion of some statistical arguments. *Contributions to Mineralogy and Petrology,* Volume 97, p. 529–534.

Robb, L., 2005. *Introduction to Ore-Forming Processes.* Madin: Blackwell Science Ltd.

Rollinson, H., 1993. *Using Chemical Data: Evaluation, Presentation, Interpretation.* Essex: Pearson Education Limited.

Roy, S., 1988. Manganese Metallogenesis : A Rivew. *Ore Geology Reviews,* Volume 4, pp. 155-170.

Roy, S., 1997. Genetic diversity of manganese deposition in the terresterial geological record. In: K. Nicholson, J. R. Hein, B. Buhn & S. Dasgupta, eds. *Manganese Mineralization: Geochemistry and Mineralology of Terrestrial and Marine Deposits.* London: Geological Society, pp. 5-27.

Roy, S., 2006. Sedimentary manganese metallogenesis. *Earth Science Reviews,* Volume 77, pp. 273-305.

Russell, J. K. & Nicholls, J., 1988. Analysis of petrologic hypotheses with Pearce element ratios. *Contributions to Mineralogy and Petrology,* 99(1), pp. 25-35.

Sakar, S. N., 1980. Precambrian stratigraphy and geocronology of Peninsular India-a review. *Indian Journal of Earth Science,* Volume 7, pp. 12-26.

SAMANCOR, 1969. *Brochure describing the manganese and iron interests of the Samancor Group of Companies; pg 20.* Johannesburg: Amcor House.

Schissel, D. & Aro, P., 1992. The major Early Proterozoic sedimentary iron and manganese deposits and theit tectonic setting. *Ecnomic Geology,* Volume 87, pp. 1367-1374.

Schlüter, T., 2006. *Geological Atlas of Africa.* Verlag: Springer.

Sleep, N. H., 2003. Simple features of mantle-wide convection and the interpretation of lower-mantle tomograms. *Geodynamics,* Volume 335, pp. 9-22.

Smithies, R. H., Champion, D. C. & Cassidy, K. F., 2003. Formation of Earth's early Archaean continental crust. *Precambrian Research,* Volume 127, pp. 89-101.

Smithies, R. H., Champion, D. C. & Van Kranendonk, M. J., 2009. Formation of Paleoarchaen continental crust through infracrustal melting of enriched basalt. *Earth and Planetary Science Letters,* Volume 281, pp. 298-306.

Smithies, R. H., Van Kranendonk, M. J. & Champion, D. C., 2007. The Mesoarchean emergence of modern-style subduction. *Gondwana Research,* Volume 11, pp. 50-68.

South African Heritage Resources Agency, 2013. *Middelplaats 332 EMP 10017.* [Online]
Available at: http://www.sahra.org.za/content/middelplaats-332-emp-10017
[Accessed 25 October 2013].

Tarney, J. & Weaver, B., 1987. Geochemistry and Petrogenesis of Early Proterozoic Dyke Swarms. In: H. C. Halls & W. F. Fahrig, eds. *Mafic Dyke swarms.* Ottawa: Geological association of Canada, pp. 81-94.

Tiskos, H., Matthews, A., Erel, Y. & Moore, J., 2010. Iron isotopes constrain biogeochemical redox cycling of iron and manganese in a Palaeoproterozoic stratified basin. *Earth and Planetary Science Letters,* Volume 298, p. 125–134.

Tsikos, H., 1999. *Petrograhpic and Geochemical Constraints on the Origin and Post-Depositional History of the Hotazel Iron-Manganese Deposits, Kalahaei Manganese Field, South Africa,* Grahamstown: s.n.

Tsikos, H., Beukes, N. J., Moore, J. M. & Harris, C., 2003. Deposition, Diagenesis, and Secondary Enrichment of Metals in the Paleoproterozoic Hotazel Iron Formation, Kalahari Manganese Field, South Africa. *Economic Geology,* Volume 98, pp. 1449-1462.

Tsikos, H. & Moore, J. M., 1997. Petrography and Geochemistry of the Paleoproterozoic Hotazel Iron-Formation, Kalahara Manganese Field, South Africa: Implications for Precambrian Manganses Metallogenesis. *Economic Geology,* Volume 92, pp. 87-97.

Tsikos, H. & Moore, J. M., 2005. Sodic metasomatism in the Paleoproterozoic Hotazel iron - formation, Transvaal Supergroup, South Africa: implications for fluid-rock interaction in the Kalahari manganese field. *Geofluids,* Volume 5, pp. 1-8.

Van Hunen, J. & Van Den Berg, A. P., 2008. Plate tectonics on the early Earth: Limitations imposed by strength and buoyancy of subducted lithosphere. *Lithos,* Volume 103, pp. 217-235.

Von Gruenewaldt, G., Sharpe, M. R. & Hatton, C. J., 1985. The Bushveld Complex; introductionand review. *Economic Geology,* Volume 80, pp. 803-812.

Walter, M. J. & Tronnes, R. G., 2004. Early Earth differentiation. *Earth and Planetary Science Letters,* Volume 225, pp. 253-269.

Wedepohl, K. H., 1980. Potential sources for manganese oxideprecipitation in the oceans. In: I. M. Varentsov & G. Grassley, eds. *Geology and Geochemistry of Manganese Vol-1.* Budapest: Hungarian Academy of Science, pp. 13-22.

Wiggering, H. & Beukes, N. J., 1990. Petrography and Geochemistry of a 2000-2200-Ma-old Hematitic Paleo-Alteration Profile on Ongeluk Basalt of the Transvaal Supergroup, Griqualand West, South Africa. *Precambrian Research,* Volume 46, pp. 241-258.

Young, G. M., 1991. The geologic record of glaciation: relevance to the climatic history of earth. *Geoscience Canada,* Volume 18, pp. 100-108.

Appendix A Rock powder weights for loss on ignition calculations

Appendix Table 1 Weights of rock powders for calculation of loss on ignition (LOI)

Sample Name	Crucible weight	Rock Powder weight	Combined Weight Before Drying	Combined Weight After Drying	Weight of Powder after drying	Combined Weight After Ashing	Free Water Loss	Rock Powder Weight After Ashing	Loss On ignition	Duplicate Samples
MP53_S1-1	20.1051	2.1218	22.2269	22.2188	2.1137	22.1850	0.0081	2.0799	0.0338	
MP53_S2-2	20.0930	2.0370	22.1300	22.1214	2.0284	22.0829	0.0086	1.9899	0.0385	
MP54_S1-1	19.7223	2.0621	21.7844	21.7777	2.0554	21.7110	0.0067	1.9887	0.0667	
MP54_S2-5	20.5425	2.0084	22.5509	22.5460	2.0035	22.4960	0.0049	1.9535	0.0500	
MP54_515-1	20.8298	2.0898	22.9196	22.9146	2.0848	22.8536	0.0050	2.0238	0.0610	Y
MP54_515-2	20.8298	2.0898	22.9196	22.9146	2.0848	22.8536	0.0050	2.0238	0.0610	Y
MP54_515-3	20.8298	2.0898	22.9196	22.9146	2.0848	22.8536	0.0050	2.0238	0.0610	Y
MP54_567-1	20.8634	2.0198	22.8832	22.8725	2.0091	22.5338	0.0107	1.6704	0.3387	Y
MP54_567-2	20.8634	2.0198	22.8832	22.8725	2.0091	22.5338	0.0107	1.6704	0.3387	Y
MP54_567-3	20.8634	2.0198	22.8832	22.8725	2.0091	22.5338	0.0107	1.6704	0.3387	Y

Appendix B **Calculation of standards for the XRF**

Appendix Table 2 Calculation of standards for the XRF

Calculation of standards with accuracy																			
	Mo	V	Cr	Mn	Co	Ni	Cu	Zn	Rb	Sr	Y	Zr	Nb	La	Ce	Nd	Pb	Th	U
BCR-1																			
STD	1.6	407	16	1354	37	13	19	130	47.2	333	38	186	14	24.9	53.7	28.8	13.6	6	1.7
Calc	1.2	414.2	10.8	1381.1	35.8	8.4	27.9	129.6	48.7	337.9	37.9	185.7	13.7	21.9	60.9	31.8	14.8	5.5	0.9
Accuracy	75.00%	101.77%	67.50%	102.00%	96.76%	64.62%	146.84%	99.69%	103.18%	101.47%	99.74%	99.84%	97.86%	87.95%	113.41%	110.42%	108.82%	91.67%	52.94%
G-2																			
STD	0	36	8.7	240	4.6	5	11	86	170	478	11	309	13.5	89	160	55	30	24.7	2.1
Calc	-1.3	28.9	6.9	238	6	4.6	14.5	86.7	165.7	472.6	9.3	306.6	12.1	87.9	159.4	54.3	31.2	24.6	1.8
Accuracy	0.00%	124.57%	126.09%	100.84%	76.67%	108.70%	75.86%	99.19%	102.60%	101.14%	118.28%	100.78%	111.57%	101.25%	100.38%	101.29%	96.15%	100.41%	116.67%
AGV-1																			
STD	3	121	10.1	775	15.3	16	60	88	67.3	662	20	227	15	38	67	33	36	6.5	1.9
Calc	1.4	119.6	7.5	769.5	15.7	13.8	56.3	88.7	68.2	662.9	19.9	227.1	14.8	35.1	82.2	35.6	38.6	6.8	0.6
Accuracy	46.67%	98.84%	74.26%	99.29%	102.61%	86.25%	93.83%	100.80%	101.34%	100.14%	99.50%	100.04%	98.67%	92.37%	122.69%	107.88%	107.22%	104.62%	31.58%
BHOV-1																			
STD	1	317	289	1314	1314	121	136	105	11	403	27.6	170	20	15.8	39	25.2	2.6	1.1	0.4
Calc	0.7	320.9	280	1313.8	1313.8	115.1	136.8	106.1	9.7	395.6	27.3	169.7	20.6	12	41.6	24.6	2.5	1.7	0.8
Accuracy	70.00%	101.23%	96.89%	99.98%	99.98%	95.12%	100.59%	101.05%	88.18%	98.16%	98.91%	99.82%	103.00%	75.95%	106.67%	97.62%	96.15%	154.55%	200.00%
RGM-1																			
STD	2.3								149	108	25	228	10				24	15.1	5.2
Calc	1.4								149.5	103.7	25.1	225	9.4				22.6	14.2	4.8
Accuracy	60.87%	NR	NR	NR	NR	NR	NR	NR	100.34%	96.02%	100.40%	98.68%	94.00%	NR	NR	NR	94.17%	94.04%	92.31%

Appendix Table 2 continued

Calculation of standards with accuracy																			
	Mo	V	Cr	Mn	Co	Ni	Cu	Zn	Rb	Sr	Y	Zr	Nb	La	Ce	Nd	Pb	Th	U
GSN-005																			
STD	19.5	12	190	680	680				149	59.8	99	591	41				19	12.8	0
Calc	16.5	13.5	194.8	698.2	698.2				150.4	61.6	100.6	593.2	41.3				20	12.7	1.3
Accuracy	84.62%	112.50%	102.53%	102.68%	102.68%	NR	NR	NR	100.94%	103.01%	101.62%	100.37%	100.73%	NR	NR	NR	105.26%	99.22%	NR
JB-1																			
STD	34.4	212	401	1163	38.7				41.2	450	24	135	0				7.1	9.2	1.7
Calc	36.6	199	410.7	1150	37.9				41.5	455.5	23.7	135.9	40.6				6	7.6	1.6
Accuracy	106.40%	93.87%	102.42%	98.88%	97.93%	NR	NR	NR	100.73%	101.22%	98.75%	100.67%	NR	NR	NR	NR	84.51%	82.61%	94.12%
KRF-13																			
STD	0	254	268	1294	39	51	66	82	10	208	28.5	107	6.5				5.5	4.6	0
Calc	0.7	251	269.3	1270.3	38.3	42.2	71	82.6	10.4	208.6	29	107.8	7.2				6.2	3.5	1.5
Accuracy	NR	98.82%	100.49%	98.17%	98.21%	82.75%	107.58%	100.73%	104.00%	100.29%	101.75%	100.75%	110.77%	NR	NR	NR	112.73%	76.09%	NR
CAR-08																			
STD	0	207	299	1156	37	70	72	84	19	296	25.5	126	18.5	17	40	19	0	2.5	0
Calc	0.9	205.8	290.9	1157.3	38.4	65	70.6	85.8	19.3	299.8	25.9	128.3	18.6	20.1	42.5	18	2	2	1.1
Accuracy	NR	99.42%	97.29%	100.11%	103.78%	92.86%	98.06%	102.14%	101.58%	101.28%	101.57%	101.83%	100.54%	118.24%	106.25%	94.74%	NR	80.00%	NR
NIM-G																			
STD	2.7					120	14	68	320	10	143	273	0.001	109	195	72	40	51	15
Calc	-0.02					106.8	18.3	60.6	321	10.3	142	271.9	60.7	111.7	187.2	70.6	36.9	51.7	15.4
Accuracy	-0.74%	NR	NR	NR	NR	89.00%	130.71%	89.12%	100.31%	103.00%	99.30%	99.60%	NR	102.48%	96.00%	98.06%	92.25%	101.37%	102.67%
INS-79																			
STD	2.7					1335	126	101											
Calc	-0.02					1337.4	123	103.1											
Accuracy	-0.74%	NR	NR	NR	NR	100.18%	97.62%	102.08%	NR	NR	NR	NR	NR	NR	NR	NR	NR	NR	NR

Appendix E (Electronic records)

Appendix E is the attached CD/DVD. This contains excel sheets of all points analysed on the microprobe and additional photo micrographs. Raw data as well as stoichiometrically balanced data for Fe_2O_3 and cations are contained as well as graphic plots of mineral species. If this item is missing or somehow misplaced duplicate copies can be obtained by contacting the author at mterracin@gmail.com